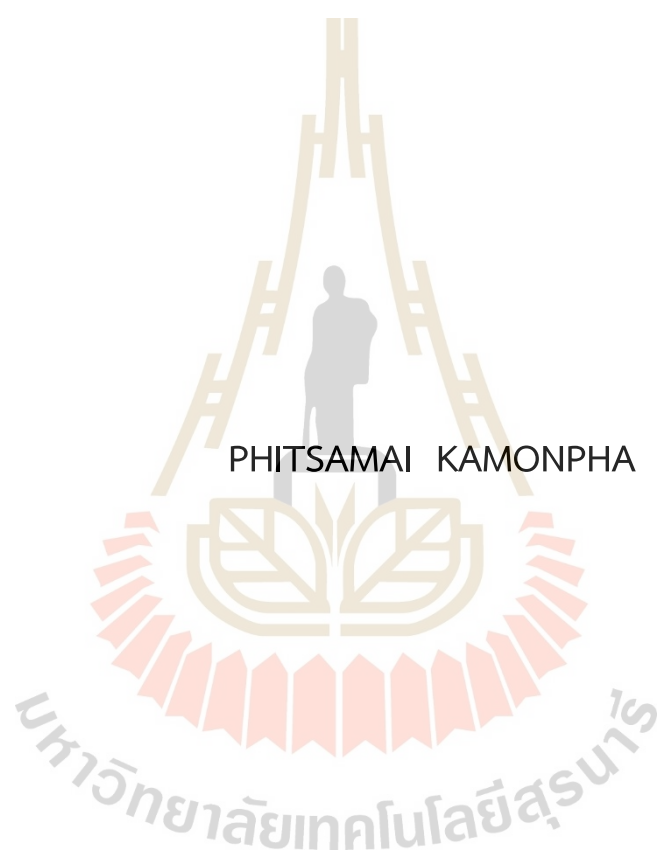


STRUCTURAL AND OPTICAL CHARACTERIZATION OF  
CERIUM DOPED LITHIUM BARIUM GADOLINIUM  
PHOSPHATE GLASS SCINTILLATOR



PHITSAMAI KAMONPHA

A Thesis Submitted in Partial Fulfillment of the Requirements for the

Degree of Doctor of Philosophy in Physics

Suranaree University of Technology

Academic Year 2022

ลักษณะเฉพาะเชิงโครงสร้างและเชิงแสงของแก้วซินทิลเลเตอร์ลิเทียมแบเรียม  
แกโดลิเนียมฟอสเฟตที่เจือด้วยซีเรียม



วิทยานิพนธ์นี้เป็นส่วนหนึ่งของการศึกษาตามหลักสูตรปริญญาวิทยาศาสตรดุษฎีบัณฑิต  
สาขาวิชาฟิสิกส์  
มหาวิทยาลัยเทคโนโลยีสุรนารี  
ปีการศึกษา 2565

STRUCTURAL AND OPTICAL CHARACTERIZATION OF CERIUM DOPED  
LITHIUM BARIUM GADOLINIUM PHOSPHATE GLASS SCINTILLATOR

Suranaree University of Technology has approved this thesis submitted in partial fulfillment of the requirements for the Degree of Doctor of Philosophy.

Thesis Examining Committee

  
\_\_\_\_\_

(Prof. Dr. Rattikorn Yimnirun)

Chairperson

  
\_\_\_\_\_

(Assoc. Prof. Dr. Prapun Manjumn)

Member (Thesis Advisor)

  
\_\_\_\_\_

(Assoc. Prof. Dr. Saroj Rujirawat)

Member

  
\_\_\_\_\_

(Assoc. Prof. Dr. Jakrapong Kaewkhao)

Member

  
\_\_\_\_\_

(Dr. Pinit Kidkhunthod)

Member

  
\_\_\_\_\_

(Assoc. Prof. Dr. Chatchai Jothityangkoon)

Vice Rector for Academic Affairs

and Quality Assurance

  
\_\_\_\_\_

(Prof. Dr. Santi Maensiri)

Dean of Institute of Science

พิศมัย กมลภา : ลักษณะเฉพาะเชิงโครงสร้างและเชิงแสงของแก้วซินทิลเลเตอร์ลิเทียม  
แบบเรียบมแกโดลิเนียมฟอสเฟตที่เจือด้วยซีเรียม (STRUCTURAL AND OPTICAL  
CHARACTERIZATION OF CERIUM DOPED LITHIUM BARIUM GADOLINIUM  
PHOSPHATE GLASS SCINTILLATOR) อาจารย์ที่ปรึกษา : รองศาสตราจารย์ ดร.  
ประพันธ์ แม่นยำ, 120 หน้า.

คำสำคัญ : แก้วฟอสเฟตซินทิลเลเตอร์/ การตรวจจذبรังสี/ ช่วงเวลาการสลายตัวที่รวดเร็ว/วัสดุเรือง  
แสง/ สัมประสิทธิ์การลดทอนเชิงมวล/ ค่าเลขอะตอมยังผล/ ค่าความหนาแน่นอิเล็กทรอนิกส์

งานวิจัยนี้ได้ทำการสังเคราะห์และตรวจวิเคราะห์แก้วลิเทียมแบบเรียบมแกโดลิเนียมฟอสเฟตที่  
เจือด้วยซีเรียมซึ่งมีคุณสมบัติเป็นแก้วซินทิลเลเตอร์ ด้วยมีแรงจูงใจจากความต้องการที่จะเข้าใจกลไก  
การเรืองแสงอย่างลึกซึ้ง เพื่ออธิบายและสามารถนำไปใช้ประโยชน์ได้ดียิ่งขึ้น วัตถุประสงค์สูงสุดของการ  
วิจัยนี้คือการลดเวลาการสลายตัวของแก้วซินทิลเลเตอร์ลง ด้วยอิทธิพลของสารตัวกลางในโครงสร้าง  
ของแก้ว (แกโดลิเนียมออกไซด์และซีเรียมฟลูออไรด์) ต่อลักษณะทางแสงและโครงสร้าง ในการ  
ตรวจสอบโครงสร้างและลักษณะการเรืองแสงของแก้วลิเทียมแบบเรียบมแกโดลิเนียมฟอสเฟตที่เจือด้วย  
ซีเรียมถูกเตรียมด้วยเทคนิค melting quenching ที่อุณหภูมิ 1200 °C แก้วตัวอย่างที่เตรียมได้มีการ  
เรืองแสงวาบออกมาที่ความยาวคลื่น 275 นาโนเมตร ซึ่งเกิดจากแกโดลิเนียมซึ่งจะถ่ายโอนพลังงาน  
ไปยังซีเรียมและเรืองแสงออกมาที่ความยาวคลื่น 343 นาโนเมตร ซึ่งการเรืองแสงนี้เกิดจากการ  
เปลี่ยนระดับชั้นพลังงานจาก 5d-4f ที่มีแถบการเรืองแสงที่กว้างและมีแถบการเรืองแสงซ้อนทับกับ  
แกโดลิเนียม ส่งผลให้ค่าคงที่เวลาการสลายตัวมีค่าน้อย ประมาณ 14-20 ns นอกจากนี้ ยังได้ศึกษา  
ปฏิกิริยาโฟตอนในสารประกอบตัวอย่างแก้วซินทิลเลเตอร์ในงานนี้ เช่น สัมประสิทธิ์การลดทอนเชิง  
มวล ( $\mu_m$ ) ค่าเลขอะตอมยังผล ( $Z_{eff}$ ) และค่าความหนาแน่นอิเล็กทรอนิกส์ ( $N_{eff}$ ) ของแก้วลิเทียม  
แบบเรียบมแกโดลิเนียมฟอสเฟตที่เจือด้วยซีเรียม ซึ่งคำนวณจากทฤษฎีและเปรียบเทียบกับค่าทดลอง  
ซึ่งจะทำให้เราเข้าใจคุณสมบัติของแก้วซินทิลเลเตอร์ที่กล่าวถึงในวิทยานิพนธ์นี้มากขึ้น และเป็น  
แนวทางที่สามารถนำไปใช้ปรับปรุงคุณสมบัติของแก้วซินทิลเลเตอร์อื่น ๆ ในอนาคต

สาขาวิชาฟิสิกส์  
ปีการศึกษา 2565

ลายมือชื่อนักศึกษา พิศมัย กมลภา  
ลายมือชื่ออาจารย์ที่ปรึกษา ดร. ประพันธ์ แม่นยำ

PHITSAMAI KAMONPHA : STRUCTURAL AND OPTICAL CHARACTERIZATION OF CERIUM DOPED LITHIUM BARIUM GADOLINIUM PHOSPHATE GLASS SCINTILLATOR. THESIS ADVISOR : ASSOC. PROF. PRAPUN MANYUM, Ph.D. 120 PP.

Keyword: Phosphate Glass scintillator /Radiation detection /Fast decay time/ Luminescence material/ Mass attenuation coefficient/ Effective atomic number/ Effective electron density

Cerium doped lithium barium gadolinium phosphate glass scintillation properties were investigated to better explain and utilize them. Motivated by a desire to get a deeper understanding of the fluorescence mechanism, the ultimate objective of this research is to reduce the scintillation decay time. The influence of various intermediates (Gadolinium oxide and Cerium fluoride) on the optical and structural characteristics. The luminescence of Ce-doped lithium barium gadolinium phosphate glass was the subject of a study that was prepared by the conventional melt quenching method at 1200 °C. The dominant emissions of our glass sample are at 275 nm from  $Gd^{3+}$ , which transfer energy to  $Ce^{3+}$ , and at 343 nm from allowed 5d-4f transitions. These perturbed ions emit fluorescence in a broad band with a peak at 343 nm and a decay time constant of roughly 14-20 ns for phosphate glass samples in this research. which the performance of  $CeF_3$  as a scintillator that can decrease decay time. in addition, the photon interactions in phosphate glass sample compounds were studied in this work. The interaction parameters of phosphate glass, such as the total mass attenuation coefficient ( $\mu_m$ ), effective atomic number ( $Z_{eff}$ ), and effective electron density ( $N_{eff}$ ), were estimated theoretically and compared to experiment. We expect that the properties of glass discussed in this thesis have been obvious. It will be applied to improve glass material properties for a better scintillator in the next step.

School of Physics  
Academic Year 2022

Student's Signature Prapun Manyum  
Advisor's Signature P. Manyum



## ACKNOWLEDGEMENT

I acknowledge the generous financial support from the Science Achievement Scholarship of Thailand, SAST.

I would like to thank my advisor, Assoc. Prof. Dr. Prapun Manyum, has been a constant source of inspiration and new ideas for me (Many things that have not been done). Inspiration comes from his wonderful words about how to conduct research and study the world. Your encouraging words and thoughtful, detailed feedback have been very important to me. Thank you to the interviewees, who so generously took time out of their schedules to participate in my research and make this project possible, which I aspire to continue throughout my career.

For all of the nice words and assistance you have given to my chairperson, Prof. Dr. Rattikorn Yimnirun, I would like to express my gratitude. His knowledge and diligent editing have benefited me considerably. Since I was a student of yours, you've always had my back and I'm grateful for that.

I would like to thank Assoc. Prof. Dr. Saroj Rujirawat, the professor was the one who pushed me to focus on my research. attempt to get a better grasp on the subject matter so that you can explain it to others or answer their questions.

I'd like to express my gratitude to all who helped me. Assoc. Prof. Dr. Jakrapong Kaewkhao and his students from the Center of Excellence in Glass Technology and Materials Science (CEGM) at Nakhon Pathom Rajabhat University for their support and insightful comments on my research. Even though my time here is limited (2 months), the people I've met so far have been friendly and supportive (and think in the future too). They're extremely lovely, I must say.

The analysis of the attitude survey could not have been completed without Dr. Pinit Kidkhunthod's contribution of experiment in case XAS research data and his willingness to serve as an examination committee member every time.

And I am grateful for other members of beamline in the SLRI, Dr. Narong Janlek was always available to give study and research concept advice (sometimes he urged us to exercise to relax from work or study), and Dr. Yingyot Poo-arporn for give an opportunity did much work on my split work and research, Who has been a good boss for the past four years, he gave me a very good experience for my first job during study in my life.

I am fortunate to have been a part of the Characterization group. Thank you for the fun and support from them.

Most of all, I am grateful for the unwavering, unambiguous, and loving support I have received from my family. None of them asked when I was going to finish the thesis. They don't bother me in the least. They'll be checking in often to make sure I'm alright. "Please let me know if there is anything I can do to help", while talking to them, that's all they use. Although my decisions are respected at all times by them.

Phitsamai Kamonpha



มหาวิทยาลัยเทคโนโลยีสุรนารี

# CONTENTS

	Page
ABSTRACT IN THAI.....	I
ABSTRACT IN ENGLISH.....	II
ACKNOWLEDGEMENTS.....	III
CONTENTS.....	V
LIST OF TABLES.....	VIII
LIST OF FIGURES.....	X
LIST OF ABBREVIATIONS.....	XV
<b>CHAPTER</b>	
<b>I INTRODUCTION.....</b>	<b>1</b>
1.1 Scintillator.....	1
1.2 The way to applied to scintillator and radiation detector.....	3
1.3 Research objectives.....	4
1.4 Scope and limitations.....	4
<b>II THEORETICAL.....</b>	<b>5</b>
2.1 Early history of glass.....	5
2.2 Glass's nature and structure.....	8
2.3 The Phosphate glasses.....	12
2.4 Literature reviews.....	15
2.4.1 Scintillation material component.....	16
2.4.2 Glass composition proportions.....	21
2.5 Luminescence phenomenon.....	25
2.6 Scintillator detector.....	26
2.7 Detection of ionizing radiation.....	27

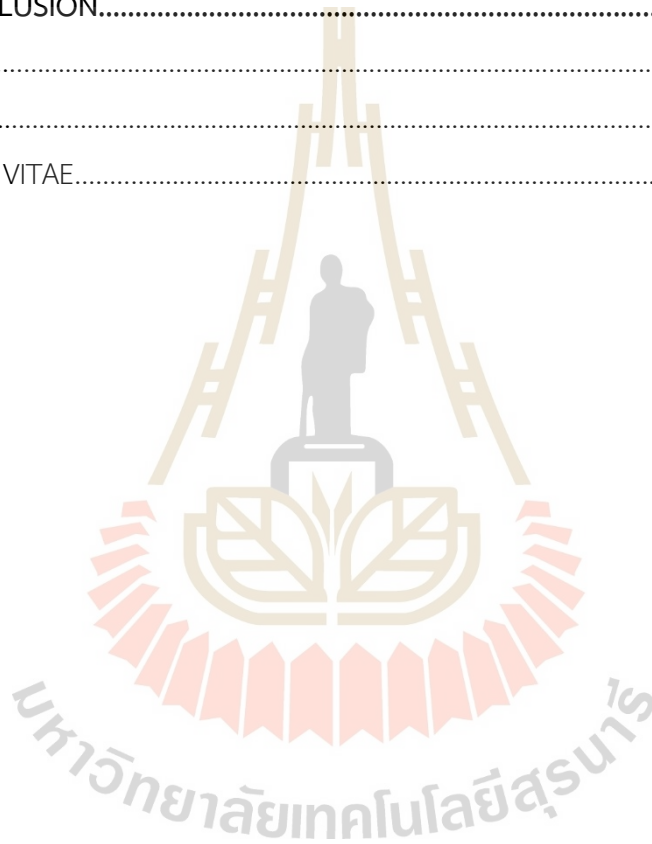


## CONTENTS (Continued)

		Page
	2.8 Materials characterization .....	27
	2.8.1 Density and molar volume.....	28
	2.8.2 Refractive index.....	28
	2.8.3 Scintillator decay times.....	29
	2.8.4 Photoluminescence (PL) .....	29
	2.8.5 UV-Vis.....	31
	2.8.6 Optical band gap.....	32
	2.8.7 X-Ray Diffractometer (XRD) .....	34
	2.8.8 Scanning electron microscopy (SEM) and Energy Dispersive X-Ray Spectroscopy (EDX) .....	35
	2.8.9 X-ray absorption spectroscopy (XAS) .....	36
	2.8.10 Stopping Power and Range of Ions in Matter.....	39
	2.8.11 The Compton coincidence technique (CCT) .....	41
<b>III</b>	<b>RESEARCH PROCEDURE.....</b>	<b>45</b>
	3.1 Preparation of glass samples.....	45
	3.1.1 Raw materials.....	45
	3.1.2 Phosphate glass synthesis.....	46
	3.2 Finding host glass.....	46
	3.2.1 Various concentration of Gadolinium Oxide.....	46
	3.2.2 Various concentration of Cerium Oxide.....	49
	3.3 Measurements.....	51
<b>IV</b>	<b>RESULT AND DISCUSSION.....</b>	<b>58</b>
	4.1 Phosphate host glass 10Li <sub>2</sub> O: 10BaO: xGd <sub>2</sub> O <sub>3</sub> : (80-x) P <sub>2</sub> O <sub>5</sub> ; Li-Ba-xGd (x = 0, 10, 12, 14, 16, 18, 20) .....	59
	4.2 Phosphate glasses 10Li <sub>2</sub> O: 10BaO: xGd <sub>2</sub> O <sub>3</sub> : (79.5-x) P <sub>2</sub> O <sub>5</sub> (x = 8, 10, 12, 14, 16, 18) doped 0.5 mol% of CeF <sub>3</sub> .....	63

## CONTENTS (Continued)

	Page
4.3 Phosphate glasses $10\text{Li}_2\text{O} : 10\text{BaO} : 18\text{Gd}_2\text{O}_3 : (62-x)\text{P}_2\text{O}_5 : x\text{CeF}_3$ ( $x = 0.1, 0.3, 0.5, 1.0, 1.5, 2.0$ ) .....	74
4.4 Radiation attenuation.....	82
<b>V CONCLUSION.....</b>	<b>88</b>
REFERENCES.....	91
APPENDIX.....	97
CURRICULUM VITAE.....	99



## LIST OF TABLES

Table	Page
2.1 The categorized metal oxides based on the field strength (F).....	11
2.2 Main luminescence excitation bands and lines in Cerium, Gadolinium, Europium, and Dysprosium.....	24
2.3 Example of neutron capture cross sections by an isotope. (Thermal neutrons) .....	27
3.1 Gravimetric Factor (GF) is used to create glass samples from precursors	47
3.2 The method for calculating the amount of precursors for used to prepare 61.5P <sub>2</sub> O <sub>5</sub> : 10Li <sub>2</sub> O: 10BaO: 18Gd <sub>2</sub> O <sub>3</sub> : 0.5CeF <sub>3</sub> Phosphate glass sample.....	50
4.1 Code name of samples.....	58
4.2 Data of indirect band gap of samples with various concentration of Gd <sub>2</sub> O <sub>3</sub> of Li-Ba-xGd-0.5Ce.....	62
4.3 Data of indirect band gap of samples with various concentration of Gd <sub>2</sub> O <sub>3</sub> of Li-Ba-xGd-0.5Ce.....	70
4.4 The ratio of oxidation state of cerium.....	72
4.5 The elemental analysis of 10Li <sub>2</sub> O:10BaO: 18Gd <sub>2</sub> O <sub>3</sub> :61P <sub>2</sub> O <sub>5</sub> :1CeF <sub>3</sub> glass.....	76
4.6 Data of indirect band gap of samples with various CeF <sub>3</sub> of Li-Ba-18Gd-xCe phosphate glasses.....	80
4.7 The percentage of energy loss in different energy of He ions interacted with 10Li <sub>2</sub> O:10BaO: 18Gd <sub>2</sub> O <sub>3</sub> :61P <sub>2</sub> O <sub>5</sub> :1CeF <sub>3</sub> glass.....	83
4.8 The weight fractions and density of Li-18Gd-0.5Ce photphase glass.....	86
4.9 The mass attenuation coefficients and Partial interaction of Li-18Gd-0.5Ce photphase glass.....	86

## LIST OF TABLES (Continued)

Table	Page
4.10 The effective atomic numbers and density of electron of Li-18Gd-0.5Ce photphase glass.....	87
5.1 Comparative properties of Li-18Gd-1Ce phosphate glass in this work and commercial.....	88



## LIST OF FIGURES

Figure	Page
1.1 Consider their properties for choosing scintillator materials. (J. WEBER et al., 1995) .....	2
2.1 The Royal Window Northwest Transept Canterbury Cathedral. (ref; <a href="https://sparkypus.com/2020/09/14/canterbury-cathedral-and-the-royal-window/">https://sparkypus.com/2020/09/14/canterbury-cathedral-and-the-royal-window/</a> ) .....	6
2.2 A silicat structure (ref; <a href="https://www.alexstrekeisen.it/english/vulc/index.php">https://www.alexstrekeisen.it/english/vulc/index.php</a> ) .....	7
2.3 Even during process of glass formation, the volume changes as a function of temperature.....	8
2.4 A two-dimensional diagram depicting the structure of an invert glass. Trap and Stevens granted permission for this reprint. © Deutsche Glastechnische Gesellschaft (DGG).....	11
2.5 Glass chemistry development and glass engineering timeline. Green highlights ionic glasses and related materials. (Calahoo and Wondraczek, 2020) .....	12
2.6 Alkali phosphate glasses may include phosphate tetrahedral units.....	13
2.7 The gadolinium electron configuration and diagram. ( <a href="https://valenceelectrons.com/gadolinium-electron-configuration/">https://valenceelectrons.com/gadolinium-electron-configuration/</a> ) .....	18
2.8 The luminescent states are represented on the energy level diagram for $\text{Ln}^{3+}$ ions (except for La, Ce, Pm, and Lu) (Ilichev et al., 2019) .....	19
2.9 The cerium electron configuration and diagram. (Ref; <a href="https://valenceelectrons.com/cerium-electron-configuration/">https://valenceelectrons.com/cerium-electron-configuration/</a> ) .....	20
2.10 Schematic of Jablonski for the mechanism of Fluorescence vs. Phosphorescence. ©2013 Royal Society of Chemistry.....	22
2.11 The forms of the angular dependence functions for s,p, d, and f orbitals with $l = 0, 1, 2, 3$ (Marra, 2016) .....	23

## LIST OF FIGURES (Continued)

Figure	Page
2.12 Schematic of A high-energy photon hits a scintillating crystal, releasing low-energy photons that are converted into photoelectrons and multiplied in a photomultiplier.....	25
2.13 Radiation categorization diagram.....	26
2.14 Luminescence decay curve of glasses. ....	29
2.15 Schematic of photoluminescence spectroscopy measurement system and the electronic levels and transitions.....	30
2.16 (a) and (b)The atomic orbitals and the energy gap required to excite the electron energy state are discussed in detail.....	32
2.17 The Tauc plot is used to calculate the band gap energy ( $E_g$ ). The plot's linear portion is extrapolated to the x-axis.....	33
2.18 Diffraction: Bragg's Law (Kubala-Kuku's et al., 2013) .....	34
2.19 (a) Schematic of the energy dispersive x-ray spectroscopy (EDX) principle in a scanning electron microscope (SEM) and (b) Types of beam-specimen signals ( <a href="https://wiki.aalto.fi/display/SSC/Energy-dispersive+X-ray+spectroscopy">https://wiki.aalto.fi/display/SSC/Energy-dispersive+X-ray+spectroscopy</a> ) .....	35
2.20 (a) Schematic diagram of the characteristic X-ray generation and (b) EDX elemental analysis of a clean PTFE surface.....	36
2.21 The diagram of an atom absorbing an x-ray and ejecting a core electron into the continuum.....	37
2.22 SRIM window of input parameters for stopping calculation.....	40
2.23 (a) The schematic of kinematics of Compton Scattering (Limkitjaroenporn et al., 2010) and (b) The strength of each of the three forms of gamma ray interactions relies on initial gamma ray energy and Z of the material (Parks, 2015) .....	42



## LIST OF FIGURES (Continued)

Figure	Page
3.1 A schematic overview of synthetic glass samples, from precursors preparation to sample preparation for characterization-ready dimensions.....	48
3.2 The bulk glass sample of phosphate-host glass with varying $Gd_2O_3$ concentrations.....	49
3.3 The glass samples with various concentrations of $Gd_2O_3$ after cut and polished.....	51
3.4 The bulk glass samples with various concentrations of $CeF_3$ .....	51
3.5 (a) Density measurement kit (A&D HR-200) 4-digit Microbalance with density kit and (b) Multi wavelength Abbe refractometer (ATIGO-3T) (Refractive Index measurement from 1.3-1.7) ( <a href="http://dept.npru.ac.th/cegm/index.">http://dept.npru.ac.th/cegm/index.</a> ) .....	52
3.6 (a) Fluorescence Spectrophotometer (Cary-Eclipse)(Photo-luminescence measurement of material in visible region from 200 - 900 nm) and (b) UV-VIS spectrophotometer (Cary-50) (and %T measurements in the range of 200-1100 nm with CIE $L^*a^*b^*$ color coordinate software) .....	53
3.7 X-Rays Induced Optical Luminescence (Radioluminescence) (Inel x-ray generator with 2 kW Cu-anode) (Spectrum detected by fiber optics spectrometer, QE65000 Ocean Optics) (Radioluminescence measurement of material in visible region from 200 - 900 nm) .....	54
3.8 (a) Bruker D2 PHASER and (b) FE-SEM/WDX/EDX (JEOL JSM 7800F) .....	55
3.9 Current SUT-NANOTEC-SLRI beamline setup at BL5.2 ( <a href="https://www.slri.or.th/en/sut-nanotec-slri.html">https://www.slri.or.th/en/sut-nanotec-slri.html</a> ) .....	56
3.10 Schematic of the Compton scattering technique for mass attenuation coefficient measurement (Limkitjaroenporn et al., 2013) .....	57

## LIST OF FIGURES (Continued)

Figure	Page
4.1 (a) The density and molar volume of Li-Ba-xGd phosphate glasses and (b) The refractive index of Li-Ba-xGd phosphate glasses.....	59
4.2 The transmission curves of Li-Ba-xGd phosphate glass.....	60
4.3 The optical band gap of Li-Ba-xGd for (a) Indirect band gap and (b) Direct band gap.....	61
4.4 (a) PL result of spectra of Gd <sup>3+</sup> excitation (b) Radioluminescence spectra of Li-ba-xGd phosphate glasses at room temperature.....	62
4.5 XRD pattern of Li-Ba-xGd-0.5Ce at x=18 mol% phosphate glass sample...	64
4.6 (a) The density and molar volume of Li-Ba-xGd-0.5Ce phosphate glasses and (b) The refractive index of Li-Ba-xGd-0.5Ce phosphate glasses.....	65
4.7 The photoluminescence (PL) results show two distinct spectra for the Li-Ba-xGd-0.5Ce phosphate glasses: (a) excitation spectra of Gd <sup>3+</sup> and (b) excitation and emission spectra of Ce <sup>3+</sup> .....	66
4.8 (a) The percentage of the area under the emission peak in the excitation spectrum was analyzed for varying concentrations of Gd <sub>2</sub> O <sub>3</sub> . (b) A partial energy level diagram was presented to illustrate the potential energy transfer pathways from Gd <sup>3+</sup> ions to Ce <sup>3+</sup> ions in both Li-xGd-0.5Ce and Li-18Gd-xCe phosphate glass systems.....	67
4.9 (a) Radioluminescence spectra of Li-ba-xGd-0.5Ce phosphate glasses at room temperature and (b) zoom in in emission rang of Ce <sup>3+</sup> .....	68
4.10 (a) The transmission curves and (b) optical band gap of Li-Ba-xGd-0.5Ce.....	69
4.11 (a) Linear combination fit of XANES at Ce L <sub>3</sub> -edge of Li-Ba-xGd-0.5Ce phosphate glass. (b) The mechanism luminescence of Ce doped.....	70
4.12 The scintillation pulse shapes of Li-Ba-xGd-0.5Ce phosphate glasses.....	73
4.13 XRD pattern of Li-Ba-18Gd-xCe at x = 1 mol% phosphate glass sample.....	74
4.14 (a) The density and molar volume of Li-Ba-18Gd-xCe phosphate glasses and (b) The refractive index of Li-Ba-18Gd-xCe phosphate glasses.....	75

## LIST OF FIGURES (Continued)

Figure	Page
4.15 (a) SEM image surface and (b) EDX elemental analysis surface of 10Li <sub>2</sub> O:10BaO: 18Gd <sub>2</sub> O <sub>3</sub> :61P <sub>2</sub> O <sub>5</sub> :1CeF <sub>3</sub> glass.....	76
4.16 (a) The spectra of Gd <sup>3+</sup> excitation and (b) spectra of Ce <sup>3+</sup> excitation and emission of Li-Ba-18Gd-xCe phosphate glasses.....	77
4.17 The percent of area under the peak for emission of excitation spectrum at different concentration of CeF <sub>3</sub> .....	78
4.18 (a) The transmission curves and (b) The optical band gap of Li-Ba-18Gd-xCe phosphate glasses.....	79
4.19 The scintillation pulse shapes and decay time component of Li-Ba-18Gd-xCe (x = 0.1, 0.3, 0.5,1.0, 1.5, 2.0) phosphate glass.....	81
4.20 Ion distribution of 10Li <sub>2</sub> O:10BaO: 18Gd <sub>2</sub> O <sub>3</sub> :61P <sub>2</sub> O <sub>5</sub> :1CeF <sub>3</sub> glass in different energy of 4He ions of (a) 100 keV, (b) 500 keV and (c) 1000 keV.....	82
4.21 The typical Cs <sup>137</sup> at 0.662 MeV (662 keV) for transmitted (I) gamma-rays intensities of 10Li <sub>2</sub> O:10BaO:18Gd <sub>2</sub> O <sub>3</sub> :61.5P <sub>2</sub> O <sub>5</sub> :0.5CeF <sub>3</sub> (Li-18Gd-0.5Ce) glass are scatted at different angles.....	83
4.22 A typical energy spectrum for Cs-137 gamma rays scattered at an angle of 120° relative to the direction of the gamma rays being emitted from the source. , The incident (I <sub>0</sub> ) (in red line) and transmitted (I) (in blue line) gamma-rays intensities of 10Li <sub>2</sub> O: 10BaO:18Gd <sub>2</sub> O <sub>3</sub> :61.5P <sub>2</sub> O <sub>5</sub> :0.5CeF <sub>3</sub> (Li-18Gd-0.5Ce) glass.....	85

## LIST OF ABBREVIATIONS

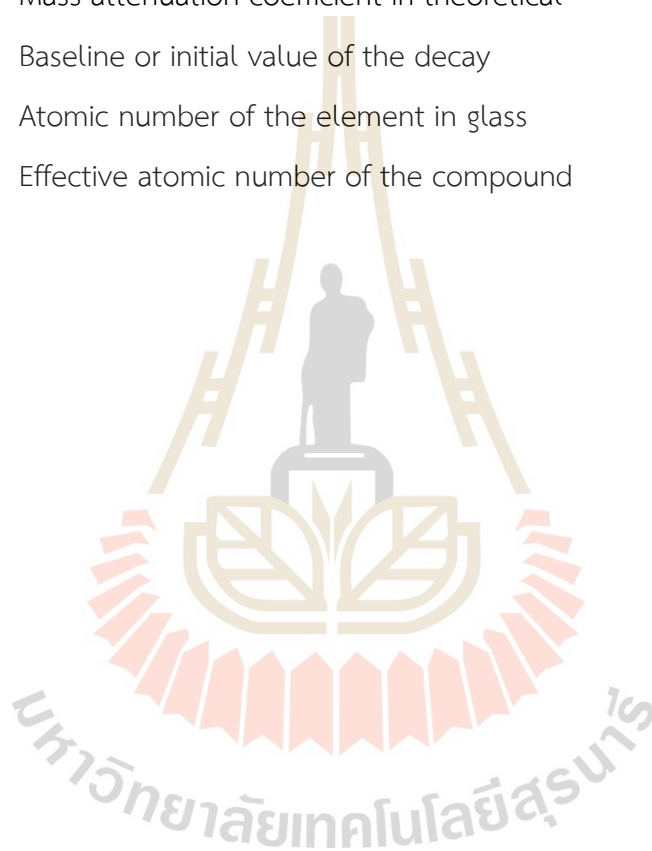
$a^2$	Area of the plates
$^{\circ}\text{C}$	Degree Celsius
$A_1, A_2$	Amplitudes of the two decay processes
BL5.2	Beamline 5.2
BOs	Bridging Oxygens
$c$	Velocity of light
CCT	Compton coincidence technique
CRI	Color Rendering Index
DBOs	Doubly Bonded Oxygens
$E$	Incident X-ray energy
$E_0$	Threshold energy
$E_B$	Core electron's binding energy
$E_g$	Energy of the optical band gap
$E_k$	Photoelectron's kinetic energy
EDX	Energy-dispersive X-ray spectroscopy
$F$	Field strength
eV	Electron-volt
$I$	Light intensity
$I_0$	Light reference intensity
$I(t)$	intensity or amplitude of the decay at time $t$
$mc^2$	Rest mass of an electron (511keV)
MW	Molar weight
NBOs	Non-Bridging Oxygens
$r$	Power factor of transition mode
$S_0$	Singlet ground state
$S_1$	Singlet excited state
$T_1$	Triplet excited state

## LIST OF ABBREVIATIONS (Continued)

$T$	Kauzmann temperature
$T_g$	Glass transition temperature
$T_m$	Melting temperature
SRIM	Stopping Power and Range of Ions in Matter
UV-Vis	UV-visible spectroscopy
$v$	Velocity of light in a matter
$V_m$	Molar volume
$W_{air}$	Weight of sample in air
$W_{liq}$	Weight of displaced liquid
XRD	X-ray diffraction
XANE	X-ray Absorption Near Edge Spectroscopy
XAS	X-ray absorption spectroscopy
$Z$	Atomic number
$Z_c$	Characteristic impedance
$\alpha$	Absorption coefficient
$\beta$	Band tailing parameter
$C$	Concentration
$E_\gamma$	Incident gamma ray energy
$E_\gamma'$	Scattered gamma ray energy
$h\nu$	Photon energy
$k$	Electron's wave vector
$K$	Pair production
$\lambda$	Wavelength
$\lambda_{Em}$	Emission wavelength
$\lambda_{Ex}$	Excitation Wavelength
$n'$	Refractive index
$\rho$	Density
$\tau_1, \tau_2$	Decay constants

## LIST OF ABBREVIATIONS (Continued)

$\sigma$	Compton
$\sigma_{t,el}$	Total electronic cross-section
$\tau$	Photoelectric
$\mu_{mE}$	Mass attenuation coefficient for experiment
$\mu_{mt}$	Mass attenuation coefficient in theoretical
$\gamma_0$	Baseline or initial value of the decay
$Z_i$	Atomic number of the element in glass
$Z_{eff}$	Effective atomic number of the compound





# CHAPTER I

## INTRODUCTION

In this part of the discussion, we will talk about the purpose of the research, which will include a brief explanation of why we are interested in this topic and what elements will obviously need to be worked upon. It is my hope that the reader will continue to be interested in this research after they have completed reading this section, which contains brief material that is comparable to conclusions in research.

### 1.1 Scintillator

Historically, the scintillator substance was employed. Which A scintillator is a substance that shows scintillation, the luminescence property. Scintillators are substances that transform high-energy radiation, such as X-rays or gamma rays, into near-visible or visible light. They are usually applied in medical diagnostics, high-energy physics, and geophysical exploration as detectors.

The last time this material has inspired curiosity and investigation for numerous applications. Most of the past research look at the requirements for scintillator materials in a variety of different applications, the characterization and attributes of scintillators, and the current state of our understanding of the factors that influence scintillator performance. In furthermore, the process and efficiency of a scintillator involve the absorption of incident radiation or particles by the host and their conversion into thermalized electrons and holes, the transfer of a fraction of the electron and hole excitation to luminescence centers, and the luminescence process.

When understood, the physics of scintillator will allow for the improvement and development of the material for several applications. When choosing materials for a certain application, certain properties of scintillator materials need to be taken into consideration then show in figure 1.1. In this study, we were interested in the form of material that has a large different shape and a low price relative to the price of raw

materials, preparation, high transparency, a short decay time, stability in the atmosphere, UV-emitting emission, and detectors for high energy. This glass material will attract attention.

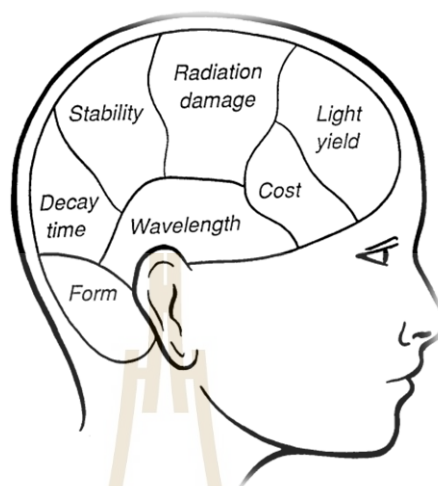


**Figure 1.1** Consider their properties for choosing scintillator materials (J. WEBER et al., 1995).

The scintillator devices, as well as the functions of scintillator and radiation detection are the center of this study, and phosphate glass is a kind of glass interested because of its unique physical and chemical features, as well as its good structural properties, such as a low phonon energy when compared to other glass types. Phosphate glass also has a low refractive index, a high thermal expansion coefficient, a low melting point, a low glass transition temperature, a low viscosity, a high UV transmission, and a high transparency. These properties are advantageous for optical devices such as scintillators, radiation detectors, and radiation shielding windows made of developed glass (Chanthima et al., 2018). That from the phosphate glass structure is capable of containing various compounds, such as rare earth elements, with specialized applications deriving from these elements. While they are transparent in high concentrations of rare earth element, that features of high contain other element make phosphate glass are to enhanced materials, such as density, decay time, emission wavelength, and material stability. In addition, they can be manufactured by the conventional melting method at low temperatures. That features of phosphate glass,

such as density, decay time, emission wavelength, and material stability, are advantageous to enhanced materials. However, the phosphate glass has a defect is sensitive to moisture, this problem will be tried by put BaO on phosphate structure and when we add high contain of rare earth melting point of phosphate glass are increase, we fixed this problem by add LiO<sub>2</sub> in glass structure for reduce temperature to synthesis.

## 1.2 The way to applied to scintillator and radiation detector

The process of light generated from ionizing radiation is explained by scintillators, which are materials function is to convert high-energy radiation such as X or gamma-rays to near-visible or visible light. High physical density and high stopping power of the host lattice, high light yield from the scintillation process, fast decay time, low afterglow value, linearity of the light output (excitation for good energy resolution), ease of machining, hardness, spectral match with the photodetector, and so on are all characteristics of an excellent scintillator (Ronda and Jüstel, 2008). Doping rare earth ions can improve these properties. According to reports, due to electronic excitation and light emission throughout the UV-visible light spectrum range by rare earth ions in the glass structure, rare-earth doped phosphate glass has a great potential for scintillator application. (Ronda and Jüstel, 2008).

Therefore, the rare-earth doped phosphate glass with Gd ion might be a promising candidate for the scintillator applications. On the other hand, cerium also exhibits essential properties in order to enhance scintillator performance such as fast decay time (ns) due to short distance of electron transition from 5d→4f state, and a good activator ion (accepter) in energy transfer mechanism (Ronda and Jüstel, 2008). In this work, we doped Ce in phosphate glass with Gd ion in order to improve the scintillator performance. The cerium ion could enhance the scintillation properties of the phosphate glass with Gd ion.

### 1.3 Research objective

We really would like to improve the Lithium Barium Gadolinium Phosphate glass doped Cerium for scintillator and shielding material. Then the objectives of works are:

1.3.1 The melt-quenching process can be used to synthesize Lithium Barium Gadolinium Phosphate glass doped Cerium.

1.3.2 The glass samples are able to detect large levels of energy and emission in the visual spectrum.

1.3.3 The short distance between the  $5d4f$  and  $5d4f$  states of cerium, the decay time of glass samples doped with cerium will be reduced in the nanosecond range.

1.3.4 The glass sample has the ability to either attenuated radiation or have radiation shielding properties.

### 1.4 Scope and limitations

1.4.1 The purpose of this study is to synthesize Lithium Barium Gadolinium Phosphate glass doped Cerium using the melt-quenching process.

1.4.2 The optical properties and structure of Lithium Barium Gadolinium Phosphate glass doped Cerium will be characterized using refractive index, ultraviolet-visible, optical band gap, photoluminescence, radioluminescence, and decay time for the optical properties, and XRD, XAS, and EDX for the structure and chemical composition, respectively.

1.4.3 The Compton coincidence technique (CCT) will be used to assess the radiation detection of the glass samples.

## CHAPTER II

### THEORETICAL

The purpose of this section is to discuss a brief history of glass, as the adage goes "To understand science, one must first understand its history; Auguste Comte," the fundamental glass components and their relationship to glass structure and properties, and the goal of developing glass material for glass scintillators.

#### 2.1 Early history of glass

Glass is an old substance with a lengthy history. Both those that are caused by nature, such as lightning, volcanic and those that are created by humans. Glassmaking was discovered in Eastern Mesopotamia around 3500 BC. The earliest glasses were inspired to produce decorative things, maybe to resemble gem and semiprecious stones (natron) by using sintered bodies of silica and desert soda (natron). Making glass in the past was difficult and time-consuming. Glass melting furnaces have a limited size and temperature range; they are small and produce temperatures below melting point. Until first century BC, Syrian artisan developed the blow pipe. This breakthrough made glass processing easier, faster, and less expensive. Alexandria, Egypt, has been the most important location of glass making around 1000AD. The remarkable skill of colored glass making on churches and cathedral across Europe exerted a strong influence in the greatest Chartres and Canterbury cathedral windows produced in the 13th and 14th centuries then shown in figure 2.1.

In the Middle Ages, practically all raw materials had a soda-lime silica composition, and two separate sources of alkali were affected: first, natron (hydrated  $\text{Na}_2\text{CO}_3$ ) from the Eastern Mediterranean littoral, and second, plant ash from Mesopotamia, which had higher  $\text{K}_2\text{O}$  and  $\text{MgO}$ . Because of the impurities present, much glass created in the Middle Ages was dark green, dark brown, or virtually black. As a result, some attention was paid to the purification of raw materials.

It led to "L' Arte Vertraria," written by Antonio Neri, an Italian priest and glassworker, in 1672, becoming one of the most important sources of glass technology during this period. That the structure information regarding glasses made from purified raw material is quite evident (Kurkjian and Prindle, 1998).

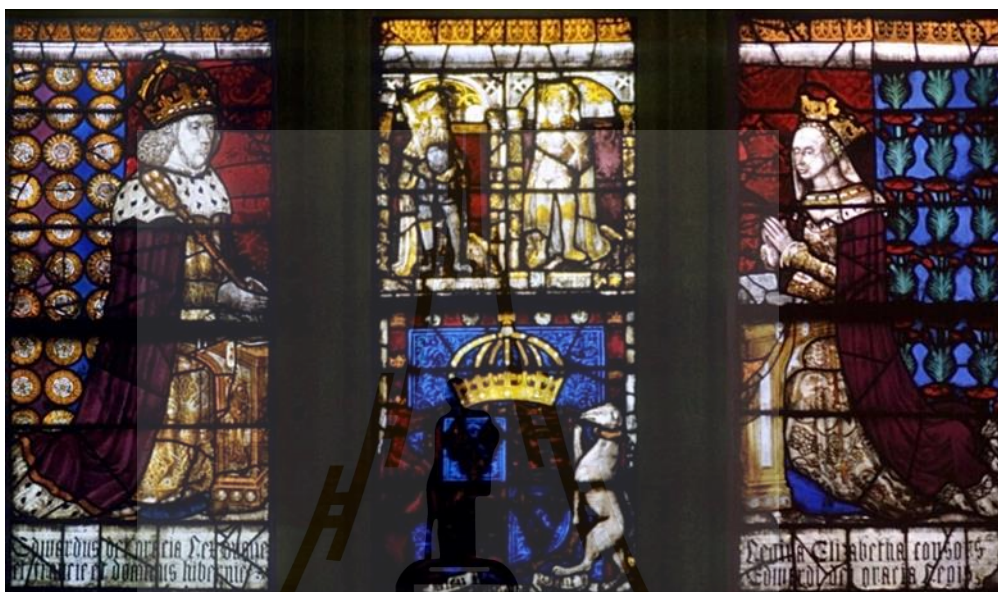


**Figure 2.1** The Royal Window North West Transept Canterbury Cathedral.  
(ref; <https://sparkypus.com/2020/09/14/canterbury-cathedral-and-the-royal-window/>).

The 17th and 18th centuries saw a surge in scientific curiosity, with experts such as Galileo and Kepler pushing for improvements in optical instruments, particularly telescopes. The development of new glasses in the late 19th century was essentially a matter of chance discovery and isolation of new elements, the fabrication of heavy glasses, and improved laboratory glassware made of borosilicate glass. Furthermore, to examine glass network structure in 1936, and they were the first to establish a simple glass network structure, which is showed in figure 2.2. Silicate glasses are made up of silicon dioxide ( $\text{SiO}_2$ ) molecules that are connected through oxygen atoms to form a network structure. The network structure of silicate glasses is similar to that of the crystalline form of silicon dioxide, which is known as quartz. However, in the glass state, the atoms are arranged in a disordered manner, without any long-range periodic order. In a silicate glass, each silicon atom is bonded to four oxygen atoms, and each



oxygen atom is bonded to two silicon atoms. This results in a three-dimensional network structure, where the silicon and oxygen atoms are interconnected through shared corners, forming a tetrahedral arrangement. The tetrahedral arrangement is the basic building block of the silicate network structure and is repeated throughout the glass structure.

The silicate glass network structure can be modified by introducing other elements or ions into the network, such as aluminum, boron, or sodium, which can replace some of the silicon or oxygen atoms. These modifications can result in changes to the glass properties, such as its refractive index, density, and chemical resistance.

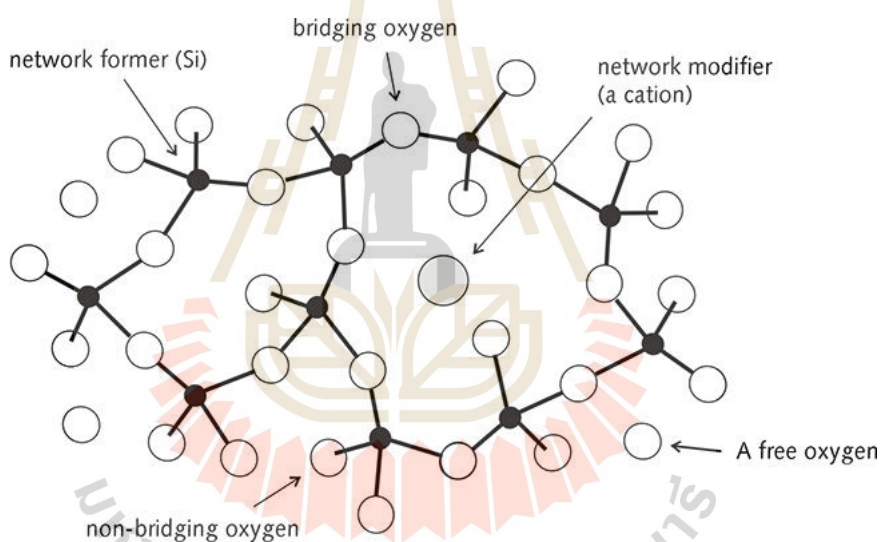


**Figure 2.2** A silicate structure (ref:<https://www.alexstrekeisen.it/english/vulc/index.php>)

Understanding the first established simple glass network structure, which is a silicate structure, has been crucial in the development of new glasses with specific properties for different applications, optimization of glass production processes, and development of new applications for glasses.

## 2.2 Glass's nature and structure

Glass is often formed when a molten mass is rapidly cooled below the crystallization temperature, and solidification begins when the material approaches the glass transition point. As illustrated in Figure 4, this process is typically represented in terms of changes in enthalpy or volume as a function of temperature, respectively. A continuous decrease in the temperature of the molten mass starting at point A in figure 2.3 results in a continuous decrease in the volume of the molten mass along the line AB. Then, as the temperature cools slowly, the volume decreases abruptly, and crystallization at the melting point occurs along the BC. Further cooling leads in a progressive change in volume with the creation of crystalline phases along the line CD as a result of the formation of crystalline phases. However, rapid cooling eliminates

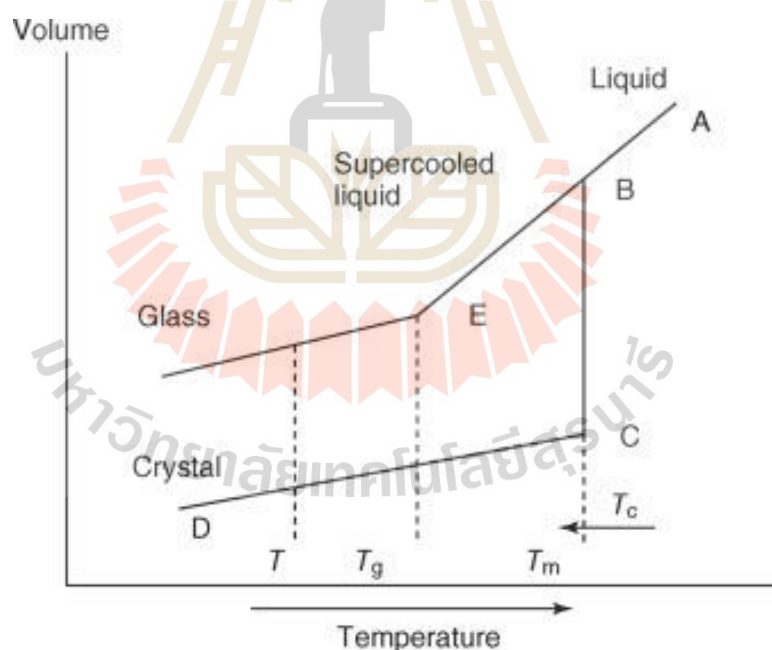


**Figure 2.3** Even during process of glass formation, the volume changes as a function of temperature.

The possibility of crystallization; instead, a supercooled liquid is produced, and the volume change will follow the line BE. As the melt cools to room temperature,

the viscosity of the melt increases, making it impossible for the atoms to be placed in a long-range ordered arrangement (symmetrical units of grouped atoms), resulting in the development of a glass. The temperature difference between the temperature of the supercooled liquid and the temperature of the frozen solid (glass) is referred to as the glass transition temperature, or  $T_g$  for short. (Abou Neel and Knowles, 2009).

Zachariasen's Rules for Glass Formation (1932), which were based on an empirical observation of oxides, were developed. In general, for glass formation to take place, all four requirements must be met at the same time.

The first rule states that an oxygen atom cannot be connected to more than two cations at the same time. This means that each oxygen atom can only form a limited number of chemical bonds with cations, which is important for the overall structure of the glass.

The second rule states that the cation coordination number, which refers to the number of oxygen atoms bonded to a cation, should be in the low three or four range. This is important for maintaining the structural stability of the glass, as a coordination number that is too high can result in an unstable structure.

The third rule states that the oxygen polyhedra, which are the groups of oxygen atoms bonded to a cation, should share only their corners and not their edges or faces. This is important for maintaining the structural integrity of the glass and preventing it from breaking apart.

The fourth and final rule states that in 3D networks, at least three corners must be shared by two or more nodes. This ensures that the structure of the glass is interconnected and stable.

Zachariasen's Rules for Glass Formation provide important guidelines for the creation of glass structures and help to ensure that the resulting glass is stable and structurally sound. These rules are still used by researchers today in the development of new glass materials for a wide range of applications.

In general, for glass formation to take place, all four requirements must be met at the same time. Combined with the low coordination numbers and corner-sharing principles, this suggests that glass production is more likely when polyhedral structures are open and low in density. Subsequently in 1942, Dietzel categorized the primary component oxides into three categories: network formers, network modifiers, and intermediates and examined at direct Coulombic interactions and categorized metal oxides based on the strength of the electromagnetic field ( $F$ ), which is depicted in table 2.1 below. In metal oxide bonds, field strength is related to the ionicity of the bonds, with low field strength bonds having a high amount of ionic character and high field strength bonds having a high amount of covalency or directionality to their bonding environment, respectively.

The first type of network former. The essential glass forming oxides, that is a positively charged ion, often known as "network formers," are the first.  $\text{SiO}_2$ : $\text{Si}^{4+}$ ,  $\text{B}_2\text{O}_3$ : $\text{B}^{3+}$ ,  $\text{GeO}_2$ :  $\text{Ge}^{4+}$ , and  $\text{P}_2\text{O}_5$ : $\text{P}^{5+}$  are examples of triangular and tetragonal coordination. Figure 2.4 shows a two-dimensional schematic demonstrating the structure of an invert glass, which represents the models of the basic components of glass. Permission was obtained for this reprint by Trap and Stevels.

The second type of network modifier is alkalis and alkaline earth ions, which have an intermediate electronegativity and do not form ionic connections. The network-modifying unit is  $\text{M}_2\text{O}$  ( $\text{M}=\text{Li}, \text{Na}, \text{K}, \text{Rb}, \text{Cs}$ ). They change the continuous network former by breaking bridging oxygens (BOs) and forming negatively charged non-bridging oxygens (NBO). Warren and Bischoe (1938) used a continuous random network (CRN) model of sodium silicate and discovered that the NBO's negative charge is balanced by the positively charged alkali cation to maintain charge neutrality then show in figure 2.4.

The third type of intermediates, which account for a lesser portion of the total. They do not form glasses on their own, but when connected with other components, they behave as network form.

**Table 2.1** The categorized metal oxides based on the field strength (F).

Glass structure	Field strength ( $F$ ) = $\frac{Z_c}{a^2}$
Network formers	> 1.3
Network modifiers	< 0.4
Intermediates	$0.4 \leq F \leq 1.3$

From the above information It can be seen that there are many types of glass. In general, they are separated using glass forming oxide, and each kind is developed for a given device by doping some element on this structure. Figure 2.5 shows that we are in the third generation of inquiry and process design for machine learning glass science.

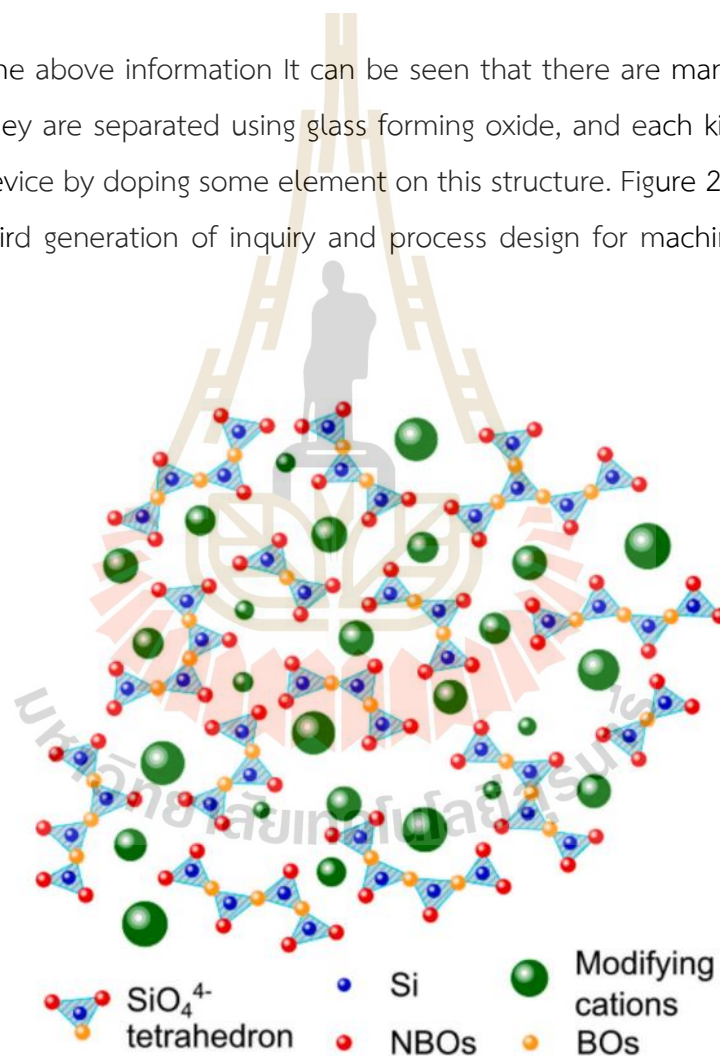


**Figure 2.4** A two-dimensional diagram depicting the structure of an invert glass. Trap and Stevens granted permission for this reprint. © Deutsche Glastechnische Gesellschaft (DGG).

The optical devices like phosphate glass were reported around 100 years ago by Schott and co-workers, they developed phosphate glasses with low dispersion and relatively high refractive indices (compared to silica-based optical glasses) for achromatic optical elements. When compared to silicate glasses, alkaline earth phosphate glasses have outstanding transparency for ultraviolet (UV) light, prompting additional research (Brow, 2000), on the other hand, has a low chemical resistance. It is hydrophilic in nature, which makes the development of this kind of glass difficult.

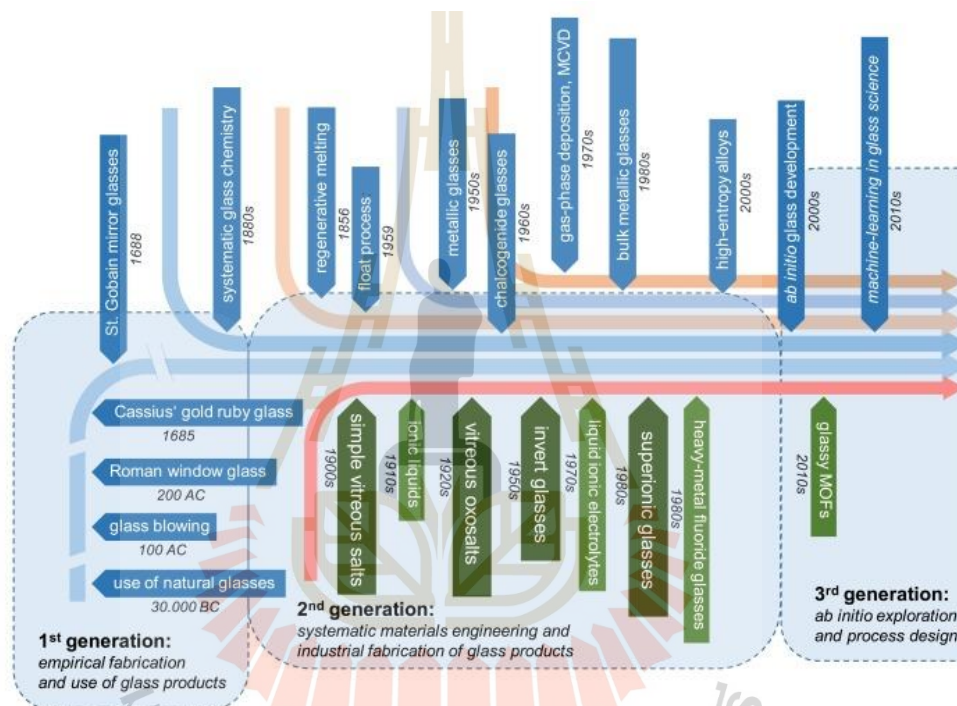


**Figure 2.5** Glass chemistry development and glass engineering timeline. Green highlights ionic glasses and related materials. (Calahoo and Wondraczek, 2020).

### 2.3 The Phosphate glasses

The Phosphate glass for used as optical glasses based on phosphorus pentoxide ( $P_2O_5$ ) is a type of glass that contains phosphate. The P-tetrahedra that are produced as a direct consequence of the P outer electrons' involvement in the production of  $sp^3$  hybrid orbitals ( $3s^2, 3p^3$ ). Covalent bridging oxygens connect these tetrahedra to generate a variety of phosphate anions. Each phosphor ion confines three



bonded oxygens and one doubly bonded oxygen in the network of phosphate glasses, which is made up of  $\text{PO}_4$  tetrahedra. (Van Dongen and Oomen, 1989). All of these tetrahedra have at least one terminal oxygen, that is not connected to another phosphate unit. Although the  $\text{Q}^3$  unit (a phosphate tetrahedron with three bridging oxygens and one terminal oxygen) is the most basic unit of a phosphate glass, there are three more types of  $\text{Q}^i$  tetrahedra to consider:  $\text{Q}^2$ ,  $\text{Q}^1$ , and  $\text{Q}^0$ , where  $i$  designates the number of bridging oxygens (BO) on each  $\text{PO}_4$  unit. Each  $\text{PO}_4$  tetrahedron's remaining  $(4-i)$  oxygens are terminal. Figure 2.6 illustrates these structures. Only  $\text{Q}^3$  tetrahedra have doubly bonded oxygens (DBOs), while the other Q-species' terminal oxygens are all non-bridging oxygens (NBOs) (Brow and WITTENAUER, 2002). And the  $\text{P}_2\text{O}_5$  is indicated as a precursor to phosphate glass formation. which is a prototype This 'random network'

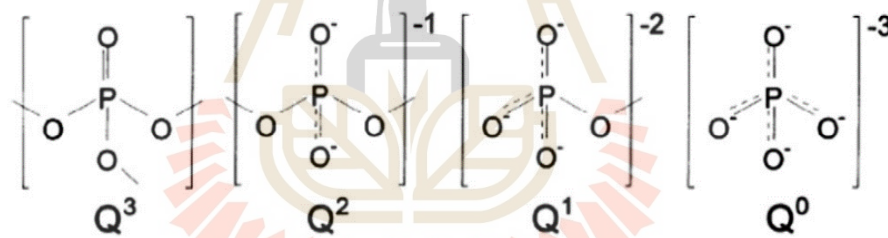


Figure 2.6 Alkali phosphate glasses may include phosphate tetrahedral units.

Around one hundred years ago, Schott and his collaborators created phosphate glasses for achromatic optical elements. These glasses had low dispersion and relatively high refractive indices in comparison to silicate-based optical glasses. Rare earth doped on silicate germinate, and phosphate glass were studies on 1989 by E.W.J.L. OOMEN and A.M.A. van DONGEN. They examined the effect of various network formers, network modifiers, network modifier concentrations, and network former concentrations. The thermal history of the phosphate glasses structure differs from other glasses (germinate, borate, and silicate glass due to the fact that the network is constructed from  $\text{PO}_4$  tetrahedra, and each phosphor ion contains three bonding



oxygens in addition to one oxygen that is doubly bound, Phosphate glasses, as a direct consequence of this phenomenon, have a preference to form chains as opposed to a three-dimensional network, with the modifier ions occupying spaces in between the chains that they generate. These sites are incorporated into the network voids produced by the network founder oxygen ions (Van Dongen and Oomen, 1989). After that many researchers are interested in phosphate host glasses doped with rare earth due to their low photon energies, great transparency, radiation absorption, and visible-length luminescence. The amorphous form of glass provides the benefit of a huge quantity of free volume, a broad chemical ratio range. In addition, the presence of several rare earth sites in glass is responsible for the inhomogeneous broadening of spectra caused by this glass and when comparing the half-bandwidth of the  ${}^7F_0 \rightarrow {}^5D_0$  transition in an europium sesquioxide crystal, which is about  $2 \text{ cm}^{-1}$ , to the half-bandwidths of these transitions in glasses, which are  $119 \text{ cm}^{-1}$  in phosphate glass. Then the enhancement of the radiative transfer characteristic is appropriate. The phosphates host glass is a type of glass that is already highly transparent and is doped with certain elements, such as rare earth, to improve performance (Weber, 1990).

The properties of phosphate glass are dependent on the phosphate tetrahedral structure, which consists of one, two, three, and four non-bridging phosphate tetrahedrons that can integrate high levels of lead to improve the refractive index of a certain element. Due to these characteristics, lasers and other photonic glass devices were able to be built and researched (Fletcher et al., 2011). In addition, phosphate glass is simple to fabricate and form due to its low-temperature melt-quenching synthesis.

The advantage of phosphate glass has several unique properties that make it useful for various applications. It has a high refractive index, which makes it useful for optical applications such as fiber optics. It also has a low melting point, making it easy to work with and form into different shapes (R. K. Brow., 2000). Additionally, phosphate glass is biocompatible, and it can be modified to be bioactive, meaning it can bond with bone tissue and promote bone growth. This makes it useful for medical applications such as bone implants (M. C. Veeramachaneni et al., 2012).

Phosphate glass can also be used as a radiation detector (G. W. Arnold et al., 1995), where it is used to detect ionizing radiation. When ionizing radiation interacts with the glass, the phosphorus atoms in the glass absorb the energy and release it in the form of visible light, which can be detected and measured. Overall, phosphate glass is a versatile material with many unique properties that make it useful in a wide range of applications, from optical fibers and solid-state lasers to bioactive glass and radiation detectors.

## 2.4 Literature reviews

Theoretical data necessary for understanding features of glass materials such as luminescence phenomena, scintillator mechanism, and how to characterize glass materials in order to prove and improve the glass material. Below, we've attempted to give only the most important data that we used in our research.

Scintillation materials are typically composed of a scintillating compound or crystal and a dopant material. The scintillating material is the component that absorbs the energy of incoming radiation and produces light photons that can be detected by a photodetector. The dopant material is added to enhance the properties of the scintillating material, such as its light yield, decay time, and energy resolution. There are many types of scintillating materials used in radiation detection, including inorganic crystals, organic liquids, plastics, and glasses. Inorganic crystals such as sodium iodide (NaI), Caesium iodide (CsI), and lutetium oxyorthosilicate (LSO) are commonly used in gamma ray detection, while organic materials such as anthracene and stilbene are used in neutron detection.

Phosphate glass scintillators have gained attention due to their potential advantages over traditional scintillators, particularly in the field of radiation detection. Phosphate glass scintillators have a high light yield, which means they produce more visible light photons per unit of energy deposited in the material (G. W. Arnold et al., 1995). This can improve the sensitivity and energy resolution of radiation detectors, allowing for more accurate measurements of the energy and intensity of incoming radiation. In addition, phosphate glass scintillators have a relatively fast response time

and short decay time, which means they can detect radiation events and recover quickly to detect subsequent events. This can be particularly useful in high-rate applications such as nuclear physics experiments and medical imaging. Phosphate glass scintillators also have good radiation hardness, meaning they can withstand exposure to ionizing radiation without significant damage to their properties. This makes them suitable for use in harsh radiation environments such as nuclear reactors and particle accelerators. Overall, phosphate glass scintillators have shown promising performance in radiation detection applications and are an active area of research and development.

#### 2.4.1 Phosphate glass scintillation material component

This section describes why we should add specific materials or elements to the structure of the glass phosphate in order to optimize the advantages that we achieve when attempting to synthesize scintillator glass or shielding devices. Alternatively, what may be done to resolve the problem in our scintillator host glass.

**2.4.1.1 Lithium Oxide** Since the late 1950s, lithium has been used in glass components for scintillation materials. When they were first developed, cerium-activated lithium silicate glass scintillators have been used in a wide variety of applications relating to the detection of radiation. The chemical formula for lithium oxide is  $\text{Li}_2\text{O}$ , the molar mass of this compound is 29.88 g/mol. The  $\text{Li}_2\text{O}$  functions as a network modifier and is crucial to the basic structure of glass, it's a lithium source that is both thermally stable and difficult to degrade, and it can improve heat-shock resistance and thermal-mechanical qualities (Guo et al., 2020). And can be used to manufacture ceramics and glass. In addition, lithium oxide can produce a spectrum pattern that increases in intensity, which makes it an attractive flux for use in glass structures and  $^6\text{Li}$  is the most common application of a neutron capture element with a high thermal neutron cross-section (Zaman et al., 2017).

**2.4.1.2 Barium Oxide** is a common dopant used in phosphate glass scintillators for radiation detection. When added to the glass, it can improve the scintillation properties of the material, such as light yield, energy resolution, and decay time. Barium oxide is known to enhance the conversion efficiency of the glass, which

means it can efficiently convert the energy from ionizing radiation into visible light that can be detected and measured. Barium oxide has the following chemical formula: BaO is a chemical and thermal stabilizer that is added to phosphate glass as an intermediate component. In addition,  $^{56}\text{Ba}$  has a high X-ray interaction and reduces hydrolysis in phosphate glass, maintaining BaO in glass is critical (Zaman et al., 2017). The higher concentrations of barium oxide can improve the detection of gamma rays, while lower concentrations may be more suitable for detecting alpha particles that can be improved for the application of radiation shielding material.

**2.4.1.2 Gadolinium Oxide** On a glass network, gadolinium oxide is an essential component material. The chemical formula is  $\text{Gd}_2\text{O}_3$  (Gadolinium oxide), density =  $7.41 \text{ g/cm}^3$ . The high density of Gadolinium oxide is particularly essential for increasing the density of glass, and it has been developed for use in shielding applications. According to a significant portion of the most recent studies, gadolinium oxide is a co-dope with several other rare earths because of its ability to transfer energy. Today, glass scintillators with a high concentration of  $\text{Gd}_2\text{O}_3$  are utilized in a variety of phosphate, germanate, and silicate glass systems because of their comparatively high light yield and fast decay time (Luo et al., 2014).

From the above information,  $\text{Gd}_2\text{O}_3$  can detect high-energy elements and emit (transfer energy) to lower-energy elements,  $\text{Gd}^{3+}$  ions are slow millisecond emission observed 310 nm at originate from forbidden 4f-4f transitions that  $\text{Gd}^{3+}$  are the result of electron loss from 5d and 6s, as seen in figure 2.7 scintillator glass (Kuřcera et al., 2013). Additional  $^{157}\text{Gd}$  and  $^{158}\text{Gd}$  ions are expected to slow neutrons in the future, making them ideal for neutron detection (Kim et al., 2015 and Smith et al., 2015). In addition,  $\text{Gd}_2\text{O}_3$  has effect on glass structure, they can increase density and molar volume with increase in  $\text{Gd}_2\text{O}_3$  concentration. This can be attributed to an increase in the amount of oxygen molecules that do not bridge (NBOs). It is reasonable to suppose that an increase in the amount of gadolinium leads to an accessibility in the structure of the glass network (Al-Hadeethi et al., 2019).

The trivalent gadolinium ion has a suitable energy level scheme for excited state excitation measurements. First, excitation around 310 nm brings the ion to the

$6P_{7/2}$  state. This means that when the ion absorbs light at this wavelength, it gains energy and is promoted to an excited state with a specific energy level.

After the gadolinium ion is in the  $6P_{7/2}$  state, it can absorb another photon of light and undergo multiphoton relaxation, a process where it releases excess energy before emitting light at a lower energy level. The passage mentions that emission can occur from the  $6I_{7/2}$ ,  $6D_{9/2}$ , and  $6G_{7/2}$  levels, which are all lower energy states than the  $6P_{7/2}$  state. These energy levels are referred to as anti-Stokes emission levels, as they emit light at higher energies than the initial excitation.

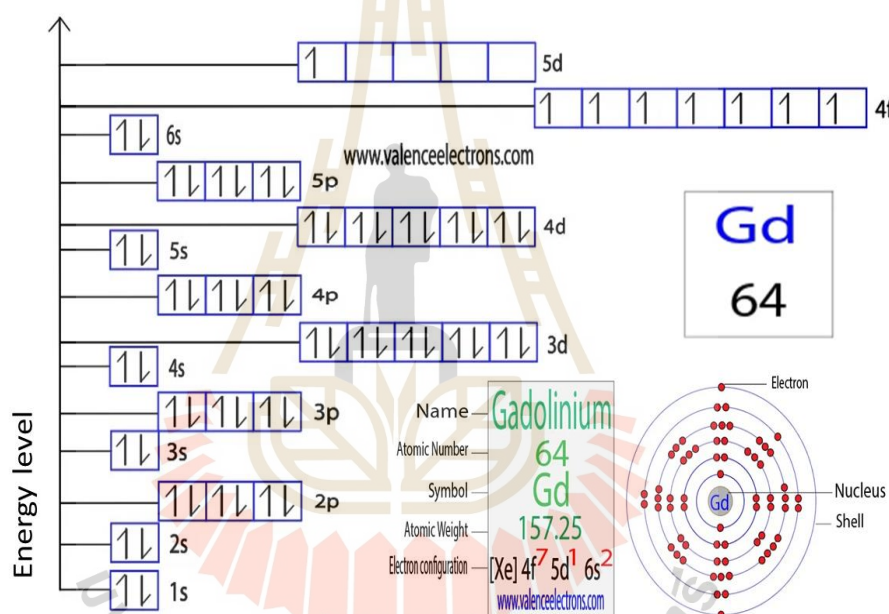


**Figure 2.7** The gadolinium electron configuration and diagram. (<https://valenceelectrons.com/gadolinium-electron-configuration/>)

By detecting the anti-Stokes emissions from one of these three energy levels, researchers can measure the excited state excitation of the gadolinium ion. This technique has many applications, including in scintillation detectors, medical imaging, and nuclear physics research.

Excited state excitation measurements have some advantages compared to two-photon excitation. First, the transition probabilities are higher as the oscillator strength is about 6 orders of magnitude higher. Second, impurities are less of a problem

when the ion under investigation is being excited selectively. Tuning of the first excitation laser to an energy that corresponds to a resonant transition of the  $Gd^{3+}$  ions in figure 2.8  $S_{7/2} \rightarrow {}^6P_{7/2}$  transition gives the two-photon excitation process for the  $Gd^{3+}$  ion a strong enhancement over undesired two-photon excitation processes involving impurities or defects. As a result, the rare-earth doped phosphate glass containing Gd ion could be a potential scintillator candidate.

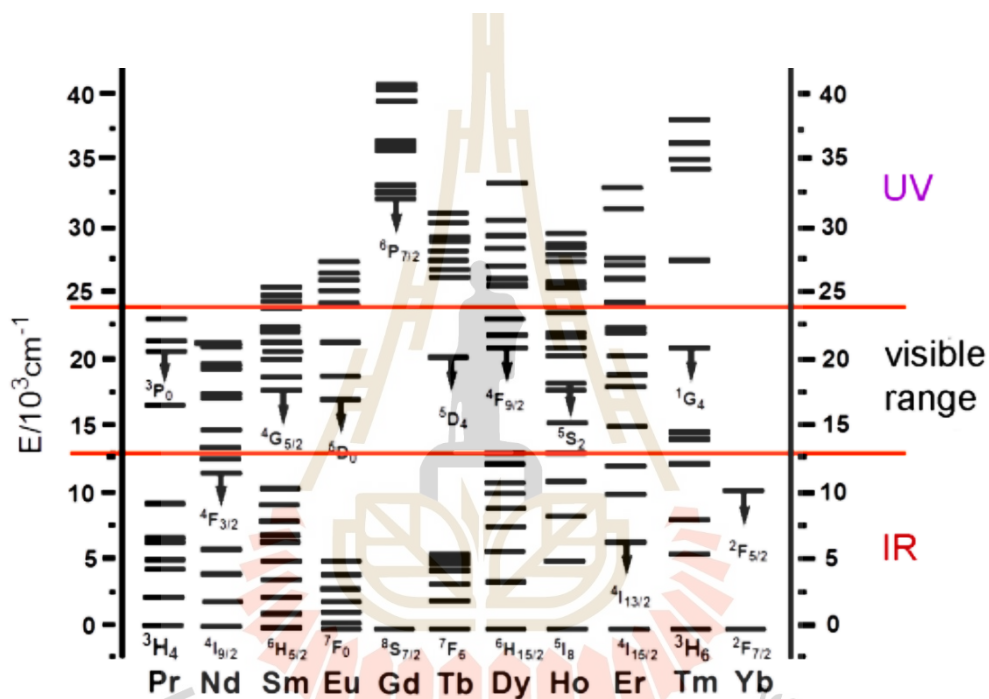


Figure 2.8 The luminescent states are represented on the energy level diagram for  $Ln^{3+}$  ions (except for La, Ce, Pm, and Lu) (Ilichev et al., 2019).

**2.4.1.3 Cerium (III) fluoride** The Cerium from Cerium (III) fluoride ( $CeF_3$ ) doped in optical materials has attracted the curiosity of researchers who have been working on developing a scintillator for years, that one of  $Ce^{3+}$  features is luminescence, can result in radiative  $5d-4f$  transitions in the visible-near ultraviolet region of the electromagnetic spectrum (Weber et al., 1995).

The energy level of an atom can be used to produce an orbital diagram can be explained by following both Pauli's exclusion principle and Hund's principle.



According to Pauli's exclusion principle, the value of all four quantum numbers that describe two different electrons in the same atom cannot be the same. It is necessary to perform the electron configuration of cerium before you can draw the orbital diagram for cerium (Ce). Consequently, as shown in figure 2.9.

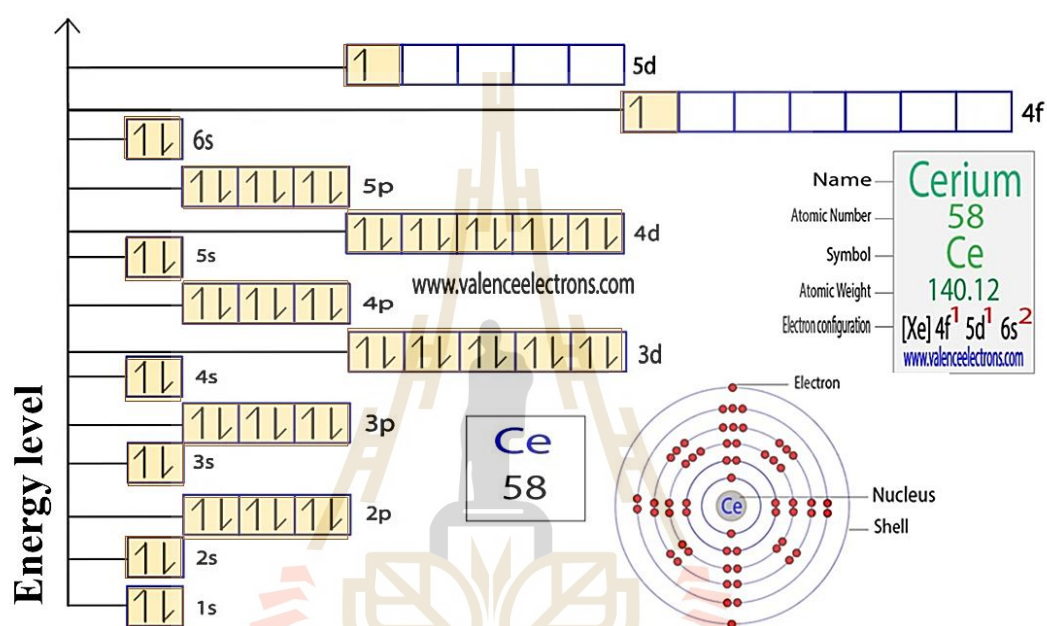


Figure 2.9 The cerium electron configuration and diagram.

(Ref: <https://valenceelectrons.com/cerium-electron-configuration/>)

Cerium also has important qualities that help improve scintillator performance, such as a short decay time (ns) due to the mechanism of  $\text{Ce}^{3+}$  excitation involves the transfer of an electron from the 4f level to the lowest level of 5d, which is then followed by 5d-to-4f fluorescence at a wavelength of 284-300 nm. The spin-orbit interaction divides the free-ion 4f electronic ground state of  $\text{Ce}^{3+}$  into two states  $^2F_{5/2}$  and  $^2F_{7/2}$  separated by 0.3 eV, whereas the excited 5d band is approximately 6.2 eV above the bottom of the 4f band (Lang, 1935). For  $\text{LaF}_3:\text{Ce}$ , the optical excitation of cerium results in fluorescence with a decay time of 20 ns, but for ionizing radiation, there is an early decay component that is 2-10 ns faster (Moses et al., 1994). From the



short distance between the  $5d4f$  and  $5d4f$  states, and a good activator ion (acceptor) in the energy transfer process. (Ronda and Jüstel, 2008).

#### 2.4.2 Glass composition proportions

Phosphate host glass contained numerous materials for enhanced scintillator material performance and shielding as well. For the purpose of this thesis, we aim to synthesize a glass material that can be synthesized by conventional melting and quenching method in low temperature melting at  $1200\text{ }^{\circ}\text{C}$ , will be transparent, and will be able to detect high-energy electromagnetic radiation. The reported scintillation phosphate glasses were synthesized by melt-quenching at  $1200\text{-}1250\text{ }^{\circ}\text{C}$ , followed by annealing at  $500\text{ }^{\circ}\text{C}$  in another furnace and cooling to room temperature, with the formula  $55.5\text{ P}_2\text{O}_5\text{-}(19.5\text{-}24.5)\text{ BaO}\text{-}(10\text{-}20)\text{ BaF}_2\text{-}(2\text{-}8)\text{ Al}_2\text{O}_3\text{-}(1\text{-}7)\text{ Gd}_2\text{O}_3\text{-}1\text{ Ce}_2\text{O}_3$  and the highest intensity of emission are defined in formula  $55.5\text{ P}_2\text{O}_5\text{-}19.5\text{ BaO}\text{-}15\text{ BaF}_2\text{-}6\text{ Al}_2\text{O}_3\text{-}3\text{ Gd}_2\text{O}_3\text{-}1\text{ Ce}_2\text{O}_3$  (Yao et al., 2016). The  $\text{Ce}^{3+}$  doped glass for radiation detection material were prepared followed the formula  $20\text{ Na}_2\text{O}\text{-}10\text{ Gd}_2\text{O}_3\text{-}10\text{ Al}_2\text{O}_3\text{-}(60\text{-}x)\text{ P}_2\text{O}_5\text{-}x\text{ CeF}_3$  (where  $x = 0.00, 0.10, 0.50, 1.50, 2.00$  and  $3.00$  mol%), these glasses were prepared by melt quenching method at  $1200\text{ }^{\circ}\text{C}$  (Wantana et al., 2018).

#### 2.5 Luminescence phenomenon

Luminescence, often known as "cold light," is the spontaneous emission of non-thermal radiation quaveringly or electronically excited species by no means in thermally balanced with its environment". This phenomenon can be caused by chemical processes, electrical energy, subatomic vibrations, and crystal tension. The difference between luminescence and incandescence is that luminescence happens when a substance is heated and creates light. The process of a chemical molecule absorbing light at a specific wavelength, which we call the excitation wavelength, and emitting light at a longer wavelength (lower energy), which we call the emission wavelength, is known as luminescence.

The photoluminescence phenomenon can be classified into two categories: fluorescence and phosphorescence. The Schematic diagram in figure 11 explained the

mechanism of photoluminescence, when you irradiate one atom, some electrons transit from the ground state ( $S_0$ ) to the first excited singlet ( $S_1$ ) or the second excited singlet ( $S_2$ ), which are both unstable. As electrons return to the ground state ( $S_0$ ) from the initial excited singlet state, energy is generated in the form of light in a short period of time ( $10^{-9}$  to  $10^{-6}$  sec), resulting in fluorescence. The electron spin is switched when an intersystem crossing occurs from a singlet excited state ( $S_1$ ) return to an energetically favorable triplet excited state ( $T_1$ ). The parallel spin of each electrons distinguishes triplet excited states, which are metastable. Phosphorescence causes another switch of the electron spin and the emission of a photon, resulting in relaxation. The return to the relaxed singlet ground state ( $S_0$ ) may take a long time ( $10^{-3}$  to  $>100$  sec). (Zhang et al., 2019).

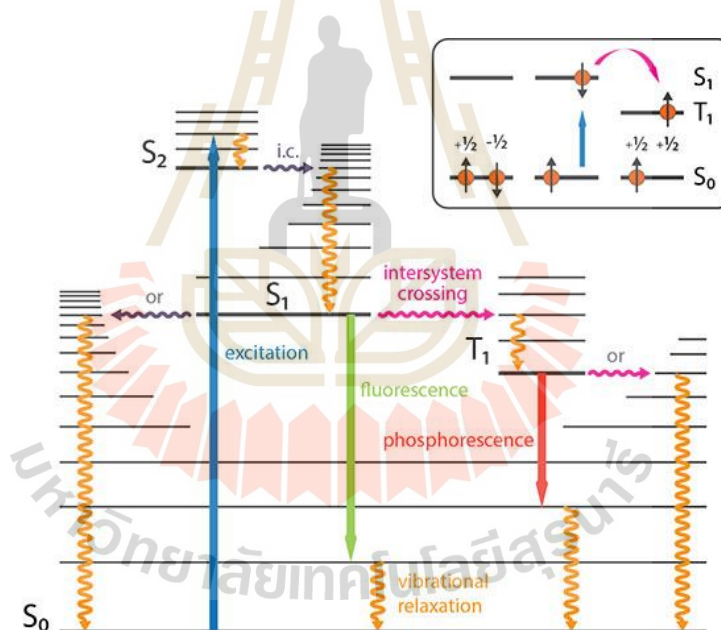


**Figure 2.10** Schematic of Jablonski for the mechanism of Fluorescence vs. Phosphorescence. ©2013 Royal Society of Chemistry.

The luminescence has been the theoretical black ground of the s,p,d,f atomic orbitals. In free atoms, electrons occupy so-called atomic orbitals. Each orbital's energy is determined by the quantum numbers  $n$ ,  $l$ , and  $m_l$ , where  $n$  is the main quantum number, denoted by the numbers 1,2,3...,  $l$  is the orbital quantum number, denoted

by the numbers  $0, 1, 2, \dots, (n-1)$ , and  $m_l$  is the magnetic quantum number, denoted by the numbers  $-l, -l+1, \dots, 0, \dots, l-1, l$  values. This is dictated by quantum law.

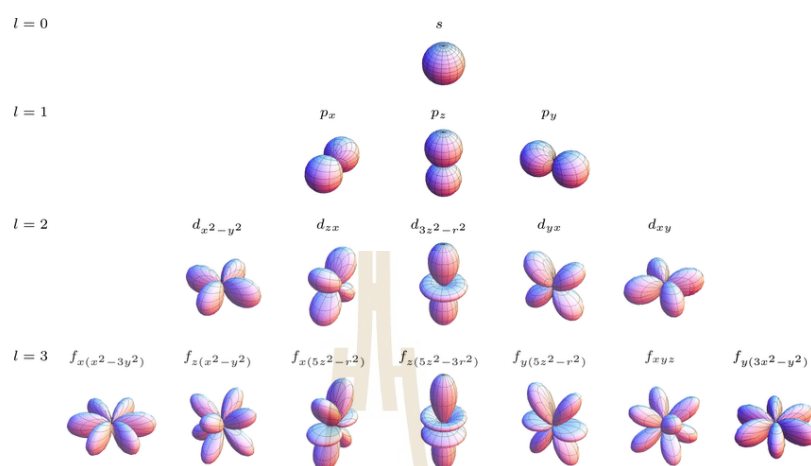


**Figure 2.11** The forms of the angular dependence functions for s, p, d, and f orbitals with  $l = 0, 1, 2, 3$  (Marra, 2016).

The geometry of atomic orbitals in space is defined by the  $l$  quantum number labeled as s, p, d, f for  $l = 0, 1, 2, 3$  as illustrated in figure 2.11, according to the quantum law. According to the  $(2l+1)$  rule, the number of possible orbital orientations is equal to 1 for s-orbitals, 3 for p-orbitals, and 7 for f orbitals. This is notably relevant for explaining absorption and luminescence properties

The luminescence properties, or radiation properties, are characterized by emission under site selective excitation, which is dependent on the luminescence center's local environment symmetry. For d-d or f-f electronic transitions between the free electronic levels of transition metal or rare earth ions in the ligand field spectroscopic state. An ion with a partially filled d- or f-electron shell is accommodated into a crystalline environment with a differential energy between the different orbitals due to the symmetry. The intensities of d-d and f-f absorption can vary over four orders of magnitude of quantum law show in figure 2.11.

After the excitation energy is absorbed, the luminescence of the material will radiate radiation. The luminescence mechanism can be divided into two categories. First, intra-centric excitation happens when a process of excitation is centered around

an isolated center and occurs without ionization of any species in the mineral. That excitation and emission occur due to electronic transition at the center. The second process occurs when high-energy radiation or particles, which have a higher energy than the band gap, excite the band gap. At ionized centers, this process created electrons and holes. Electron transfers in semiconductors with a tiny inter-band separation of impurity ions of the ground substance to the conduction band have resulted in donor (near the conduction band) and acceptors during stimulated by high-energy photons (in the vicinity of the valence band).

**Table 2.2** Main luminescence excitation bands and lines in Cerium, Gadolinium, Europium, and Dysprosium.

Center	Electronic transition	$\lambda_{\text{excitation}}$ (nm)	$\lambda_{\text{luminescence}}$ (nm)
Ce <sup>3+</sup>	4f-5d	280,320-340	360-390
Gd <sup>3+</sup>	<sup>8</sup> S <sub>7/2</sub> - <sup>6</sup> I <sub>7/2</sub>	270	300,312
Eu <sup>2+</sup>	4f <sup>7</sup> -4f <sup>6</sup> 5d	250,310	380-450
Eu <sup>3+</sup>	Charge transfer	220	590,610,650,700
	<sup>7</sup> F <sub>0</sub> - <sup>5</sup> H <sub>3</sub>	325	
	<sup>7</sup> F <sub>0</sub> - <sup>5</sup> D <sub>2</sub>	532	
Dy <sup>3+</sup>	<sup>6</sup> H <sub>15/2</sub> - <sup>6</sup> P <sub>5/2</sub>	351	480,575,670,760

The excitation spectrum revealed that not only for effective luminescence, but also for energy migration inquiry, which is important for luminescence center interpretation, it presented in table 2. Because the bands are more spread out in glasses, the luminescence properties of rare earth ions in glasses are different from the luminescent features of rare earths in crystals. The presence of many rare earth sites in glasses is the primary reason of this inhomogeneous broadening. It is widely considered that network modifiers, like rare-earth ions in oxide glasses, are randomly distributed across the many interstitial locations within the network-former oxygen structure (Oomen and Van Dongen, 1989).

## 2.6 Scintillator detector

Scintillators are materials that have the ability to transform high-energy radiation such as X-rays or gamma rays into near-visible or visible light. Scintillators are used in a variety of applications. They are used as detectors in a variety of applications, including clinical diagnostics, high-energy materials science, and geophysical exploration. Scintillators were originally used in nuclear research. As early as 1944, researchers were successfully detecting ionizing radiation with a phosphor coupled to a photomultiplier tube. Scintillators are available in a variety of forms, including liquid, solid, and gaseous, and they can be either organic or inorganic (glass, single crystal, ceramics). The Photodetectors based on scintillator materials are comprised of a scintillator material and a photodetector, which can be either a photomultiplier tube or a photodiode, depending on the application. The photodetector's job is to transform the light emitted by the scintillator into an electrical signal, which is then processed by the computer. fundamental underlying operating principle Of An electronic light sensor, such as a photomultiplier tube (PMT), photodiode, or silicon photomultiplier, is used in conjunction with a scintillator to produce a scintillation detector or scintillation counter. The photoelectric effect causes PMTs to absorb the light emitted by the scintillator and re-emit it in the form of electrons as a result of the absorption. It is possible to obtain relevant information about the particle that struck the scintillator by analyzing the electrical pulse produced by the following multiplication of those electrons (also known as photo-electron multiplication). As seen in figure 2.12.

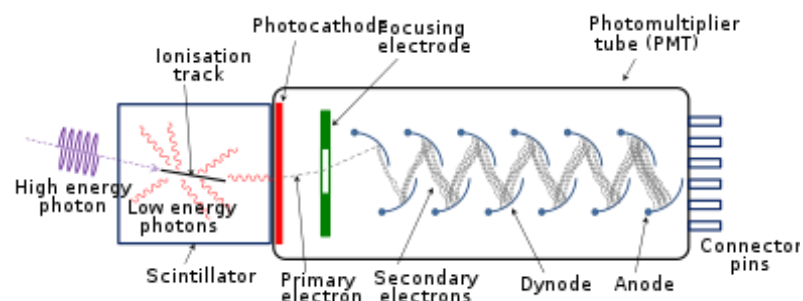


**Figure 2.12** Schematic of A high-energy photon hits a scintillating crystal, releasing low-energy photons that are converted into photoelectrons and multiplied in a photomultiplier.

## 2.7 Detection of ionizing radiation

Energy emitted by matter in the form of rays or high-speed particles is referred to as radiation. Radiation can be classified as either ionizing or non-ionizing, depending on how it interacts with the matter it encounters then show in figure 14. Non-ionizing radiation is a sequence of energy waves made up of oscillating electric and magnetic fields that travel at the speed of light, and it is not harmful to the human body. Ionizing radiation is any electromagnetic or particle radiation that has the ability to produce ion pairs as a result of its contact with matter. Ionizing radiation can be divided into two categories: uncharged particle and charged particle.

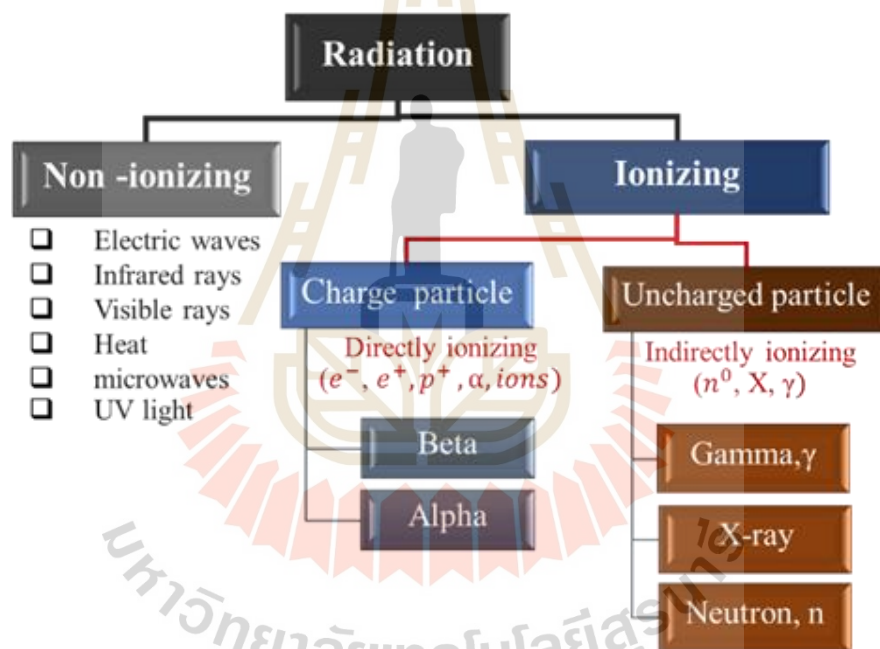


Figure 2.13 Radiation categorization diagram.

Moreover, several studies into radiation shielding studies of glasses have revealed that the shielding capacity of a glass against a specific radiation type and energy varies greatly on the chemical composition of the glass being studied. There is only one thing that matters when it comes to good X-ray shielding, and that is the density that is required. Thus, lead aprons and blankets are the most effective shielding materials for X-ray and gamma-ray radiation shielding applications. In this research, we

will discuss that glass can absorb high-energy radiation such as gamma rays or neutrons. Currently, researchers utilize gamma shielding materials that have a high density and a high Z value (Z is the atomic number), while neutron shielding materials have a low atomic number. These low-Z elements have a strong potential to slow neutrons by collisions (moderation); these elements are described in Table 2.3 (Issard, 2015).

**Table 2.3** Example of neutron capture cross sections by an isotope (thermal neutrons).

Isotopes	Mass nb	Cross section capture	Natural% isotope
$^1\text{H}$	1	0, 332	100
$^3\text{Li}$	6	945	7,4
$^5\text{B}$	10	4107	19
	11	73	81
$^{48}\text{Cd}$	113	20800	12, 34
$^{62}\text{Sm}$	149	40800	13, 85
$^{63}\text{Eu}$	151	7800	47, 8
	153	440	52, 2
$^{64}\text{Gd}$	155	56200	14, 78
	157	242000	15, 71
$^{72}\text{Hf}$	174	1500	0, 18
	177	380	18, 39

## 2.8 Materials characterization

Material characterization is an important aspect of research. That component might be used to prove and analyze the research's goal or to link back to the correct way to discuss problems. We will only write about techniques that we have used or are interested in using in the future in this section.



### 2.8.1 Density and molar volume

The density ( $\rho$ ) of the examined samples was determined using the standard Archimedes method at room temperature. The sample density was determined using the following equation (1) as an average of triplicate measurements:

$$\rho_{sample} = \left( \frac{W_{air}}{W_{air} - W_{liq}} \right) \times \rho_{liq} \quad (1)$$

Where  $W_{air}$  is weight of sample in air,  $W_{liq}$  is weight of displaced liquid, and  $\rho_{liq}$  is density of liquid

The molar volume ( $V_m$ ) is the volume occupied by one mole of a chemical element or a chemical compound at standard temperature and pressure (STP). It is determined by calculating the molar weight ( $MW$ ) by the mass density ( $\rho$ ). can be calculated using the equation (2).

$$V_M = \frac{MW}{\rho} \quad (2)$$

### 2.8.2 Refractive index

The ratio of the speed of light in a vacuum to that in a second medium of larger density is used to compute the refractive index, commonly known as the Index of Refraction. The refractive index variable is most commonly denoted by the letter  $n$  or  $n'$  in mathematical equations and descriptive writings then shown in equation (3).

$$n' = \frac{c}{v} \quad (3)$$

Where,  $c$  is velocity of light in empty space and  $v$  is the velocity of light in a matter.

### 2.8.3 Scintillator decay times

A scintillator's decay time is defined as the time required for the intensity of the light pulse to return to  $1/e$  of its greatest value. The majority of scintillators have several decay times, and the effective average decay time is frequently mentioned. The decay time is critical for applications requiring rapid counting and/or timing. In this work, the scintillation data were measured and analyzed, as shown in figure 2.14, and the exponential decay formula was used to determine the rate of decline with time, as demonstrated in equation (4).

$$I(t) = A_1 e^{\frac{-t}{\tau_1}} + A_2 e^{\frac{-t}{\tau_2}} + y_0 \quad (4)$$

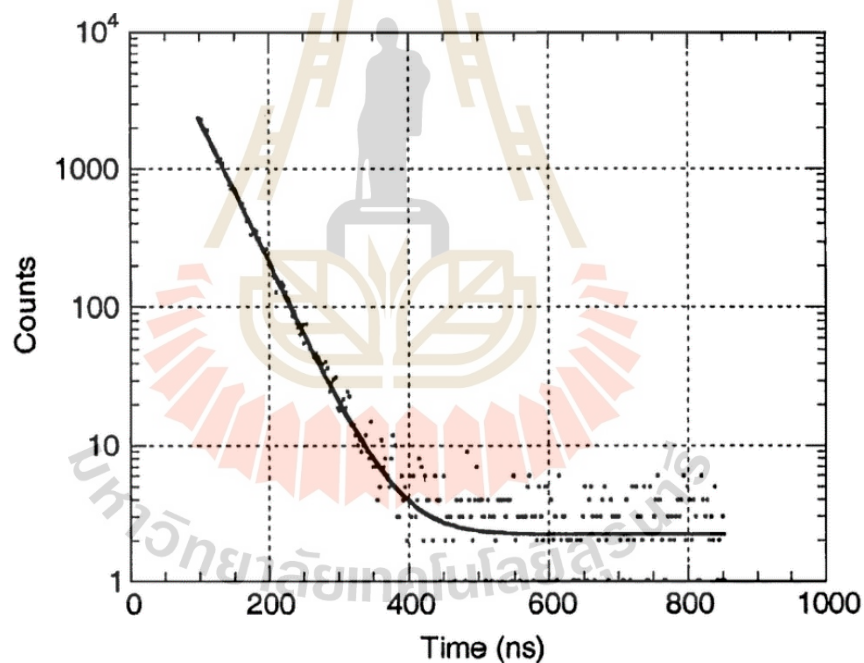
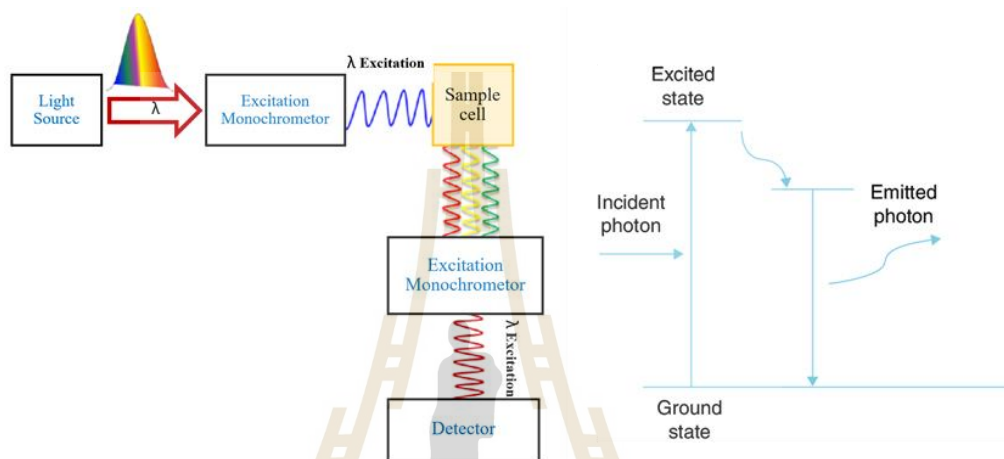


Figure 2.14 Luminescence decay curve of glasses.

### 2.8.4 Photoluminescence (PL)

The optical properties of semiconductors and other materials are commonly characterized using photoluminescence. The principle is simple: a laser with an energy greater than the bandgap excites electrons from the valence to the conduction band of the material. The schematic of photoluminescence

spectroscopy measurement system and the electronic levels and transitions is shown in Figure 16. The photon energy of the emitted photon is a direct measure of the energy difference between the involved orbitals or bands. In this way, the direct band gap of semiconductors can be determined, or the HOMO–LUMO gap in molecules. In semiconductors, it is also common that point defects yield states in the band gap so that photoluminescence is observed at photon energies below the band gap.



**Figure 2.15** schematic of photoluminescence spectroscopy measurement system and the electronic levels and transitions.

From information of photoluminescence spectra can be calculated the chromaticity color coordinates ( $x$ ,  $y$ ), correlated color temperature CCT color purity (CP), and color rendering index (CRI), respectively were estimated using CIE Color Calculator software and the following fundamental relations: CCT was calculated from color coordinates ( $x$ ,  $y$ ) using the McCamy method (Damodaraiah and Ratnakaram, 2019).

$$\text{CCT} = -449n^3 + 352n^2 - 6823.3n + 5520.33 \quad (5)$$

Where  $n = (x - x_e)/(y - y_e)$  is the inverse slope line with  $x_e = 0.3320$  and  $y_e = 0.01858$ . And the color purity was determined using relation:

$$\text{Color purity} = \sqrt{\frac{(x-x_i)^2+(y-y_i)^2}{(x_d-x_i)^2+(y_d-y_i)^2}} \times 100\% \quad (6)$$

where  $(x_i, y_i)$  and  $(x_d, y_d)$  represent the chromaticity coordinates of the light source under test, chromaticity coordinates of the white illuminant (0.333, 0.333), and dominant wavelength, respectively (Zagrai et al., 2021).

### 2.8.5 UV-Vis

The absorbance or transmittance of light is measured using the UV-visible spectroscopy technique, which is a quick analytical procedure. However, despite the fact that the UV wavelength extends from 100–380 nm and the visible component reaches up to 800 nm, the majority of spectrophotometers have a working wavelength range between 200–1100 nm.

The useful range for UV-vis spectroscopy is 200–800 nm; wavelengths beyond 800 nm are referred to as infrared, and wavelengths below 200 nm are known as vacuum UV. When it comes to color, the ability of matter to absorb and emit light is what determines it, and the human eye is capable of distinguishing between up to ten million different shades (Rocha et al., 2018).

UV-visible spectroscopy is based on the electronic transitions of organic molecules that absorb light and excite electrons from a lower energy orbital (highest occupied molecular orbital—HOMO) to a higher energy unoccupied orbital (lowest unoccupied molecular orbital—LUMO) in a higher energy unoccupied orbital LUMO. Figure 2.16 (a) shows that the energy of the light wavelength absorbed must be equal to  $\Delta E$ , which is the HOMO-LUMO energy gap.

The length of the light wavelength increases in proportion to the size of the conjugated  $\pi$  system. So, because energy gap between the lower energy molecular orbital and the higher energy molecular orbital is narrower in conjugated  $\pi$ - $\pi$  systems than in isolated double bonds, longer wavelengths are absorbed in these systems. The length of the light wavelength increases in proportion to the size of the conjugated  $\pi$  system. In addition, figure 17(b) illustrates the process of the atomic orbitals and the energy gap required to excite the electron energy state,

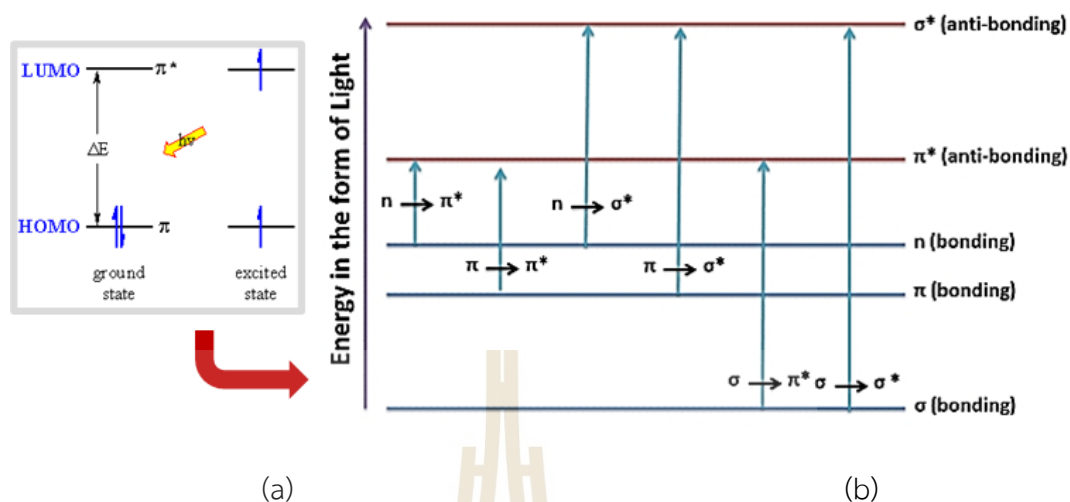


**Figure 2.16** (a) and (b) The atomic orbitals and the energy gap required to excite the electron energy state are discussed in detail.

$\sigma$ -bond (stable electrons) absorbs light at lower ultraviolet wavelengths,  $\pi$ -bond (higher energy levels for the ground state) absorbs energy at ultraviolet and visible light wavelengths, and  $n$ -electrons (non-bonding electrons) can be excited by ultraviolet and visible light.

The Beer-Lambert rule states that the absorbance of light,  $A$ , is proportional to the route length through the sample,  $b$ , the concentration,  $C$ , and a molar absorptivity,  $\epsilon$ , that is characteristic of each chemical. Is it possible to write in a way that corresponds to Eq. (7) when the light intensity, ( $I$ ) is measured in relation to an outside reference ( $I_0$ ).

$$A = \log \frac{I_0}{I} = \epsilon \cdot b \cdot C \quad (7)$$

### 2.8.6 Optical band gap

The absorption spectra have been used to estimate the optical energy band gap for direct and indirect transitions from Tauc's relation plotting. The band gap of glass can calculate via UV-vis absorption spectrum. The absorption coefficient ( $\alpha$ ) is given by

$$\alpha = 2.303 \frac{A}{d} \quad (8)$$

Where  $A$  is the absorbance and  $d$  is the sample thickness

Generally, the absorption coefficient ( $\alpha$ ) is related to photon energy (incident photon energy:  $h\nu$ ) by the known equation as:

$$\alpha = \beta/h\nu(h\nu - E_g)^r \quad (9)$$

$$\text{Or } (\alpha h\nu)^{1/r} = \beta(h\nu - E_g) \quad (10)$$

Where  $\beta$  is a constant called the band tailing parameter.

$E_g$  is the energy of the optical band gap

$r$  is the power factor of transition mode.

The reflectance spectrum of  $\text{TiO}_2$  (an indirect band gap semiconductor) converted according to Eq. 10 and plotted against photon energy is shown in figure 2.17. Semiconductor materials are characterized by a steep, linear increase in light absorption with increasing energy. The band gap energy is estimated using the x-axis intersection point of the linear fit of the Tauc plot.

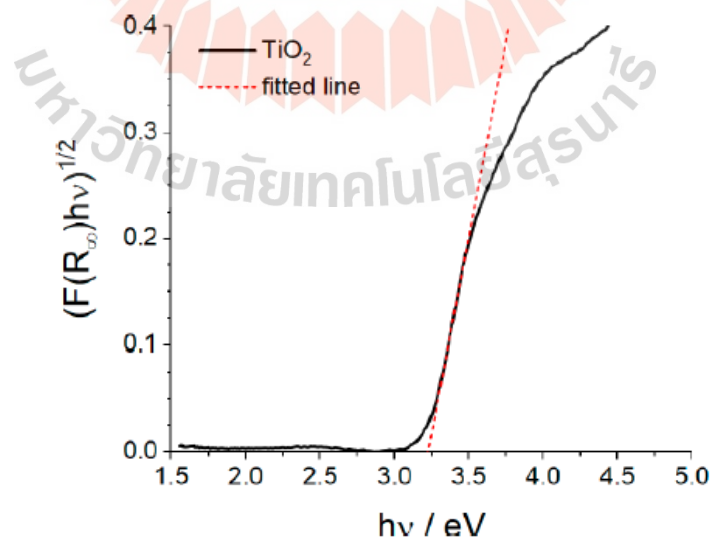


**Figure 2.17** The Tauc plot is used to calculate the band gap energy ( $E_g$ ). The plot's linear portion is extrapolated to the x-axis.

Depending on whether the substance is crystalline or amorphous. For direct electronic transition in the K space, incident electronic transition, direct forbidden transition, and indirect forbidden transition, respectively,  $r$  can take the values  $1/2$ ,  $2$ ,  $3/2$ , and  $3$ .

In accordance with Tauc's relationship. When plotting  $(\alpha h\nu)^{1/r}$  relative photon energy ( $h\nu$ ), a straight line appears in a specific location. The ( $h\nu$ ) axis will be intercepted by the extrapolation of this straight line, yielding the value of the indirect optical energy ( $E_g$ ). The Tauc and Devis-Mott relationship is defined by the equation  $(\alpha h\nu)^n = \beta(h\nu - E_g)$ . For direct band gap materials  $n = 1$  and indirect band gap materials  $n = 1/2$ , this relationship is used to explore the optical band gap energy of nanoparticles using UV-VIS absorption spectroscopy, the plot's linear portion is extrapolated to the x-axis then show in figure 2.17.

### 2.8.7 X-Ray Diffraction (XRD)

In materials science, X-ray diffraction analysis (XRD) is a technique used to determine the crystallographic structure of a material. XRD is a technique that involves irradiating a material with incident X-rays and then measuring the intensities and scattering angles of the X-rays that escape. This is referred to as elastic scattering, and the electron is referred to as the scatterer. A periodic array of scatterers results in a periodic array of spherical waves. While these waves cancel each other out in the majority of directions due to destructive interference, they add constructively in a few select directions, as indicated by Bragg's law that show in figure 2.18 and equation (11):

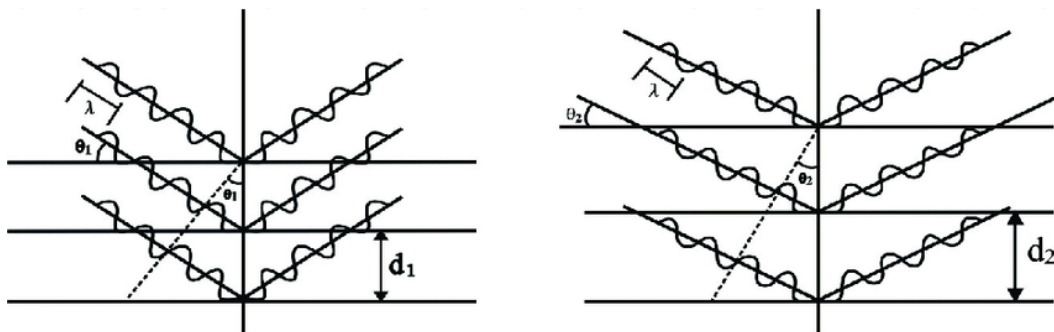


Figure 2.18 Diffraction: Bragg's Law (Kubala-Kuku's et al., 2013).

$$2d\sin\theta = n\lambda \quad (11)$$



Where  $d$  is the distance between diffracting planes,  $\theta$  is the incidence angle,  $n$  is an integer, and  $\lambda$  is the wavelength of the reflected beam. The precise directions show as reflections, which are little spots on the diffraction pattern that appear on the surface of the water. Thus, X-ray diffraction patterns are produced by electromagnetic waves impinging on a regular array of scatterers, resulting in the formation of a pattern.

### 2.8.8 Scanning electron microscopy (SEM) and Energy Dispersive X-Ray Spectroscopy (EDX)

When it comes to materials analysis, energy dispersive X-ray spectroscopy (EDX) is a technique that is used to characterize them analytically or chemically. When used in conjunction with an electron microscope, such as transmission electron microscopy (TEM) or scanning electron microscope (SEM), EDX systems are typically attached (SEM).

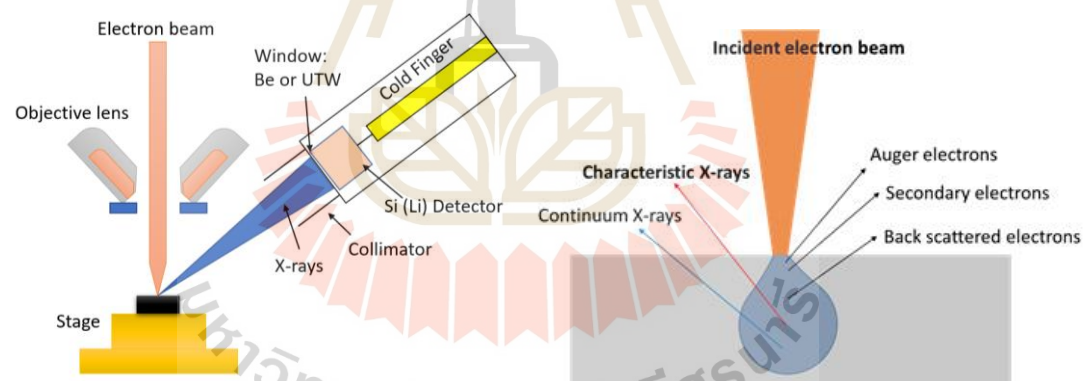


**Figure 2.19** (a) Schematic of the energy dispersive x-ray spectroscopy (EDX) principle in a scanning electron microscope (SEM) and (b) Types of beam-specimen signals (<https://wiki.aalto.fi/display/SSC/Energy-dispersive+X-ray+spectroscopy>).

The emission of distinctive X-rays from a specimen is the basis for EDX show in figure 2.19. A concentrated beam of high-energy charged particles (electrons or protons) is directed into the sample under investigation. When an electron from a higher binding energy electron level falls into the core hole, an X-ray with the energy

of the difference between the binding energies of the electron levels is released as a result of the collision.

The results of the EDX study are a spectrum that indicates the peaks that are associated to the elemental composition of the material under investigation. Additionally, using this characterization method, it is possible to produce an elemental mapping of a given sample then show in figure 2.20(b).

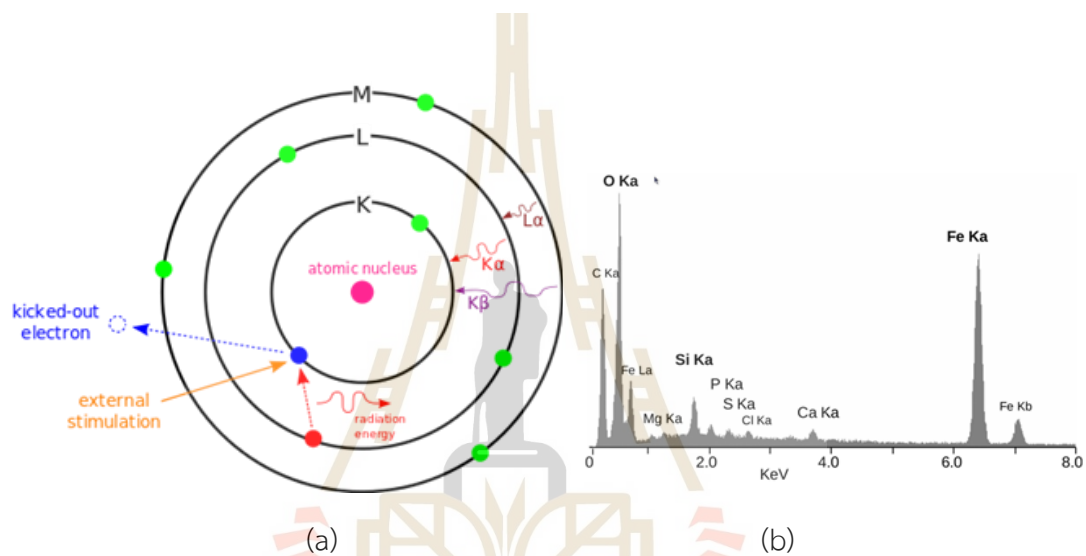


**Figure 2.20** (a) Schematic diagram of the characteristic X-ray generation and (b) EDX elemental analysis of a clean PTFE surface.

### 2.8.9 X-ray absorption spectroscopy (XAS)

XAS, or X-ray Absorption Spectroscopy, is a widely used technique for studying both the local structure of atoms and their electronic states. In general, an X-ray excites a core electron within an atom, which can then be promoted to an unoccupied level or ejected from the atom. Both of these processes will result in the formation of a core hole. Because the excited electrons are often from the 1s or 2p shells, the energy are in the thousands of electron volt range. As a result, XAS requires extremely high-energy X-ray excitation, which is available at synchrotron facilities. The energy of X-rays is approximately 104 eV (where "soft x-rays" are between 100 eV and 3 keV and "hard x-rays" are greater than 3 keV), which corresponds to wavelengths of

approximately 1 Angstrom. Due to the fact that this wavelength is on the same order of magnitude as the separation between atoms in molecular structures, XAS is an effective tool for deducing the local structure of atoms. XAS is particularly advantageous because it is a non-destructive method for directly inspecting samples. Structures can be determined from heterogeneous and amorphous substances.

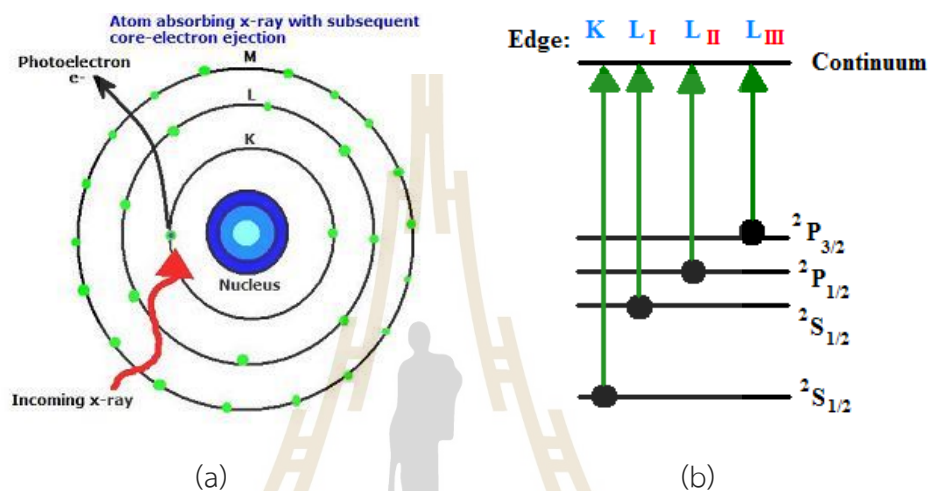


**Figure 2.21** The diagram of an atom absorbing an x-ray and ejecting a core electron into the continuum

When an X-ray interacts with an atom, one of the core electrons is either stimulated to a higher energy unoccupied state (a transition investigated by XAS) or to an unbound state known as the continuum. The ejection of electrons from an atom of a solid material is essentially the photoelectric effect, which is examined using X-ray Photoelectron Spectroscopy. When computing the wave vector ( $k$ ) of a photoelectron in figure 2.21(a), the subset of XAS utilized is determined by the wave vector of the electron (EXAFS, NEXAFS, etc.). After analyzing the de Broglie equation, the photoelectron's kinetic energy  $E_k$  and threshold energy  $E_0$  (amount of energy required to promote the electron into the continuum) can be discussed in equation (12):

$$k = \frac{h}{p} \quad (12)$$

Where  $p$  is the momentum of the electron,  $\lambda$  is the wavelength, and  $h$  is Planck's constant. The electron's wave vector ( $k$ ) is denoted by  $k$  and can be defined as equation (13).

$$k = \frac{2\pi}{\lambda} = \frac{2\pi p}{h} \quad (13)$$

The incident X-ray energy,  $E$ , and the threshold energy,  $E_0$ , are discussed in equation (14). And where  $E_B$  denotes the core electron's binding energy to the atom and  $E_B + \Phi$  denotes the ionization energy the described in equation (14).

$$E_k = E - E_0 = h\nu - E_0 \quad (14)$$

can be rewritten as 
$$E_k = h\nu - E_B - \Phi \quad (15)$$

And so, the photoelectron's wave vector ( $k$ ) can be expressed as equation (16).

$$k = \sqrt{\left(\frac{2\pi}{h}\right)^2 2m(h\nu - E_0)} \quad (16)$$

The diagram in figure xx(a) depicts an atom absorbing an x-ray and ejecting a core electron into the continuum as a result. Nota bene, the level K denotes the  $n=1$  level, the level L denotes the  $n=2$  level, and the level M denotes the  $n=3$  level. A sample's resulting X-ray photon energy spectrum will show these edges at X-ray photon energies that are equal to or greater than the ionization potentials of the bound electrons in its component atoms. Figure 22(a) depicts the K-edge and three L-edges of a typical X-ray absorption spectrum, with the K-edge being the most prominent. This nomenclature identifies the core orbital from which the electron came into being. As depicted in figure 2.21(b), The K-edge is a result of the  $1s-3p$  transition,

whereas the 2s–5p (LI), 2p<sub>1/2</sub>–5d<sub>3/2</sub> (LII), and 2p<sub>3/2</sub>–5d<sub>5/2</sub> (LIII) transitions are the result of the 2s–5p (LII), 2p<sub>3/2</sub>–5d<sub>5/2</sub> (LIII) transitions, respectively. At synchrotrons, it is possible to see a characteristic edge citation of elements due to the presence of certain elements.

### 2.8.10 Stopping Power and Range of Ions in Matter

SRIM is a software package that uses a full quantum mechanical treatment of ion-atom collisions to calculate the stopping and range of ions in matter. SRIM is used in research to plan ion implantation processes to fit the desired ion depth profile and target damage. SRIM calculates the stopping and range of ions (10 eV – 2 GeV/amu) into matter and simulates an ion implantation using a full quantum mechanical treatment of ion-atom collisions. In terms of the stopping power. SRIM simulates the ion implantation process starting from few input parameters about the beam and the target and makes Monte carlo calculations the ion trajectories which can be displayed singularly with details and synthesized into distribution graphs and synthetic statistic quantities. The stopping power is the rate of loss of energy per unit length (-dE/dx). It depends on the speed and charge of both the fallen particles and the target material. The stopping power equation describes the rate at which an energetic charged particle loses energy as it passes through a material. The equation is given by (17).

$$\frac{-dE}{dx} = \frac{4\pi Z_1^2 e^4 N}{mv^2} \quad (17)$$

where dE/dx is the stopping power, N is the number density of atoms in the material, Z is the atomic number of the material, m is the electron mass, and v is the velocity of the particle.

The first term on the right-hand side of the equation describes the effect of the Coulomb interaction between the charged particle and the atomic electrons in the material. The stopping power equation is important in many fields of physics and engineering, such as radiation protection, nuclear physics, and ion implantation. It is used to calculate the energy loss of charged particles as they pass through matter,

which is essential for understanding and predicting the behaviour of these particles in various applications.

In addition, Monte Carlo calculations are a computational technique used to simulate complex systems that involve random variables. In the case of SRIM, Monte Carlo calculations are used to simulate the trajectories of ions as they pass through a target material during ion implantation. SRIM uses a random number generator to simulate the interactions between ions and atoms in the target material. The program calculates the probability of each possible interaction based on a set of physical models and cross-section data, and then selects a random outcome for each interaction. By repeating this process many times, SRIM generates a set of ion trajectories that represent the statistical behavior of ions passing through the target material. These simulated trajectories provide valuable insights into the effects of ion implantation, such as the distribution of ion energies and the depth at which ions come to rest in the target material. By analyzing these trajectories, researchers can optimize the parameters of ion implantation processes to achieve specific goals, such as creating a certain ion depth profile or inducing a desired amount of target damage.



Figure 2.22 SRIM window of input parameters for stopping calculation.



### 2.8.11 The Compton coincidence technique (CCT)

Compton scattering is characterized by the "particle picture," in which the collision process's kinematics can be estimated classically while adhering to relativistic forms of energy and momentum conservation. Assuming high-energy transfer occurs, the energy of an atomic electron previous to scattering can be discarded.

$$(E_{\gamma} - E_{\gamma'}) \gg E_B \quad (18)$$

Where  $E_B$  is the binding energy). This is the Compton scattering of an electron in a quasi-free state. The electron can be considered to be at rest in this situation, and  $E_{\gamma'}$  is just a function of  $E_{\gamma}$  and the scattering angle.

$$E = E_{\gamma} - E_{\gamma'} \quad (19)$$

The energy of scattered photon ( $E_{\gamma'}$ ) can be calculated by equation (20). The figure 19(a) shows the schematic of experiment set up.

$$E_{\gamma'} = \frac{E_{\gamma}}{1 + \frac{(1 - \cos\theta)E_{\gamma}}{mc^2}} \quad (20)$$

Where  $E_{\gamma'}$  is the scattered gamma ray energy,  $E_{\gamma}$  is the incident gamma ray energy.  $\theta$  is the known angle of interaction between the incident photon and scattered photon and  $mc^2$  is the rest mass of an electron (511keV)

Figure 2.23(a) depicts both the beginning and end states, with the photon scattering at an angle ( $\theta$ ) of and the electron recoiling at an angle of ( $\phi$ ). The photons were the result of nuclear decay, and their great energy rendered it irrelevant that the electrons were bonded in atoms. The formula for the scattered photon's wavelength as a function of angle. and Each of the three types of gamma ray interactions is determined by the initial gamma ray energy and the atomic number, Z, of the substance in which the interaction occurs. Figure 2.23(b) depicts the area where each



type is most prominent (b). For materials with a low Z and gamma energies below a few hundred keV, the photoelectric effect is the dominant process. Pair formation becomes considerable above 5 MeV gamma energy. Thus, the Compton Effect is most pronounced at energies between 1 and 2 MeV.

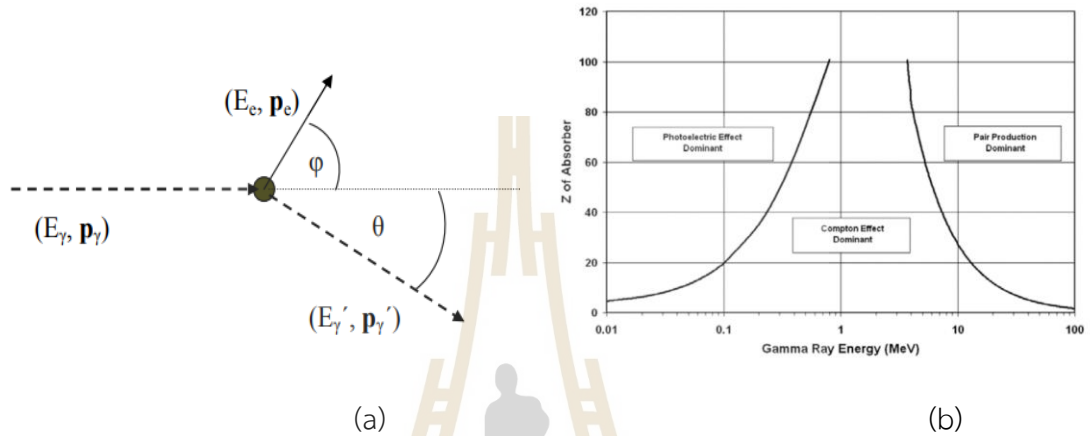


**Figure 2.23** (a) The schematic of kinematics of Compton Scattering (Limkitjaroenporn et al., 2010) and (b) The strength of each of the three forms of gamma ray interactions relies on initial gamma ray energy and Z of the material (Parks, 2015).

The total probability for interaction of total linear attenuation is composed of photoelectric ( $\tau$ ), Compton ( $\sigma$ ) and pair production ( $K$ ). Total linear attenuation may be determined using the equation (21).

$$\mu(\text{m}^{-1}) = \tau + \sigma + K \quad (21)$$

When the photoelectric can be described by eq. (22)

$$\tau = \frac{\text{probability for photoelectric effect to occur}}{\text{Distance traveled by photon}} \quad (22)$$

The pair product coefficient is a complicated function of the incident gamma ray energy ( $E_\gamma$ ) and atomic number (Z).

$$\sigma(\text{m}^{-1}) = Z_{\text{eff}}(E_\gamma) \quad (23)$$

The probability that Compton scattering is a complicate function of photon energy.

$$K(\text{m}^{-1}) = Z_{\text{eff}}^2(E_{\gamma}, Z) \quad (24)$$

In this experiment we measure mass attenuation coefficient for experiment ( $\mu_{mE}$ ) in unit of  $\text{cm}^2/\text{g}$  and compared with mass attenuation coefficient ( $\mu_{mt}$ ) in theoretical by

$$\mu_{mE} = \frac{\text{LN}\left(\frac{I_0}{I}\right)}{\rho x} \quad (25)$$

Where  $\rho$  is the density of material ( $\text{g}/\text{cm}^3$ ),  $I^0$  and  $I$  are the incident and transmitted intensities and  $t$  is the thickness of absorber (cm). Theoretical values of the mass attenuation coefficients of mixture or compound have been calculated by WinXCom, based on the rule of mixture (Gerward et al., 2004).

$$\mu_{mt} = \sum_i W_i (\mu_m)_i \quad (26)$$

Where  $w_i$  is weight fraction of element in an alloy,  $(\mu_m)_i$  is mass attenuation coefficient for individual element in alloy. The value of mass attenuation coefficients can be used to determine the total atomic cross-section ( $\sigma_{t,a}$ ) by the following relation (Limkitjaroenporn et al., 2011).

$$\sigma_{t,el} = \frac{1}{N_a} \sum \left( \frac{\mu_{mi} F A}{Z} \right) \quad (27)$$

Where  $N_A$  is Avogadro's number,  $A_i$  is atomic weight of constituent element of alloy. The total electronic cross-section ( $\sigma_{t,el}$ ) for the element is also expressed by the following formula (Limkitjaroenporn et al., 2011)

$$\sigma_{t,a} = \frac{\mu_{mt}}{N_a \sum \frac{W_i}{A_i}} \quad (28)$$

Where  $f_i$  is the number of atoms of element  $i$  relative to the total number of atoms of all elements in alloy,  $Z_i$  is the atomic number of the element in glass. Total atomic cross-section and total electronic cross-section are related to effective atomic number ( $Z_{\text{eff}}$ ) of the compound through the formula (Limkitjaroenporn et al., 2011)

$$Z_{\text{eff}} = \frac{\sigma_{t,a}}{\sigma_{t,el}} \quad (29)$$

The electron density can be defined as the number of electrons per unit mass, and it can be mathematically written as follows (Kaewkhao et al., 2008).

$$N_{\text{el}} = \mu_m / \sigma_{t,el} \quad (30)$$

Compton Effect Learning Objectives: To learn how the photopeak, Compton Knee, X-ray Production, and positron annihilation are formed, Compton Effect basics (Laws of Conservation of Energy and Momentum, Relativistic Mechanics) and how a gamma ray interacts with a scintillator and causes light; how a photomultiplier tube produces a voltage pulse.

## CHAPTER III

### RESEARCH PROCEDURE

In this section, we will describe the procedure of synthesis a phosphate glass sample and how to fabricate and measure a phosphate glass sample so that its physical properties, optical properties, and chemical properties may be investigated.

#### 3.1 Preparation of glass samples

The phosphate Glasses were fabricated in collaboration with Associate Professor Dr. Jakrapong Kaewkhao of the Physics program at Nakhon Pathom Rajabhat University's Faculty of Science. The fabrication method of glass that is carried out in accordance with the procedure given below.

##### 3.1.1 Raw materials

The raw materials for synthesizing phosphate glass typically include a phosphate source such as Ammonium Phosphate Dibasic ((NH<sub>4</sub>)<sub>2</sub>HPO<sub>4</sub>), along with metal oxides such as Barium carbonate (BaCO<sub>3</sub>), Lithium carbonate (Li<sub>2</sub>CO<sub>3</sub>), Gadolinium oxide (Gd<sub>2</sub>O<sub>3</sub>), and Cerium (III) fluoride (CeF<sub>3</sub>). These materials are typically weighed and mixed together in the desired proportions and then placed in a furnace. The commercial chemical precursors listed below were employed in this study:

1. Ammonium Phosphate Dibasic ((NH<sub>4</sub>)<sub>2</sub>HPO<sub>4</sub>), Sigma-Aldrich, 98%
2. Barium carbonate (BaCO<sub>3</sub>), 99.999% trace metals basis, Sigma-Aldrich
3. Lithium carbonate (Li<sub>2</sub>CO<sub>3</sub>), 99.99% trace metals basis, Sigma-Aldrich
4. Gadolinium oxide (Gd<sub>2</sub>O<sub>3</sub>) powder, 99.9% trace metals basis, Sigma-Aldrich
5. Cerium (III) fluoride (CeF<sub>3</sub>) anhydrous, powder, 99.99% trace metals basis, Sigma-Aldrich

### 3.1.2 Phosphate glass synthesis

The conventional melt quenching method is a common technique used for synthesizing glass materials. It involves melting the raw materials together in a high-temperature furnace or crucible, typically at temperatures above the melting point of the highest melting component. The mixture is then quickly cooled or quenched, often by pouring it onto a metal plate or into a mold, to rapidly solidify the material and prevent crystallization. During the cooling process, the glass undergoes a structural transformation from a liquid to a solid state, resulting in the formation of a non-crystalline, amorphous material. The quenching rate is an important parameter in determining the final properties of the glass, as it can affect the degree of structural relaxation and the distribution of structural defects in the material.

The conventional melt quenching method can be used for synthesizing phosphate glasses, and it typically involves melting the raw materials together at high temperatures, typically in the range of 1200-1500 °C. However, in the case of phosphate glasses, it is possible to melt the raw materials at lower temperatures, typically around 1200 °C, due to the low melting temperatures of the components

After synthesis, the glass material can be further processed by various techniques such as cutting, polishing, and annealing, to achieve the desired shape, surface quality, and properties. The resulting glass material can then be characterized using a range of analytical techniques to assess its physical, chemical, and optical properties.

## 3.2 Finding host glass

### 3.2.1 Various concentration of Gadolinium Oxide

First, we are determining the percentage of glass that will melt at a low temperature of 1200 °C by using gadolinium oxide in a variety of 6 concentrations. In most cases, the components in the formula for glass are referred to as network formers, network modifiers, and intermediates. We generated the first composition of glass using the formula in which the ratio of network formers, network modifiers, and intermediates is 80-x: 20: x mol percent, where the network glass is P<sub>2</sub>O<sub>5</sub>, the network

modifiers are  $\text{Li}_2\text{O}$  and  $\text{BaO}$ , and the intermediate is  $\text{Gd}_2\text{O}_3$ , respectively. Then, we begin with  $(80-x) \text{P}_2\text{O}_5: 10\text{Li}_2\text{O}: 10\text{BaO}: x\text{Gd}_2\text{O}_3$ , where  $x = 0, 10, 12, 14, 16, 18, 20$  mol%.

The series of sample host glasses are highly transparent and melt completely for 0-18 mol % of  $\text{Gd}_2\text{O}_3$ , except for 20 mol %, where some components do not melt, demonstrating the powder inside the bulk glass. From the result of  $(80-x) \text{P}_2\text{O}_5: 10\text{Li}_2\text{O}: 10\text{BaO}: x\text{Gd}_2\text{O}_3$ , where  $x = 0, 10, 12, 14, 16, 18, 20$  mol%. We choose the best condition of  $\text{Gd}_2\text{O}_3$  at 18 mol% for optimized with  $\text{CeF}_3$  followed the phosphate glass formula.  $\text{Li}_2\text{CO}_3$ ,  $\text{BaCO}_3$ ,  $\text{NH}_4\text{H}_2\text{PO}_4$ ,  $\text{Gd}_2\text{O}_3$ , and  $\text{CeF}_3$  are the chemical precursors used to make the glass sample. For the set amount of expected sample mass. The masses of precursor are obtained by multiplying the gravimetric factor. Gravimetry or gravimetric analysis is a quantitative analytical technique based on the mass measurement of a pure chemical substance to which the analyte is chemically connected. The Gravimetric Factor (GF) is used to create glass samples from precursors show in table 3.1.

**Table 3.1** Gravimetric Factor (GF) is used to create glass samples from precursors.

Formula	Precursor	Gravimetric Factor (GF)
$\text{Li}_2\text{O}$	$\text{Li}_2\text{CO}_3$	2.473
$\text{BaO}$	$\text{BaCO}_3$	1.2871
$\text{P}_2\text{O}_5$	$\text{NH}_4\text{H}_2\text{PO}_4$	1.6208
$\text{Gd}_2\text{O}_3$	$\text{Gd}_2\text{O}_3$	1
$\text{CeF}_3$	$\text{CeF}_3$	1

The procedure for preparing the precursor for 20 grams of phosphate glass with the formula  $61.5\text{P}_2\text{O}_5: 10\text{Li}_2\text{O}: 10\text{BaO}: 18\text{Gd}_2\text{O}_3: 0.5\text{CeF}_3$  is shown in table 3.2. After we measured properties of glass, that we found the sample of host glasses after fabricated by conventional melting-quenching method. The process of melting the mixtures in an alumina crucible in the electric furnace at  $1200^\circ\text{C}$  followed by pouring the melted glass into a graphite mold at ambient atmosphere is a common method for the

fabrication of glass samples. This process ensures that the glass is formed in the desired shape and structure. After the glass samples are solidified at room temperature, they often undergo an annealing process in an electric furnace at around 500°C for several hours. The purpose of annealing is to reduce any residual stresses that may have been created during the cooling process. These stresses can cause the glass to be more brittle and prone to cracking or breaking. Annealing allows the glass to cool gradually and uniformly, resulting in a more stable and durable final product. It is important to note that the exact parameters of the melting and annealing process may vary depending on the specific composition and desired properties of the glass. Additionally, it is crucial to ensure that the fabrication process is carried out carefully and accurately to avoid any defects or impurities in the final product. Any defects or impurities can impact the properties of the glass and its suitability for certain applications. Lastly, samples were cut and polished with dimension of 1.0 x 1.5 x 0.3 cm<sup>3</sup>. for further properties characterizations.

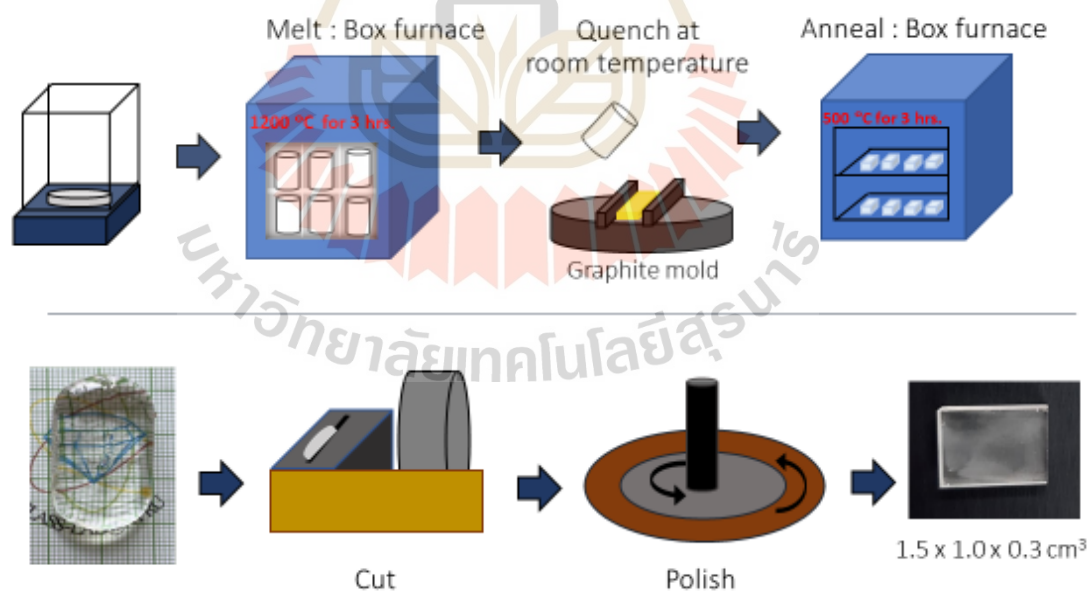


**Figure 3.1** A schematic overview of synthetic glass samples, from precursors preparation to sample preparation for characterization-ready dimensions.



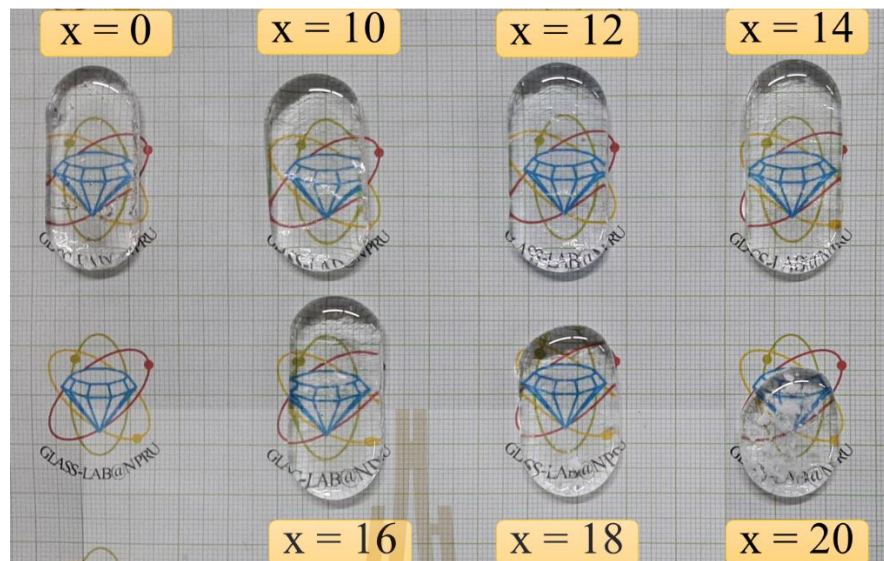


**Figure 3.2** The bulk glass sample of phosphate-host glass with varying  $Gd_2O_3$  concentrations.

### 3.2.2 Various concentration of Cerium Oxide

In this study, the focus was on investigating samples of lithium barium gadolinium phosphate glass doped with cerium from two different compositional systems. The raw materials were carefully calculated to ensure that they were stoichiometrically correct, and then mixed in the following compositions:

The first system consisted of  $10Li_2O : 10BaO : xGd_2O_3 : (79.5-x)P_2O_5 : 0.5CeF_3$  ( $x = 8, 10, 12, 14, 16, 18$ ). The  $Gd_2O_3$  concentration was varied between 8 mol% and 20 mol%, while the concentration of  $CeF_3$  was kept constant at 1.0 mol%.

The second system, which was further investigated, consisted of  $10Li_2O : 10BaO : 18Gd_2O_3 : (62-x)P_2O_5 : xCeF_3$  ( $x = 0.1, 0.3, 0.5, 1.0, 1.5, 2.0$ ) and varying concentrations of  $CeF_3$ . In this case, the  $Gd_2O_3$  concentration was fixed at 18 mol%, while the concentration of  $CeF_3$  was varied between 0.1 mol% and 2.0 mol%.

The precursors in this study were lithium oxide ( $Li_2O$ ), ammonium phosphate ( $NH_4H_2PO_4$ ), barium oxide ( $BaO$ ), gadolinium (III) oxide ( $Gd_2O_3$ ) and cerium (III) fluoride ( $CeF_3$ ).

**Table 3.2** The method for calculating the amount of precursors for used to prepare 61.5P<sub>2</sub>O<sub>5</sub>: 10Li<sub>2</sub>O: 10BaO: 18Gd<sub>2</sub>O<sub>3</sub>: 0.5CeF<sub>3</sub> Phosphate glass sample.

Formula	MW	mol%	mol	g/mol	total mass	1 g of glass sample	20 g of glass sample	GF	Mass (g) of precursor (g)
Li <sub>2</sub> O	29.8814	10	0.1	2.98814	171.8519	0.017388	0.3477576	2.473	0.8600045
BaO	153.3264	10	0.1	15.33264	171.8519	0.08922	1.7844017	1.2871	2.2967034
Gd <sub>2</sub> O <sub>3</sub>	362.4982	18	0.18	65.24968	171.8519	0.379686	7.5937106	1	7.5937106
P <sub>2</sub> O <sub>5</sub>	141.9445	61.5	0.615	87.29588	171.8519	0.507972	10.159432	1.6208	16.466408
CeF <sub>3</sub>	197.1102	0.5	0.005	0.985551		0.005735	0.1146977	1	0.1146977
total	=884.7607	=100%	=1	=171.8519		= 1	20		=27.33152

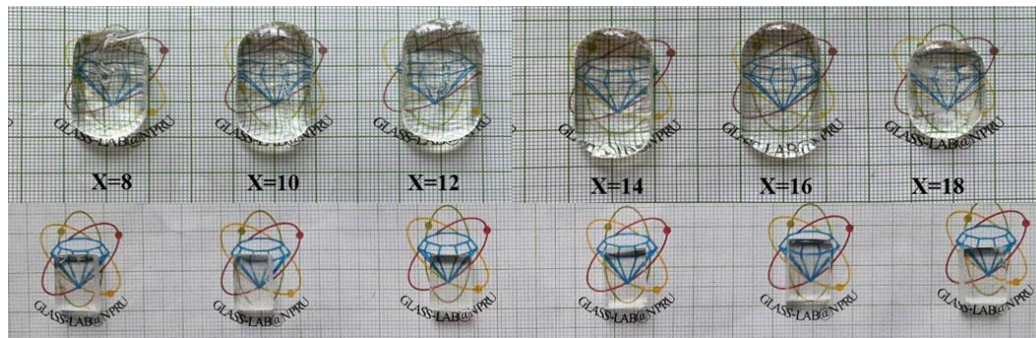


**Figure 3.3** The phosphate glass samples containing different concentrations of  $Gd_2O_3$  were prepared and subsequently cut and polished.

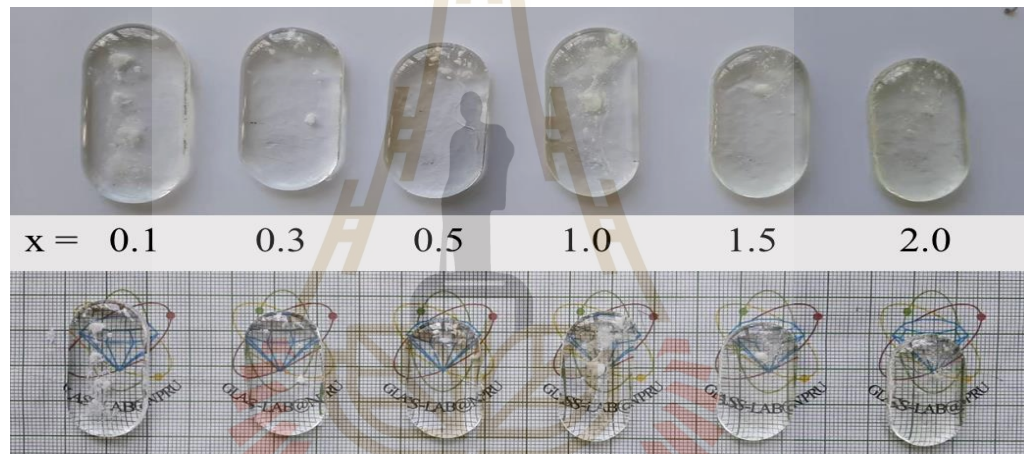


**Figure 3.4** The samples of bulk glass in this study were composed of varying concentrations of  $CeF_3$ .

### 3.3 Measurements

The density of glass samples was measured in room temperature by 4-digit Microbalance with Density Measurement Kit [AND HR-200]. This method can measure a glass sample by first weighing it in air ( $W_{air}$ ) and then again in water ( $W_{liq}$ ).

When we have information about both of them. The Archimedes method, denoted by the equation (1), will be used to calculate the density of the glass sample. The data will be weighed and calculated more than 3 data per sample, for data on average, in order to improve the reliability of the data.

Abbe refractometer was used to study the reflective index (Atago). The ATIGO-3T multi-wavelength Abbe refractometer has been designed to offer improved measuring precision while remaining user-friendly. This has been achieved through fundamental adjustments to the optical system, the employment of a larger scale, the incorporation of a high-intensity lamp, and the use of a double control knob to enable both faster and more precise system control. In this research, we calibrate utilizing filter light 589 nm, crystal  $n_D=1.5161$ .



(a)

(b)

**Figure 3.5** (a) Density measurement kit (A&D HR-200) 4-digit Microbalance with density kit and (b) Multi wavelength Abbe refractometer (ATIGO-3T) (Refractive Index measurement from 1.3-1.7) (<http://dept.npru.ac.th/cegm/index.>).

Characterization of the photoluminescence behavior of the doped samples was carried out using a spectrofluorometer (cary-Eclipse), with an excitation source of the xenon flash lamp, and with a resolution of less than 1.5 nm.





**Figure 3.6** (a) Fluorescence Spectrophotometer (Cary-Eclipse)(Photo-luminescence measurement of material in visible region from 200 - 900 nm) and (b) UV-VIS spectrophotometer (Cary-50) (and %T measurements in the range of 200 - 1100 nm with CIE L\*a\*b\*color coordinate software).

The study aimed to investigate the radioluminescence properties of materials using an x-ray induced optical luminescence spectrometer. To conduct the measurements, the spectrometer employed an Inel X-ray generator that featured a 2KW Cu-anode. The sample holder used in the spectrometer had a fixed size, which limited the maximum sample size to less than 1.5 x 1.5 cm. Therefore, in order to ensure compatibility with the apparatus, the researchers had to use samples that were smaller than 1.5 x 1.0 x 0.5 centimeters. This required the polishing of glass samples to the desired size before conducting the measurements. The x-ray beam used in the experiment was set at 50 kV, and the number of X-ray photons produced by the x-ray tube was determined by the selection of a setting at 30 mA. These parameters were carefully selected to provide the researchers with accurate and reliable results in their investigation of the radioluminescence properties of the materials under study.

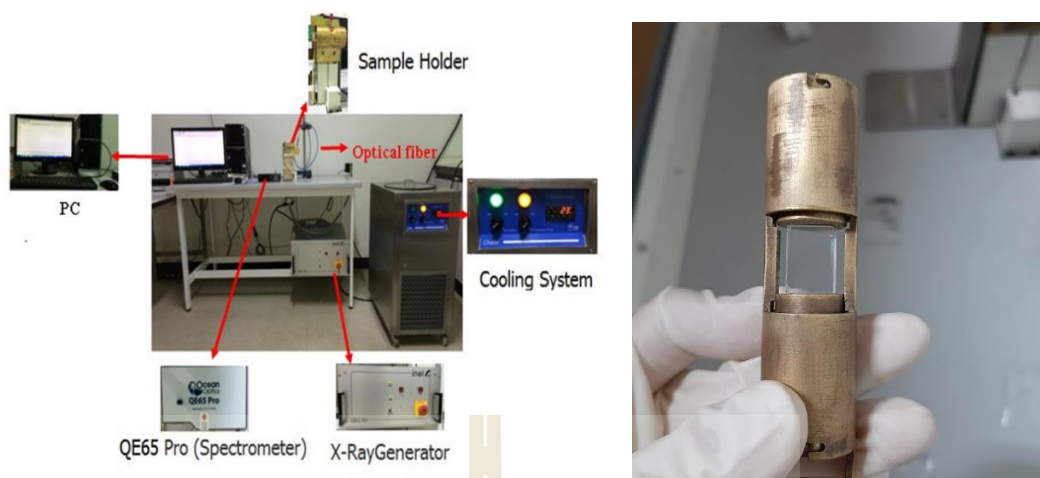


**Figure 3.7** X-Rays Induced Optical Luminescence (Radioluminescence) (Inel x-ray generator with 2 kW Cu-anode) (Spectrum detected by fiber optics spectrometer, QE65000 Ocean Optics) (Radioluminescence measurement of material in visible region from 200 - 900 nm).

The optical properties of energy absorption and transparency were investigated using the UV-VIS spectra acquired by a UV-VIS spectrophotometer (Cary-50). The luminescence decay curve of glasses is an essential characteristic to investigate as it provides crucial information on the lifetime of excited states within the glass material. In this study, the luminescence decay curves of the glasses were analyzed using the Deltapro™ fluorescence lifetime system manufactured by HORIBA Scientific. This system is equipped with a 286 nm DeltaDiode light source (DD-290) and a picosecond photon detector (PPD-850) to measure the luminescence decay of the glass samples accurately. The decay curves were measured by exciting the glass samples with the DeltaDiode light source and monitoring the resulting emission using the picosecond photon detector. The decay curves obtained were then analyzed to determine the lifetime of the excited states and other important luminescence parameters. These results were used to further optimize the composition of the glass samples and improve their luminescence properties. The use of advanced equipment such as the Deltapro™ fluorescence lifetime system in this study ensures accurate and reliable data analysis.

The X-ray diffraction pattern was obtained by Bruker D2 PHASER using Cu X-ray tube at 30 kV/10A and alignment within 0.02 degree. using a mortar and pestle to grind the sample completely before placing the sample in the sample holder. we measured. The energy dispersive X-ray characterized by FE-SEM/WDX/EDX (JEOL JSM 7800F) at 20 keV (<http://cste.sut.ac.th/2014/>).



**Figure 3.8** (a) Bruker D2 PHASER and (b) FE-SEM/WDX/EDX (JEOL JSM 7800F).

In order to analyze the local environment of the elements in the glass samples, X-ray absorption near-edge structure (XANES) spectra were obtained. The XANES spectra provide valuable information on the electronic and geometric structures of the sample. The XANES measurements in this research were carried out at the XAS facility (BL-5.2) of Siam Photon Laboratory, Synchrotron Light Research Institute located in Nakhon Ratchasima, Thailand. The measurements were conducted with the storage ring running at 1.2 GeV and a beam current of 70-140 mA during the measurement, ensuring high-quality data. The use of synchrotron radiation for XANES measurements is beneficial as it provides high-intensity, high-energy X-rays that can penetrate deep into the sample, allowing for a more detailed analysis of the sample's structure. Overall, the XANES spectra obtained in this study allowed for a deeper understanding of the glass samples' electronic and geometric structures and contributed to the optimization of their properties for potential applications. It is important to note that



proper acknowledgment was given to the XAS facility and the Synchrotron Light Research Institute for providing access to the equipment and facility for the success of this study. The Current SUT-NANOTEC-SLRI beamline setup show in figure 33(a). In this beamline, the measured energy range is 1810 eV to 13000 eV, and the element setup has two modes: transmission mode with ion chambers and fluorescence mode with a four-element silicon drift detector, with beam sizes of 13 mm (width) 1 mm (height) and 20 mm (width) 1 mm (height), respectively, at the sample. For the purpose of investigating the oxidation of cerium in phosphate glass powder or our sample, we measured the L-III edge of cerium in the energy range of 5700-5800 eV, focusing on XANE spectra. The experiment is set up in fluorescence mode since the concentration of cerium is less than 5%; the concentration of  $\text{CeF}_3$  in glass samples is measured between 0.5 and 2.0 mol%. The crystal type configuration is Ge(220) with a 2d spacing ( $A^\circ$ ) of 4.001 and an Energy range of 3440 - 12100 eV. The phosphate glass powder was prepared for measurement by placing it on capton tape, which is displayed in figure 28(b).

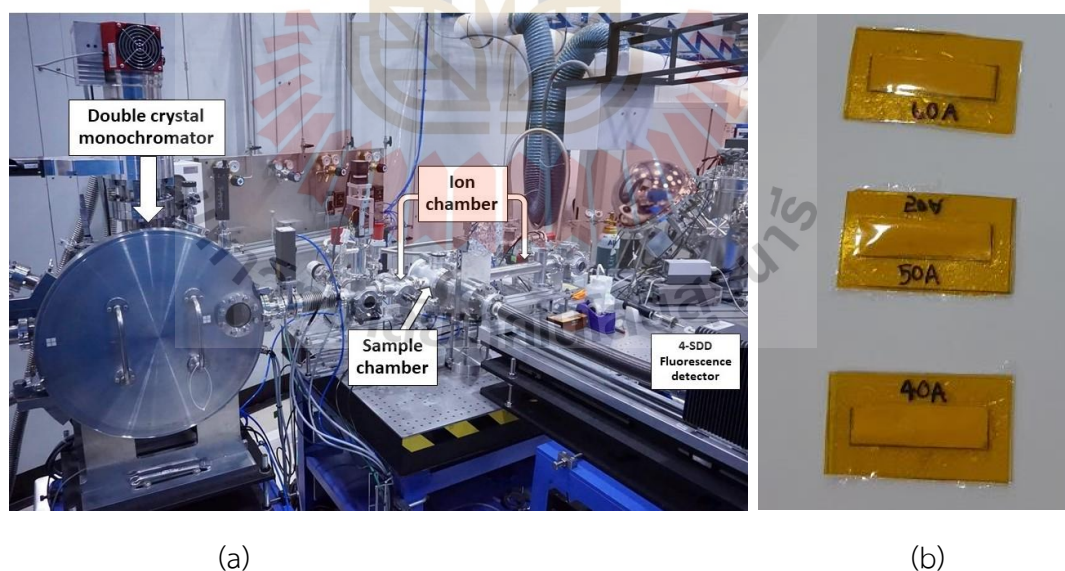


**Figure 3.9** Current SUT-NANOTEC-SLRI beamline setup at BL5.2 (<https://www.sri.or.th/en/sut-nanotec-slri.html>).

Finally, Compton scattering is a crucial phenomenon in radiation detection, and its detection requires specialized equipment. In this study, the Compton scattered rays were monitored using a rotatable scintillator detector placed in the scattering plane. A 2 NaI (Tl) detector with an 8 percent energy resolution at 662 keV (BICRON model 2M2/2) and a CANBERRA photomultiplier tube base type 805-5 were used in this experiment. The optimal distance between the source and scatterer was determined to be 20 cm, as was the optimal distance between the scatterer and detector, as shown in figure 3.10. The spectra were recorded using a CANBERRA PC-based multi-channel analyzer (MCA). The MCA detector's spectrum provided occurrence counts in each of 1024 bins, split by voltage. We varied the angle of the scatter detector and collected MCA readings. The different angles ( $\theta$ ) were used to generate various gamma ray energies. The use of specialized equipment such as a rotatable scintillator detector and a multi-channel analyzer in this study ensured accurate and reliable data collection and analysis.

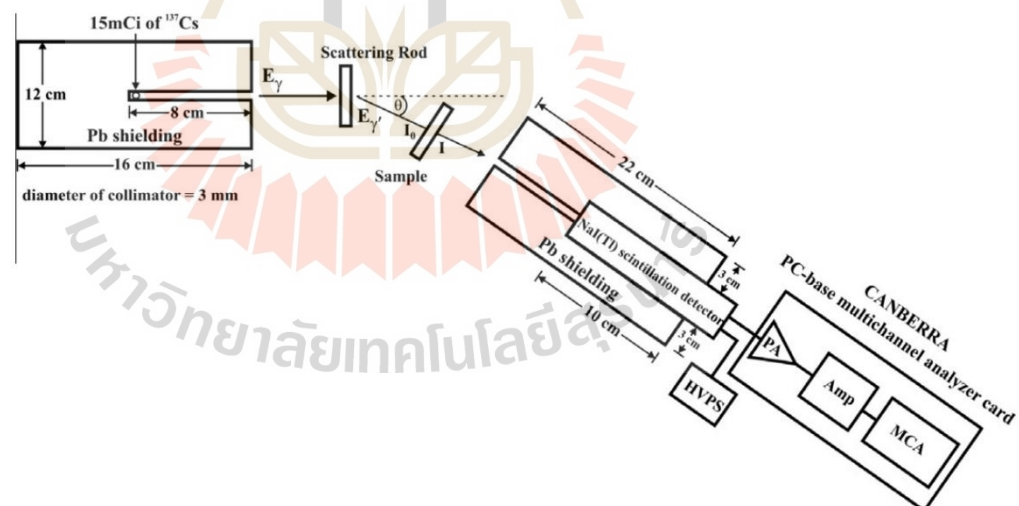


**Figure 3.10** Schematic of the Compton scattering technique for mass attenuation coefficient measurement (Limkitjaroenporn et al., 2013).

## CHAPTER IV

### RESULT AND DISCUSSION

In this section, we will present the results of our synthesized glass samples and explain the rationale behind our selection of certain compounds to enhance the properties of the glass material for potential use in scintillator or shielding devices. To facilitate the organization of the results, we have listed the samples in table 4.1 which will be referred to in subsequent parts of this section. The code names assigned to the samples in table 4.1 serve to simplify the identification of the series of glasses under investigation, as well as to facilitate comprehension of the varied compound effects on the improvement of the glass material properties in this research.

**Table 4.1** Code name of samples.

Formula	Code name
$10\text{Li}_2\text{O}:10\text{BaO}:x\text{Gd}_2\text{O}_3:(79.5-x)\text{P}_2\text{O}_5$ ( $x = 0, 10, 12, 14, 16, 18, 20$ )	Li-Ba-xGd phosphate glass various concentration of $\text{Gd}_2\text{O}_3$ ( $x = 0, 10, 12, 14, 16, 18, 20$ )
$10\text{Li}_2\text{O}:10\text{BaO}:x\text{Gd}_2\text{O}_3:(79.5-x)\text{P}_2\text{O}_5:0.5\text{CeF}_3$ ( $x = 8, 10, 12, 14, 16, 18$ )	Li-Ba-xGd-0.5Ce phosphate glass various concentration of $\text{Gd}_2\text{O}_3$ ( $x = 8, 10, 12, 14, 16, 18$ )
$10\text{Li}_2\text{O}:10\text{BaO}:18\text{Gd}_2\text{O}_3:(62-x)\text{P}_2\text{O}_5:x\text{CeF}_3$ ( $x = 0.1, 0.3, 0.5, 1.0, 1.5, 2.0$ )	Li-Ba-18Gd-xCe phosphate glass various concentration of $\text{CeF}_3$ ( $x = 0.1, 0.3, 0.5, 1.0, 1.5, 2.0$ )

All synthesized samples underwent comprehensive analysis using a range of fundamental techniques to determine their optical, structural, and radiation properties, in order to facilitate the further improvement and development of the material, consistent with the scope of the experiments outlined at the outset.

#### 4.1 Phosphate host glass $10\text{Li}_2\text{O} : 10\text{BaO} : x\text{Gd}_2\text{O}_3 : (80-x) \text{P}_2\text{O}_5 : \text{Li-Ba-xGd}$ ( $x = 0, 10, 12, 14, 16, 18, 20$ )

Initially, we must identify the appropriate host glass for applying an element with enhanced scintillator or shielding material properties. The fundamental characteristics of the glass that will be used for this component. For us to identify phosphate host glasses that meet these requirements, they must be completely molten at low temperatures, have a high degree of transparency, a high density, a low molar volume, and the ability to emit in the ultraviolet spectrum. The density of the sample host glass as well as its molar volume are presented in figure 4.1(a). They increase up as the percentage of  $\text{Gd}_2\text{O}_3$  in the sample increases. This is because of the higher atomic mass of  $\text{Gd}_2\text{O}_3$ , which takes the place of  $\text{P}_2\text{O}_5$ , and the fact that  $\text{Gd}_2\text{O}_3$  has a higher melting point than  $\text{P}_2\text{O}_5$ , which causes the molar volume will go up as a result. The Li-Ba-xGd phosphate glass containing the greatest quantity of  $\text{Gd}_2\text{O}_3$  and the lowest  $\text{P}_2\text{O}_5$  load was found to have the highest refractive index value when it was measured at 18mol% of  $\text{Gd}_2\text{O}_3$ , as shown in figure 4.1(b). This glass also had the lowest  $\text{P}_2\text{O}_5$  load. It is evident that the refractive index increases when an element with a lower atomic mass (A) is replaced by an element with a higher atomic mass on a glass structure.

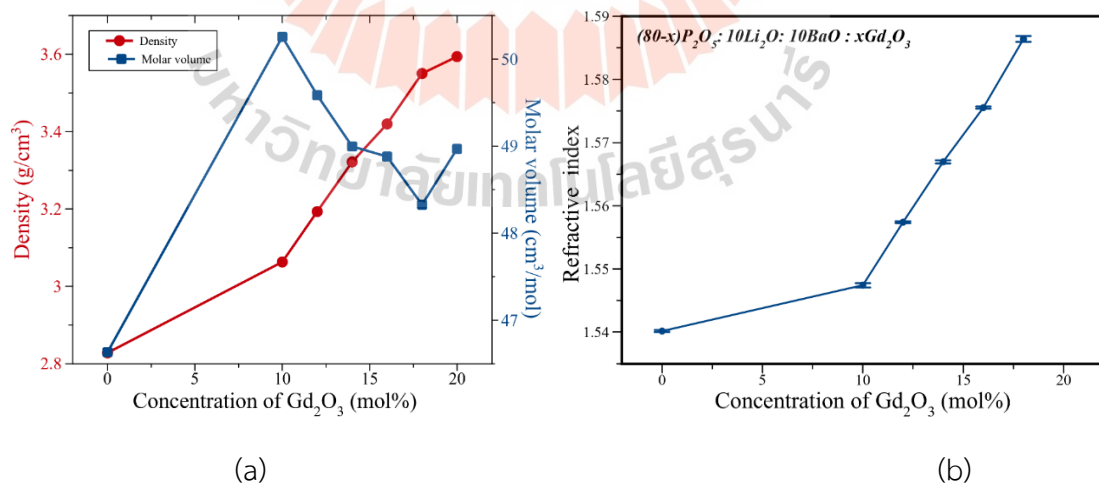


**Figure 4.1** (a) The density and molar volume of Li-Ba-xGd phosphate glasses and (b) The refractive index of Li-Ba-xGd phosphate glasses.

The optical properties were characterized by UV-vis spectroscopy for measured percent transmittance of the Li-xGd phosphate host glass samples (shown in figure 4.2). It measures the intensity of light after passing through a sample and compares it to the intensity of light before it passes through the sample then shown the transmittance in figure 36. At 12 mol% of Gd<sub>2</sub>O<sub>3</sub> have transmittance cut-off at shortest wavelength or highest energy. The cut-off wavelength of Li-Ba-xGd phosphate host glass are fluctuate. It is a specific character of phosphate glass, which is an asymmetric center within the glass structure that accounts for the relatively poor mechanical properties.

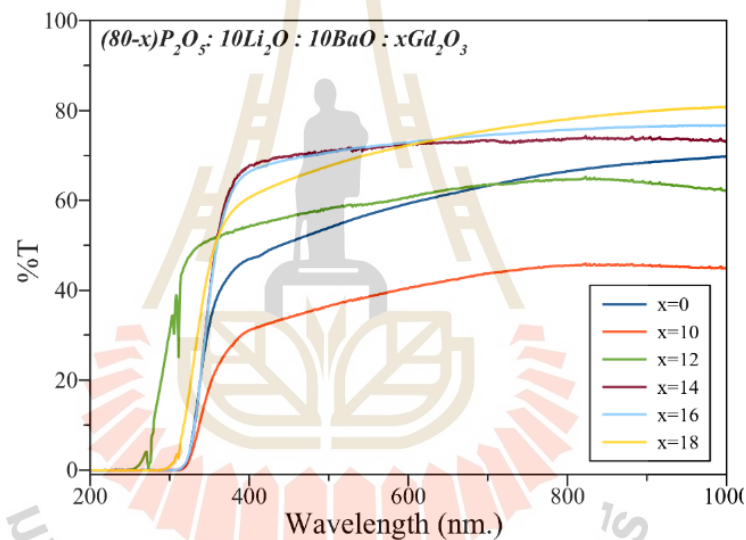


Figure 4.2 The transmission curves of Li-Ba-xGd phosphate glass.

To understand the optical properties of the glass material, we calculated the optical band gap from the absorption spectra using Tauc's relation. This allowed us to estimate the energy required for indirect and direct transitions between electronic states in the material. The resulting data was presented in figure 4.3(a) and (b), which showed the linear portion of the plot that was extrapolated to obtain the optical band gap ( $E_g$ ) value for both direct and indirect transitions.

We also analyzed the relationship between the percent transmittance and the optical band gap value. This allowed us to determine how the transmission of light

through the material was influenced by the size of the optical band gap. The results of our analysis were summarized in table 4.2, which showed the values of the indirect and direct optical band gaps for the glass material.

The optical band gap is an important parameter that characterizes the energy required for electronic transitions in a material. By analyzing the absorption spectra of the glass material and applying Tauc's relation, we were able to estimate the indirect and direct optical band gaps, which were found to be dependent on the percent transmittance of the material. This information can be useful in understanding the optical properties and potential applications of the glass material.

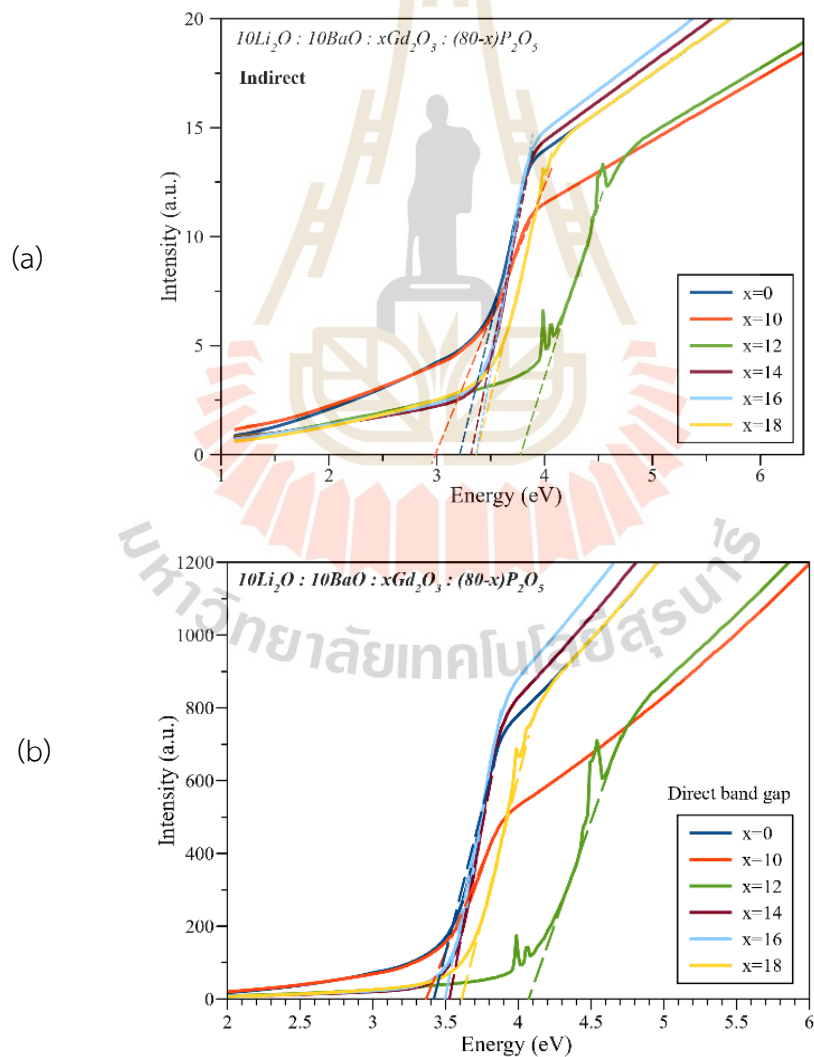


**Figure 4.3** The optical band gap of Li-Ba-xGd for (a) Indirect band gap and (b) Direct band gap.



**Table 4.2** Data of indirect band gap of samples with various concentration of  $Gd_2O_3$  of Li-Ba-xGd-0.5Ce.

$Gd_2O_3$ (mol%)	Optical Band gap(eV)	
	Indirect	Direct
x = 0	$3.16 \pm 0.05$	$3.48 \pm 0.05$
x = 10	$2.95 \pm 0.05$	$3.36 \pm 0.05$
x = 12	$3.72 \pm 0.05$	$4.05 \pm 0.05$
x = 14	$3.28 \pm 0.05$	$3.51 \pm 0.05$
x = 16	$3.30 \pm 0.05$	$3.55 \pm 0.05$
x = 18	$3.37 \pm 0.05$	$3.63 \pm 0.05$

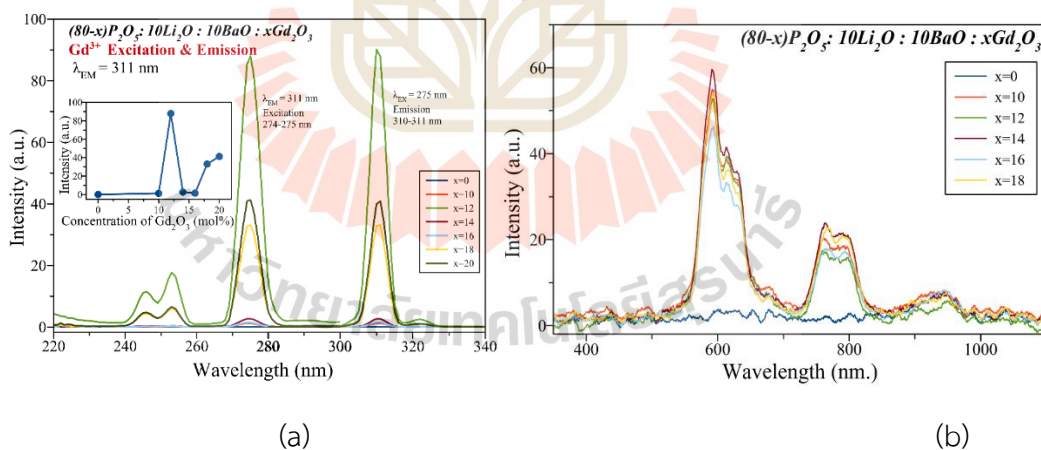


**Figure 4.4** (a) PL result of spectra of  $Gd^{3+}$  excitation (b) Radioluminescence spectra of Li-ba-xGd phosphate glasses at room temperature.

In order to identify phosphate host glass and evaluate its potential for use in scintillator devices, we conducted a series of experiments using Li-Ba-xGd glass samples. Photoluminescent spectroscopy (PL) was used to assess the ability of the glass sample to emit ultraviolet light and detect high energy. The presence of



Gadolinium in the glass sample enabled us to excite  $Gd^{3+}$  at a wavelength of 275 nm, which resulted in the emission of ultraviolet light at a peak wavelength of 311 nm. This emission peak was observed in the PL spectra of Li-Ba-xGd glass samples containing 12 mol% of  $Gd_2O_3$ . Radioluminescence spectroscopy was used to investigate the properties of scintillator devices made using Li-Ba-xGd glass samples. The  $Gd_2O_3$  component of Li-Ba-xGd glass samples allowed for the detection of radioluminescence and UV-Vis emission, which is an important characteristic for scintillator materials used in radiation detection applications.

Based on the results of our experiments, we concluded that Li-Ba-xGd glass has potential for use in scintillator devices. The next step is to further optimize the properties of the Li-Ba-xGd host glass to improve the performance of scintillator devices. In summary, our experiments demonstrated the importance of understanding the photoluminescent and radioluminescent properties of glass materials in order to identify potential scintillator materials for use in radiation detection applications. By investigating the properties of Li-Ba-xGd glass samples, we were able to identify a promising candidate for use in scintillator devices.

#### 4.2 Phosphate glasses $10Li_2O: 10BaO: xGd_2O_3: (79.5-x) P_2O_5$ ( $x = 8, 10, 12, 14, 16, 18$ ) doped 0.5 mol% of $CeF_3$

The modification of lithium barium gadolinium phosphate glass doped with cerium was carried out through two series systematic routes. The first route involved changing the content of  $Gd_2O_3$  to investigate the optimal concentration of this compound in the  $10Li_2O: 10BaO: x Gd_2O_3: (79.5-x) P_2O_5: 0.5CeF_3$  glass. The glass samples obtained through this route were found to be transparent and colorless, as depicted in figure 3.3. To verify that the glass is an amorphous material, we utilized X-ray diffraction (XRD) and found that the XRD pattern consists of a broad and hump spectrum of  $10Li_2O: 10BaO: x Gd_2O_3: (79.5-x)P_2O_5 : 0.5CeF_3$ . This pattern indicates that the structure of the glass does not exhibit long-range order, as crystals do, and peak locations are therefore not detectable. The XRD data is presented in figure 4.5.

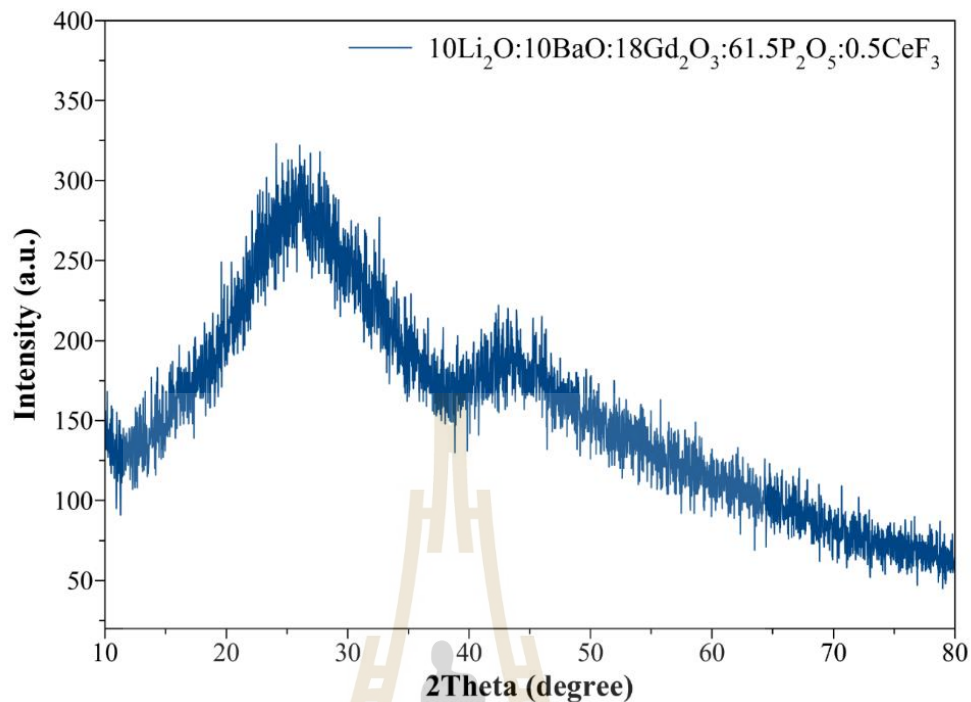


**Figure 4.5** XRD pattern of Li-Ba-xGd-0.5Ce at x=18 mol% phosphate glass sample.

Archimedes' method is a principle used in measuring the density of materials. The method relies on the fact that when an object is immersed in a fluid, it experiences an upward force equal to the weight of the fluid it displaces. This principle is known as the buoyant force. When the weight of the object is known, the buoyant force can be used to determine the volume of the displaced fluid, and hence, the density of the object.

In this study, the density of phosphate glass samples was measured using the Archimedes' method. The glass samples contained varying concentrations of  $Gd_2O_3$ . The results of the density measurements revealed that as the concentration of  $Gd_2O_3$  increased, the density of the phosphate glass samples also increased up to a certain point. It was found that the increase in density can be attributed to the higher atomic mass of the Gd ion compared to the P ion in the glass network matrix. At a certain point, the density increments slightly decreased when the  $Gd_2O_3$  content was further increased. Then shown in figure 4.6 (a), this decrease in density increment could be due to the increased atomic packing in the glass sample.

These results were consistent with the changes observed in the samples' molar volume and refractive index, which tended to decrease and increase, respectively, the results of the density measurements are shown in figure 4.6(a) and (b) with an increment in  $Gd_2O_3$  content. The molar volume is a measure of the volume occupied by one mole of the substance, while the refractive index is a measure of how much the light bends when it passes through the material. The transparent Li-Ba-xGd-0.5Ce phosphate glass with 18 mol% of  $Gd_2O_3$  was selected for further investigations because it had the highest density and refractive index. These findings indicate that the Archimedes' method is a reliable and accurate technique for measuring the density of phosphate glass samples with varying  $Gd_2O_3$  concentrations.

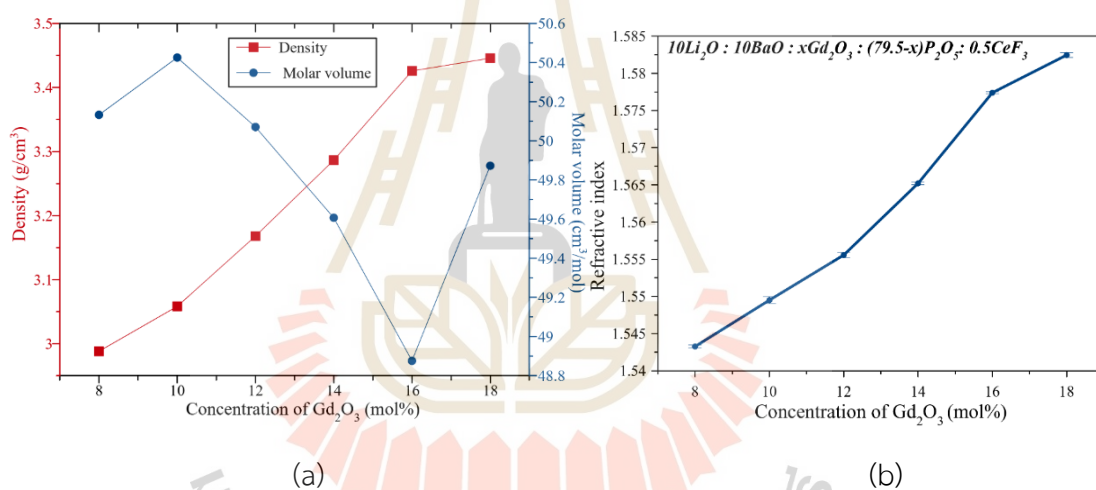


**Figure 4.6** (a) The density and molar volume of Li-Ba-xGd-0.5Ce phosphate glasses and (b) The refractive index of Li-Ba-xGd-0.5Ce phosphate glasses.

The photoluminescence properties of materials provide important information about their optical and electronic properties. In the case of Li-Ba-xGd-0.5Ce phosphate glasses, the emission spectra of  $Gd^{3+}$  ion was obtained with an excited photon at  $\lambda_{Ex} = 275$  nm, which corresponds to the excitation of  $6I_1(Gd^{3+})$  state. The emission spectra of the Li-Ba-xGd-0.5Ce ( $x = 8, 10, 12, 14, 16, 18$ ) phosphate glass samples emitted wavelengths in the range of 335 to 346 nm, which corresponds to the  $5d_2(Ce^{3+})$  state emission (Wisniewski et al., 2008). These results show that the intensity of

luminescence of  $Gd^{3+}$  excitation was highest at the  $Gd_2O_3$  concentration of 18 mol% and lowest at 8 mol%, indicating that the  $Gd_2O_3$  concentration can significantly affect the intensity of luminescence. This suggests that changes in  $Gd_2O_3$  concentration may lead to changes in the intensity of luminescence.

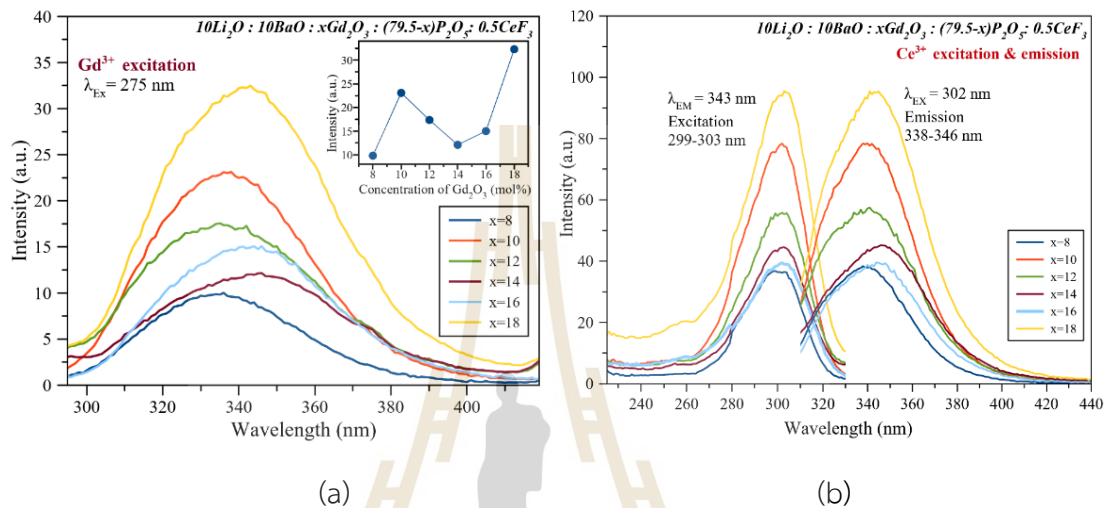


**Figure 4.7** The photoluminescence (PL) results show two distinct spectra for the Li-Ba-xGd-0.5Ce phosphate glasses: (a) excitation spectra of  $Gd^{3+}$  and (b) excitation and emission spectra of  $Ce^{3+}$ .

The excitation and emission spectra of Li-Ba-xGd-0.5Ce phosphate glass of  $Ce^{3+}$  under excitation at  $\lambda_{EX} = 302$  nm and emission at  $\lambda_{EM} = 343$  nm were also studied. The  $Ce^{3+}$  emission spectra appeared to peak in the range of 338 to 346 nm due to electron transfer from  $5d_1 \rightarrow 4f_1$ , while the excitation spectra appeared to peak in the range of 299 to 303 nm due to energy transfer from  $4f_1 \rightarrow 5d_1$  (Baccara et al., 2001). These results indicate that the energy transfer from  $Gd^{3+}$  to  $Ce^{3+}$  is responsible for the emission and excitation spectra observed in the Li-Ba-xGd-0.5Ce phosphate glass samples. The study of the photoluminescence properties of Li-Ba-xGd-0.5Ce phosphate glasses provides important insights into the materials' electronic and optical properties, which are important for various applications in optoelectronic devices, lasers, and luminescent materials.

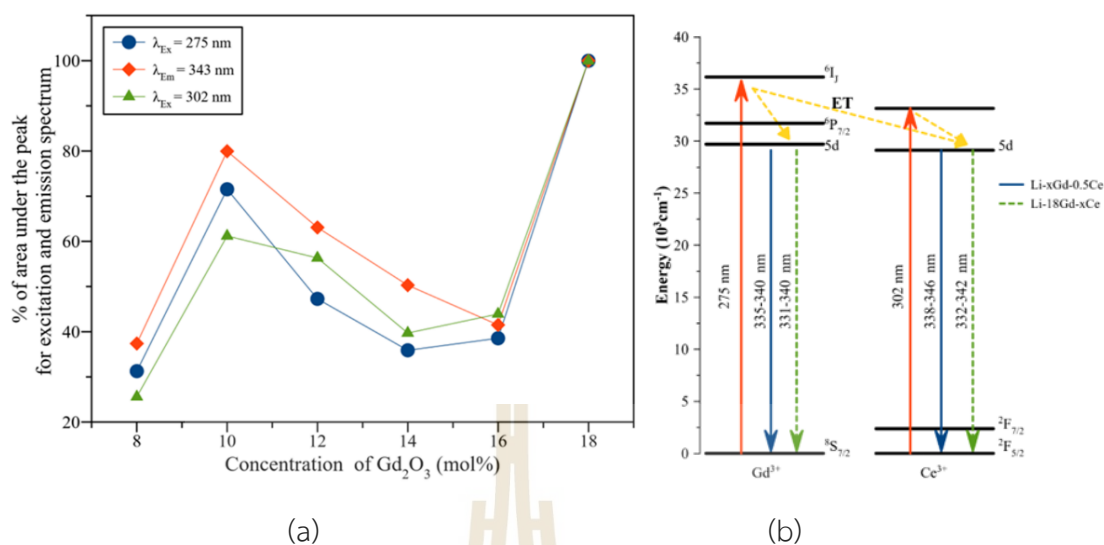


**Figure 4.8** (a) The percentage of the area under the emission peak in the excitation spectrum was analyzed for varying concentrations of  $Gd_2O_3$ . (b) A partial energy level diagram was presented to illustrate the potential energy transfer pathways from  $Gd^{3+}$  ions to  $Ce^{3+}$  ions in both Li-xGd-0.5Ce and Li-18Gd-xCe phosphate glass systems.

In figure 4.8(a), the percent of area under the peak for the emission of excitation spectra at different concentrations of  $Gd_2O_3$  is shown. The area under the peak is largest at 18 mol%, indicating that this composition is the most appropriate choice for optimum performance. In figure 4.8(b), the partial energy level diagram of  $Gd^{3+}$  and  $Ce^{3+}$  is presented along with the possible energy transfer from  $Gd^{3+}$  ions to  $Ce^{3+}$  ions in the Li-xGd-0.5Ce phosphate glasses. The broad emission bands of  $Gd^{3+}$  cover the broad emission and excitation bands of  $Ce^{3+}$ , which means that the emission spectra of  $Gd^{3+}$  consists of emission and excitation spectra of  $Ce^{3+}$ . Furthermore, some parts of the spectra of  $Ce^{3+}$  emission and excitation are overlapped due to electron transition. The near energy states are used (approximately 0.1-0.2 eV) for the excited electron from 5d level, which leads to fast decay time, as reported in previous studies (Ronda and Jüstel, 2008 and Bessi re et al., 2005). This suggests that the energy transfer from  $Gd^{3+}$  ions to  $Ce^{3+}$  ions within the glass matrix is responsible for the excellent luminescence properties observed in this study.

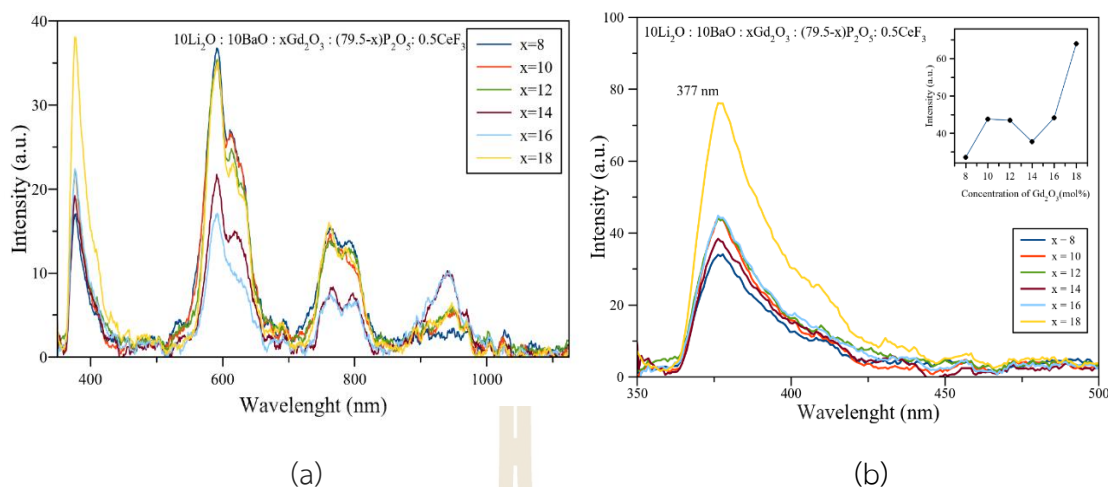


**Figure 4.9** (a) Radioluminescence spectra of Li-ba-xGd-0.5Ce phosphate glasses at room temperature and (b) zoom in emission range of  $\text{Ce}^{3+}$ .

In radioluminescence, a material emits light in response to ionizing radiation, as in the case of  $\text{Ce}^{3+}$  in the Li-xGd-0.5Ce phosphate glass samples. The energy deposited by the ionizing radiation is absorbed by the atoms in the material and excites the electrons to higher energy states. When these electrons return to their original state, they release the excess energy in the form of light. The radioluminescence spectra in figure 4.9 (a,b) shows the emission of  $\text{Ce}^{3+}$  at 377 nm for all Li-xGd-0.5Ce ( $x = 8, 10, 12, 14, 16$ ) phosphate glass samples. The highest emission intensity was observed in the sample containing 18 mol% of  $\text{Gd}_2\text{O}_3$ , which was found to be consistent with the results of photoluminescence excitation of  $\text{Ce}^{3+}$  in Li-Ba-xGd-0.5Ce phosphate glasses. These observations suggest that the high concentration of  $\text{Gd}_2\text{O}_3$  in the samples can produce a high number of photons due to energy transfer from  $\text{Gd}^{3+}$  to  $\text{Ce}^{3+}$ . The efficient energy transfer mechanism between  $\text{Gd}^{3+}$  and  $\text{Ce}^{3+}$  in the glass matrix is responsible for the observed radioluminescence and photoluminescence properties, making it a promising candidate for radiation detection applications.



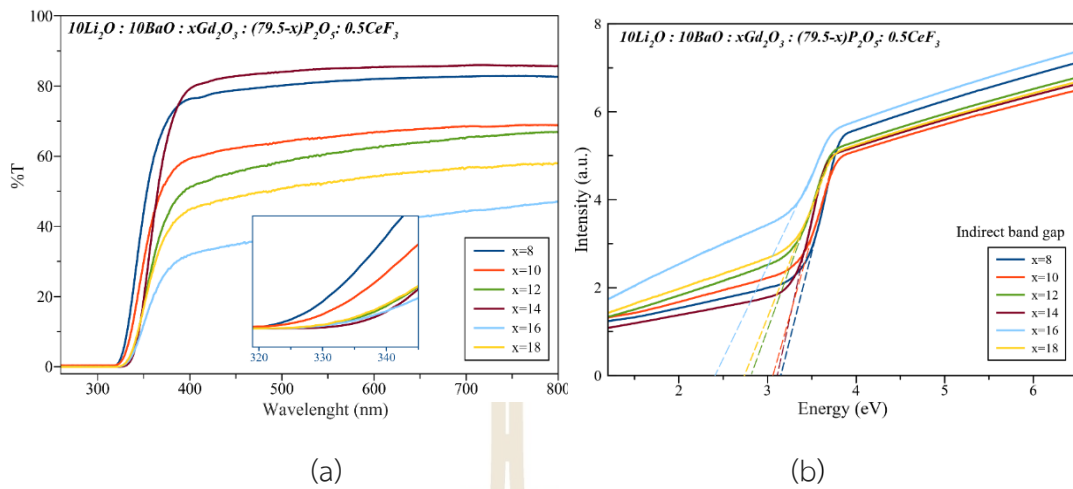


**Figure 4.10** (a) The transmission curves and (b) optical band gap of Li-Ba-xGd-0.5Ce.

The UV-vis data presented in figure 4.10 can be explained by the theory of optical bandgap energy. The shoulder observed in the transmission edge of the Li-Ba-xGd-0.5Ce ( $x = 8, 10, 12, 14, 16$ ) phosphate glasses (as shown in the inserted figure) is attributed to the electronic transitions in the glass matrix. The transmission edges observed at 318-328 nm, with increasing concentration of Gd<sub>2</sub>O<sub>3</sub>, are indicative of a redshift in the absorption edge, which could be attributed to the presence of Gd<sup>3+</sup> ions. The optical bandgap energy can be calculated using the Tauc and Davis-Mott relation, which describes the relationship between the absorption coefficient ( $\alpha$ ) and the incident photon energy ( $h\nu$ ). This relation is given by the following equation:

$$(\alpha h\nu)^n = \beta (h\nu - E_g), \quad (31)$$

where  $\beta$  is a constant (band tailing parameter),  $E_g$  is the energy of optical band gap and  $n$  is the power of transition mode. In figure 4.4(b), the indirect bandgap energy of Li-Ba-xGd-0.5Ce ( $x=8,10,12,14,16,18$ ) phosphate glasses were found to be in the range of 2.4 - 3.2 eV. This is similar to the band gap of semiconductors. The optical band gap energy of all the studied Li-Ba-xGd-0.5Ce phosphate glass samples are summarized in table 4.3. The bandgap of these samples is related to the percent of transmittance shown in figure 4.10(a).

**Table 4.3** The indirect band gap measurements were taken for the Li-Ba-xGd-0.5Ce samples with varying concentrations of  $Gd_2O_3$ .

$Gd_2O_3$ (mol%)	Optical Band gap(eV)	
	Indirect	Direct
x = 8	$3.16 \pm 0.05$	$3.56 \pm 0.05$
x = 10	$3.05 \pm 0.05$	$3.50 \pm 0.05$
x = 12	$2.82 \pm 0.05$	$2.41 \pm 0.05$
x = 14	$3.11 \pm 0.05$	$3.42 \pm 0.05$
x = 16	$2.41 \pm 0.05$	$3.29 \pm 0.05$
x = 18	$2.73 \pm 0.05$	$3.40 \pm 0.05$

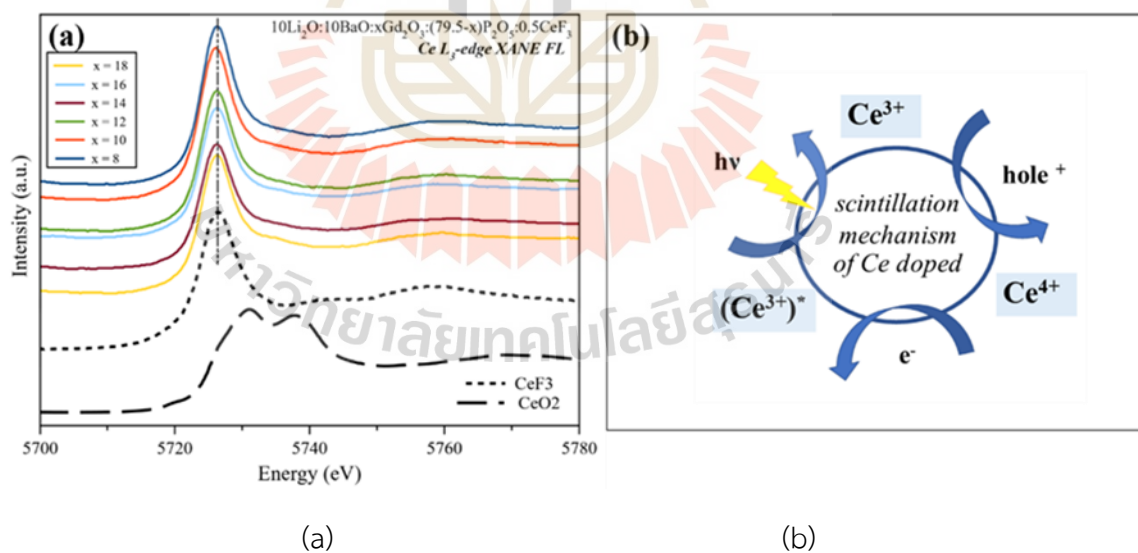


**Figure 4.11** (a) The Ce  $L_3$ -edge X-ray absorption near-edge structure (XANES) of Li-Ba-xGd-0.5Ce phosphate glass was analyzed using linear combination fitting and (b) The luminescence mechanism of Ce doping.

X-ray absorption spectroscopy was used to investigate the oxidation states of  $\text{Ce}^{3+}$  in Li-Ba-xGd-0.5Ce phosphate glass samples. The measurement was carried out using the fluorescence mode and the XANES technique was used to probe the local structure of Ce dopants at  $L_3$ -edge. The XANES spectra of the glass samples were shown in figure 4.11(a). According to the linear combination fit of XANES data, it was found that the majority of Ce ions within the glass matrix incorporated the  $\text{Ce}^{3+}$  charge state. However, there were also some partial existences of the  $\text{Ce}^{4+}$  state as shown in table 4.4. The glass sample with the 18 mol% of  $\text{Gd}_2\text{O}_3$  exhibited a higher value of  $\text{Ce}^{4+}$  state content than the other samples. This can be explained by the energy transfer from  $\text{Gd}^{3+}$  to  $\text{Ce}^{3+}$  which leads to the reduction of  $\text{Ce}^{4+}$  to  $\text{Ce}^{3+}$ . The R-factor, which is the goodness-of-fit value, was calculated from the following equation (32) (Ravel,2020). This information provides insight into the local electronic structure of the glass samples and can help in understanding the scintillation properties of the glasses.

$$\text{R factor} = \frac{\text{sum}((\text{data}-\text{fit})^2)}{\text{Sum}(\text{data}^2)} \quad (32)$$

In the process of making the samples, partial existent  $\text{Ce}^{4+}$  may arise due to oxygen bridging in the melt and quenching process or self-activation of cerium in the samples despite using  $\text{CeF}_3$  compound as the starting precursor. The scintillation mechanisms of the material with Ce dopant can be explained through figure 4.11(b). The luminescence mechanism occurs due to charge transitions between  $\text{Ce}^{3+}$  and  $\text{Ce}^{4+}$  ions which takes place in three steps: (1) The excitation of  $\text{Ce}^{3+}$  by incident radiation, (2) The transfer of energy from  $\text{Ce}^{3+}$  to  $\text{Ce}^{4+}$  via an intermediate state, and (3) The emission of photons by  $\text{Ce}^{4+}$ . This process is known as the  $\text{Ce}^{3+}$ - $\text{Ce}^{4+}$  luminescence center in glasses and is a well-established phenomenon in the literature. (Blahuta et al., 2013).

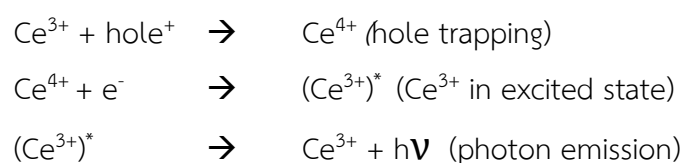


**Table 4.4** The proportion of the oxidation state of cerium.

Concentration of Gd (%mol)	Percent of Ce <sup>3+</sup>	Percent of Ce <sup>4+</sup>	R factor
8	86.32374	13.67626	0.031273
10	87.03949	12.96051	0.032179
12	86.94601	13.05399	0.032833
14	87.7885	12.2115	0.033729
16	85.83624	14.16376	0.035788
18	80.95584	19.04416	0.041747

In order to measure the decay time of the samples, the Deltapro™ fluorescence lifetime system (HORIBA scientific) was employed, which utilized a 286 nm DeltaDiode light source (DD-290) and a picosecond photon detector (PPD-850) to detect luminescence in the visible region. The decay time of the luminescence center was calculated by fitting the data to a two-exponential approximation of the decay curves, as described in equation (33).

$$I(t) = \sum A_i \exp[-t/\tau_i] \quad (33)$$

A scintillating signal with a short decay time ( $\tau$ ) of the luminescent center results in a high-count rate, indicating a fast response. This is a crucial property for a scintillator, as a fast decay time is necessary for detecting radiation events in quick succession. This phenomenon can be explained by the fact that the number of scintillation photons produced per unit of energy deposited is proportional to the inverse of the decay time of the luminescent center (Glodo et al., 2005). Therefore, a faster decay time leads to a higher scintillation light output, making it more sensitive to radiation detection.

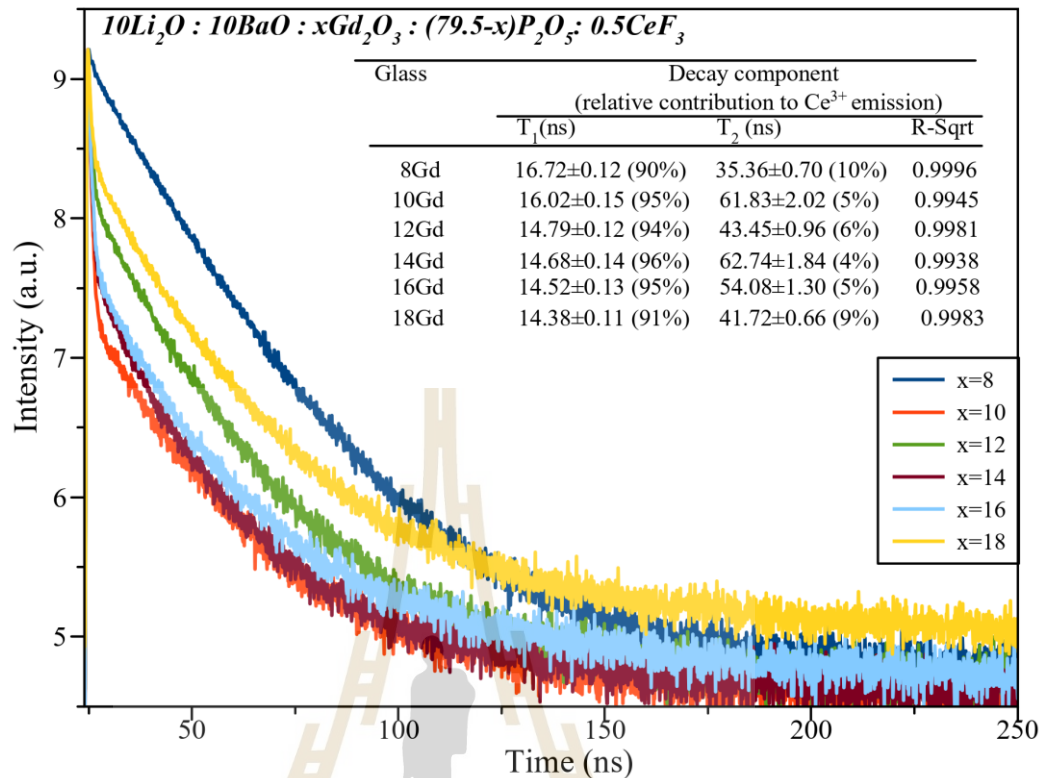


**Figure 4.12** The scintillation pulse shapes of Li-Ba-xGd-0.5Ce phosphate glasses.

The decay time of Li-Ba-xGd-0.5Ce phosphate glasses with varying concentrations of  $\text{Gd}_2\text{O}_3$  and  $\text{CeF}_3$  was measured, and the data is presented in Figure 46. The samples were prepared with the same concentration of  $\text{CeF}_3$ , and the longest decay time was found to be  $16.72 \pm 0.12$  ns for 8 mol% of  $\text{Gd}_2\text{O}_3$ , while the shortest decay time was  $14.38 \pm 0.11$  ns. As the concentration of  $\text{Gd}_2\text{O}_3$  increased, the value of the decay time in these samples decreased, which can be attributed to an increase in the number of electrons and holes, leading to more energy for the transition of excited  $\text{Ce}^{3+}$ . These results confirm the influence of Ce-doping on the decay time and indicate that the fastest decay time was found at 1.0 mol% of  $\text{CeF}_3$ , in addition to the highest emission luminescence. These findings suggest that the addition of  $\text{Gd}_2\text{O}_3$  to Ce-doped Li-Ba-xGd-0.5Ce phosphate glass can influence the decay time, with implications for the design and development of scintillator materials with specific properties.

#### 4.3 Phosphate glasses $10\text{Li}_2\text{O}:10\text{BaO}:18\text{Gd}_2\text{O}_3:(62-x)\text{P}_2\text{O}_5:x\text{CeF}_3$ ( $x = 0.1, 0.3, 0.5, 1.0, 1.5, 2.0$ )

In order to further investigate the effects of cerium fluoride ( $\text{CeF}_3$ ) on the properties of the glass, a new compositional route was studied. This route used a fixed content of  $\text{Gd}_2\text{O}_3$  (18 mol%) and varied the amount of  $\text{CeF}_3$  ( $x = 0.1, 0.3, 0.5, 1.0, 1.5, 2.0$ ) while keeping the amounts of  $\text{Li}_2\text{O}$ ,  $\text{BaO}$ , and  $\text{P}_2\text{O}_5$  constant at 10, 10, and  $62-x$  mol%, respectively. The abbreviated code names of these samples are listed in table 4.1 for ease of reference in subsequent sections. X-ray diffraction patterns of the samples were obtained and are shown in figure 4.13. The broad hump spectrum indicates that the samples are amorphous in nature, meaning that the atoms are not arranged in a regular crystalline lattice structure. This is in contrast to the sharp peaks observed in X-ray diffraction patterns of crystalline materials.

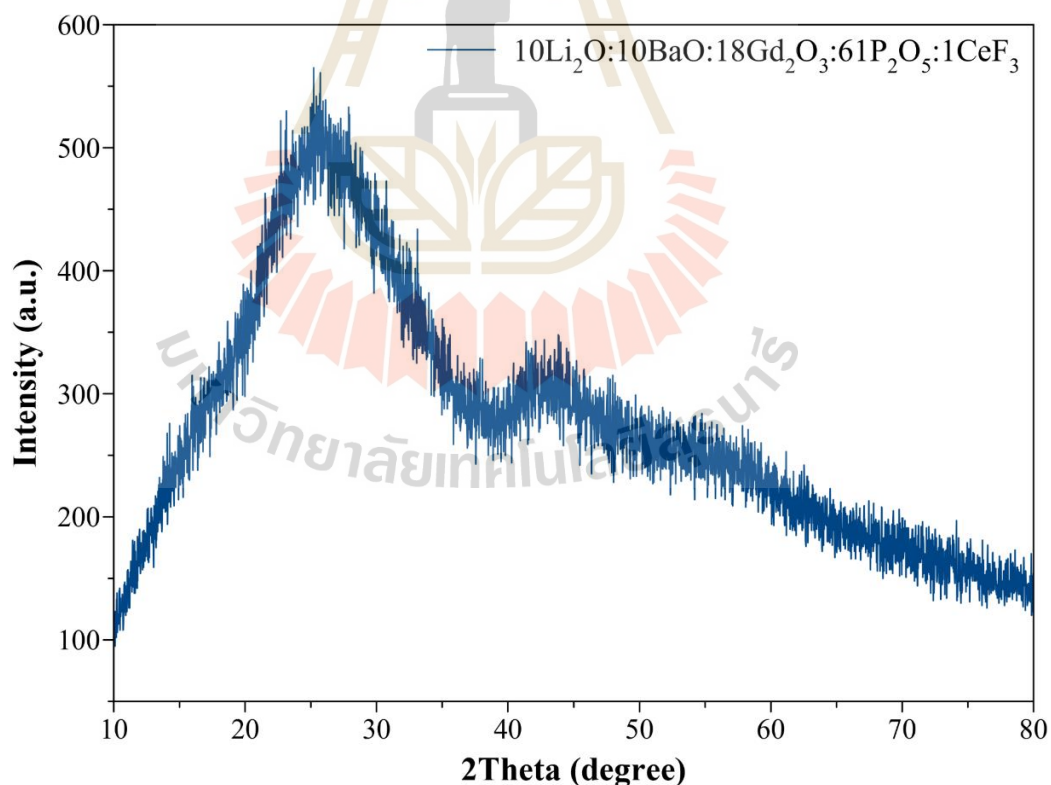
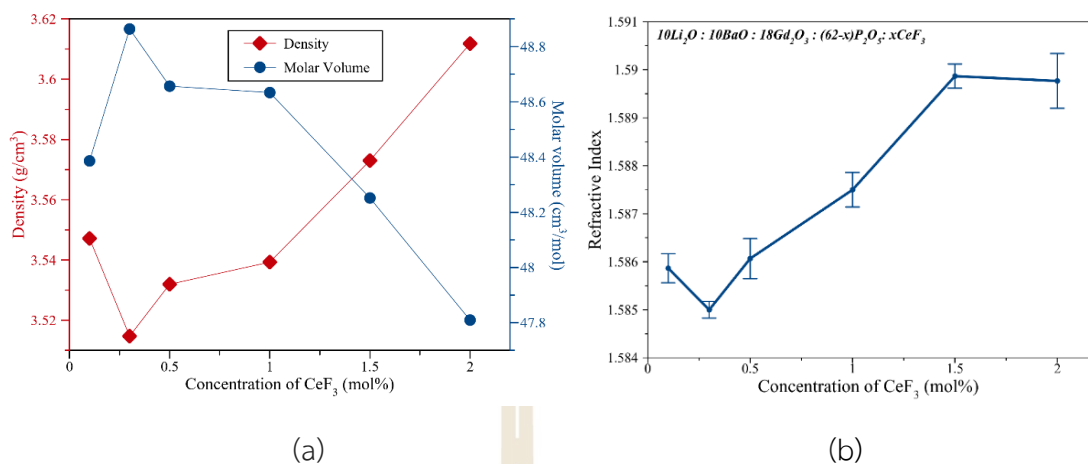


Figure 4.13 XRD pattern of Li-Ba-18Gd-xCe at  $x=1$  mol% phosphate glass sample.





**Figure 4.14** (a) The density and molar volume of Li-Ba-18Gd-xCe phosphate glasses and (b) The refractive index of Li-Ba-18Gd-xCe phosphate glasses.

In the Li-Ba-18Gd-xCe phosphate glass system, the addition of  $\text{CeF}_3$  resulted in changes in physical properties as shown in figure 4.14(a) and (b). The increase in  $\text{CeF}_3$  concentration led to an increase in both density and refractive index. However, a rapid decrease in molar volume was observed when the  $\text{CeF}_3$  concentration exceeded 1.0 mol%, which could be attributed to the breakdown of atomic bonding. These changes in physical properties are important for radiation detector applications, as the high values of physical density indicate a high stopping power of the host lattice. This means that the glass can efficiently absorb the incident radiation, thereby increasing the probability of radiation detection.

The elemental analysis of Li-Ba-18Gd-xCe at x=1 mol% phosphate glasses was performed using energy dispersive X-ray spectroscopy (EDX), which showed weight and atomic percentage values of different elements present in the glass (Table 4.5). The EDX analysis revealed the presence of O, P, Ba at K-edge, and Ce, Gd at L-edge. However, Li was not detected using this technique, as its atomic number 3 is very low, making it difficult to detect with EDX. It is important to note that this equipment is not capable of detecting a substance with an atomic number lower than 11.

These findings can be explained by the physics theory that the density and refractive index of a material are related to the atomic and molecular packing of the

material. The addition of  $\text{CeF}_3$ , which has a higher atomic number than the other constituents of the glass, leads to an increase in the overall atomic and molecular packing of the glass. This, in turn, leads to an increase in the density and refractive index of the glass. On the other hand, the breakdown of atomic bonding observed at higher  $\text{CeF}_3$  concentrations could be due to the increased concentration of Ce ions, which may lead to the formation of Ce clusters, resulting in the breakdown of the atomic bonding in the glass.

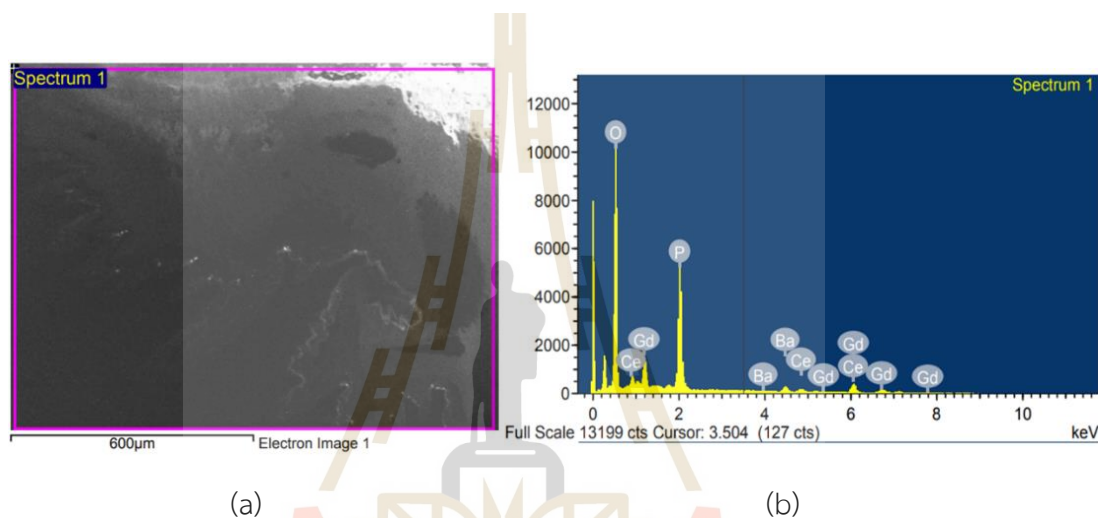


**Figure 4.15** (a) SEM image surface and (b) EDX elemental analysis surface of  $10\text{Li}_2\text{O}:10\text{BaO}:18\text{Gd}_2\text{O}_3:61\text{P}_2\text{O}_5:1\text{CeF}_3$  glass.

**Table 4.5** The elemental analysis of  $10\text{Li}_2\text{O}:10\text{BaO}:18\text{Gd}_2\text{O}_3:61\text{P}_2\text{O}_5:1\text{CeF}_3$  glass.

Element	%Weight	%Atomic
O K-edge	57.53	81.34
P K-edge	20.66	15.30
Ba K-edge	5.70	0.96
Ce L-edge	0.50	0.08
Gd L-edge	15.62	2.32

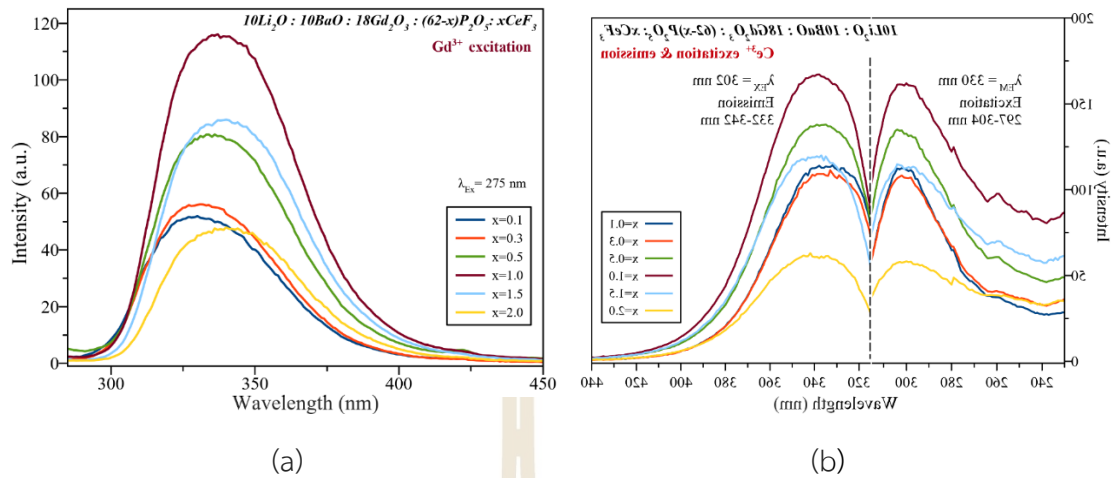


**Figure 4.16** (a) The spectra of  $Gd^{3+}$  excitation and (b) spectra of  $Ce^{3+}$  excitation and emission of Li-Ba-18Gd-xCe phosphate glasses.

In the field of luminescence spectroscopy, the emission spectra of materials provide a wealth of information about the electronic structure of luminescent centers. In this paragraph, the emission spectra of Li-Ba-18Gd-xCe ( $x = 0.1, 0.3, 0.5, 1.0, 1.5, 2.0$ ) phosphate glasses of  $Gd^{3+}$  and  $Ce^{3+}$  are analyzed. The luminescence intensity of a material is proportional to the number of excited centers emitting radiation. The figure 4.16 (a) and (b) show that the highest and lowest intensities luminescence for both excitation and emission present at 1.0 mol% and 2.0 mol% of  $CeF_3$ , respectively. The choice of the optimal concentration of a dopant in a host material is crucial in determining the best performance for a given application. The figure 4.17 shows the percentage of the area under the peak for emission of excitation spectra at different concentrations of  $Gd_2O_3$  and  $CeF_3$ . It is observed that the largest area under the peak of emission and excitation spectra is 1 mol% of  $CeF_3$  for various concentrations of  $CeF_3$ . The optimal concentration of  $CeF_3$  was chosen based on the maximum intensity of luminescence for the given material. This is an important factor to consider in the development of efficient scintillators and radiation detectors.

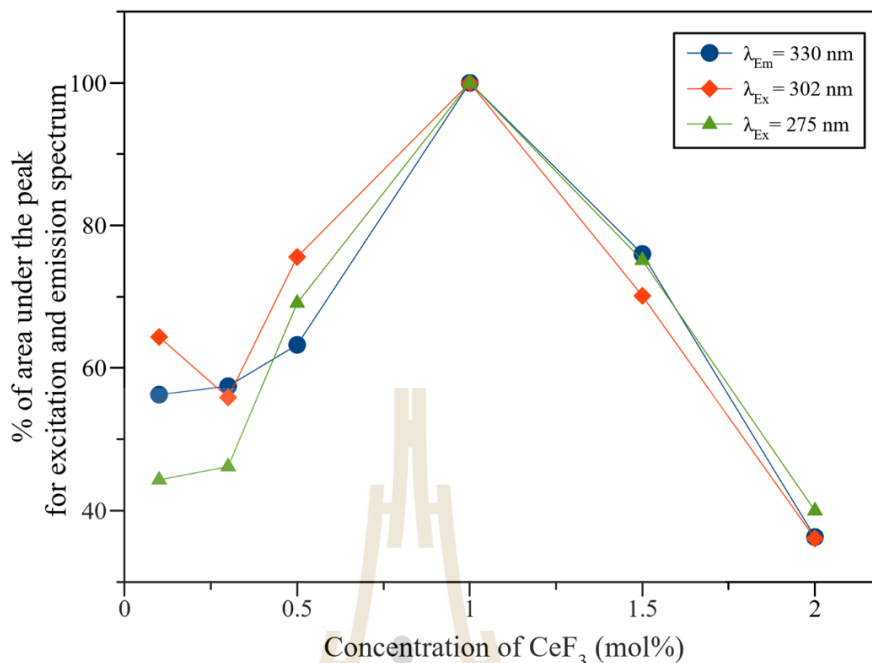


**Figure 4.17** The percent of area under the peak for emission of excitation spectrum at different concentration of CeF<sub>3</sub>.

The transmission spectra of Li-Ba-18Gd-xCe ( $x = 0.1, 0.3, 0.5, 1.0, 1.5, 2.0$ ) phosphate glasses in figure 4.17(a) show the wavelengths of light that are transmitted through the glass. The transmittance edge was observed in the range of 310-330 nm, which corresponds to the absorption edge of the glass. The high concentration of CeF<sub>3</sub> leads to an increase in the transmission edge, which causes a red-shift in the excitation. This red-shift is due to the creation of a new energy level in the glass caused by the presence of Ce<sup>3+</sup> ions. However, at 2.0 mol% of CeF<sub>3</sub>, the transmission edge shifts back towards blue. This may be due to an excess amount of CeF<sub>3</sub>, which causes the oxidation of some Ce<sup>3+</sup> ions to Ce<sup>4+</sup> ions. This process can lead to the formation of new energy levels in the glass, which can affect the transmission edge. The transmission spectra are important for the characterization of the glass as they provide information on the energy levels of the glass, which is crucial for understanding its optical properties. The shift in the transmission edge due to the presence of CeF<sub>3</sub> can be explained by the absorption and emission processes of the Ce<sup>3+</sup> ions in the glass, which is governed by the energy levels and transitions of the ions.

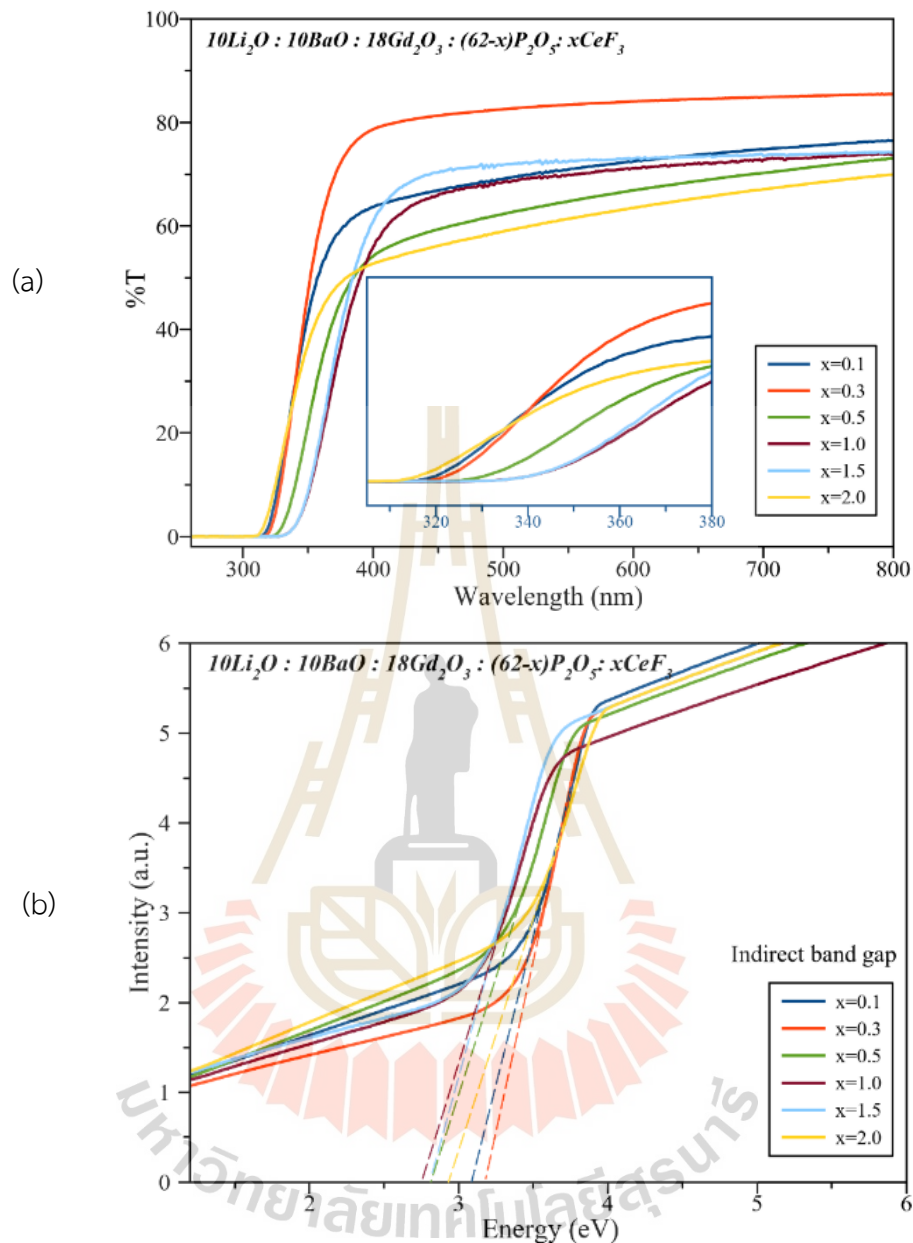


**Figure 4.18** (a) The transmission curves and (b) The optical band gap of Li-Ba-18Gd-xCe phosphate glasses.

The absorption spectra have been used to estimate the optical energy band gap for direct and indirect transitions from Tauc's relation plotting. Then the figure 53(b) showed the indirect and direct bandgap energy of Li-Ba-18Gd-xCe ( $x = 0.1, 0.3, 0.5, 1.0, 1.5, 2.0$ ) phosphate glasses were in rang of 2.7-3.10 eV and 3.3-3.6 eV, respectively. The optical band gap of all the studied Li-ba-18Gd-xCe phosphate glass samples are summarized in table 4.6. The energy of the optical band gap is connected

to the percentage of transmittance that is displayed in figure 4.18(a). In addition, a comparison of the optical band gaps is presented in table 4.6, which may be found here. Because the cut-off wavelength of phosphate glasses in this work are shorter than the absorption edge spectra of borate glasses from the literature, the optical band gap of the glasses that were analyzed is higher.

From the other type of glass optical band gap and cut-off transmittance wavelength, the increase in NBO caused a large number of negative charges to surround  $\text{Ce}^{3+}$ , which brought the 4f shell of  $\text{Ce}^{3+}$  closer to the 5d shell, which shifted the 4f-5d transition energy to the lower energy side and increased the cut-off wavelength in the absorption spectrum. The structures of phosphate glass, however, are distinct. Phosphate tetrahedra containing three bridging oxygens (BOs) and an O/P ratio of 2.5 are known as ultraphosphates. As  $\text{Q}^2$  species, metaphosphates with an O/P ratio of three are referred to as  $\text{PO}_4^{3-}$  tetrahedrons with two BOs. Typically,  $\text{Q}^2$  species consist of infinitely long chains and/or rings.

**Table 4.6** Data of indirect band gap of samples with various  $\text{CeF}_3$  of Li-Ba-18Gd-xCe phosphate glasses.

CeF <sub>3</sub> (mol%)	Optical Band gap (eV)		(Zaman et al., 2017) *
	Indirect	Direct	
x = 0.1	3.00 ± 0.05	3.60 ± 0.05	-
x = 0.3	2.70 ± 0.05	3.61 ± 0.05	2.2329
x = 0.5	2.70 ± 0.05	3.46 ± 0.05	2.2286
x = 1.0	2.87 ± 0.05	3.30 ± 0.05	2.2022
x = 1.5	2.94 ± 0.05	3.31 ± 0.05	2.1931
x = 2.0	3.10 ± 0.05	3.60 ± 0.05	2.1573

\*Li<sub>2</sub>O-Gd<sub>2</sub>O<sub>3</sub>-BaO-B<sub>2</sub>O<sub>3</sub> glass doped at 0.0, 0.3, 0.5, 0.1, 1.5 and 2.0 mol% of CeF<sub>3</sub>.



Applications that need rapid timing and a high pulse repetition present a high importance on the decay time. Figure 54 demonstrates the data of decay time of Li-Ba-18Gd-xCe ( $x = 0.1, 0.3, 0.5, 1.0, 1.5, 2.0$ ) phosphate glasses. The value of decay time in these samples lowers as the concentration of  $CeF_3$  increases. These results demonstrate that the influence of Ce-doped can decrease on the decay time, and the fastest decay time and highest emission luminescence were observed at a concentration of 1.0 mol %  $CeF_3$ .

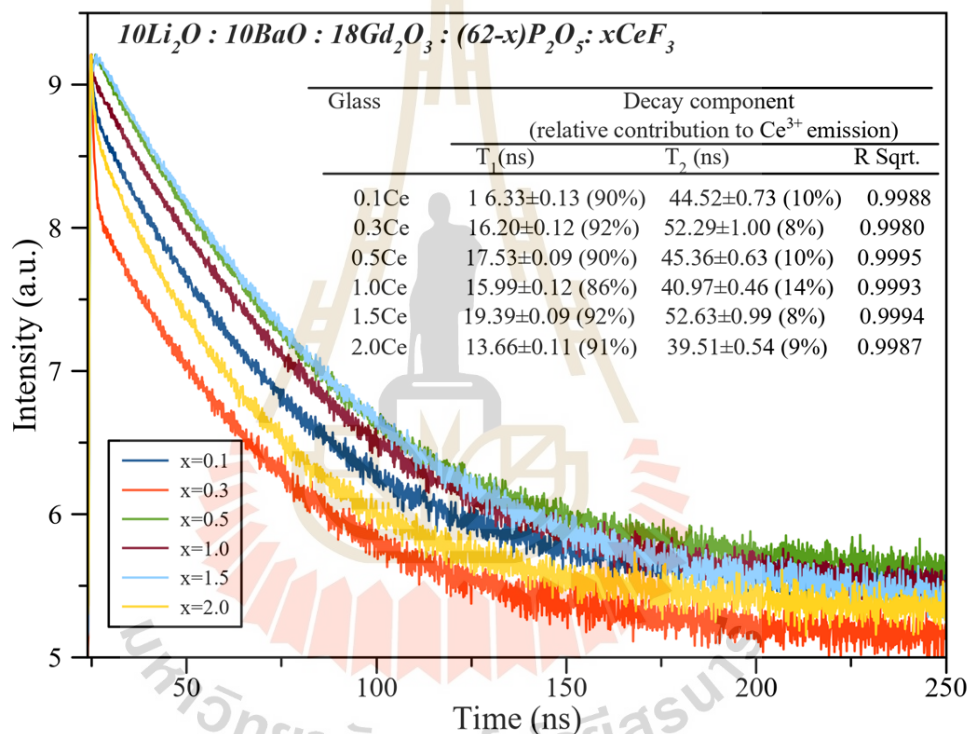


**Figure 4.19** The scintillation pulse shapes and decay time component of Li-Ba-18Gd-xCe ( $x = 0.1, 0.3, 0.5, 1.0, 1.5, 2.0$ ) phosphate glass.

#### 4.4 Radiation attenuation

The stopping power of a material for a charged particle is determined by its density, electronic and nuclear structure, and the velocity of the particle. The energy loss of a charged particle in matter can be described by the Bethe-Bloch formula, which takes into account the Coulomb interaction between the charged particle and the electrons in the material. The SRIM (Stopping and Range of Ions in Matter) program uses the Bethe-Bloch equation to calculate the energy loss and range of ions in various materials. In this work, the energy loss of alpha particles in Li-Ba-18Gd-xCe phosphate glasses was calculated using the SRIM program, and the results were presented in table 4.7 and figure 4.20. As the alpha particle energy increases, the range of the ions in the material also increases due to the increased Coulomb interaction between the alpha particle and the electrons in the material. The information provided in the table and figure can be useful for designing radiation detectors and understanding the interaction of alpha particles with matter.

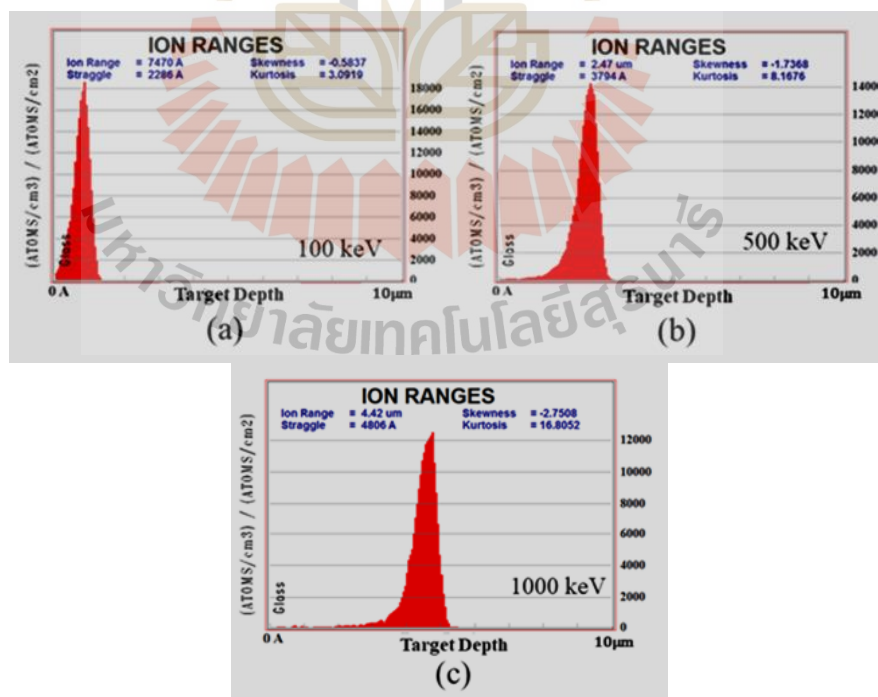


**Figure 4.20** Ion distribution of  $10\text{Li}_2\text{O}:10\text{BaO}: 18\text{Gd}_2\text{O}_3:61\text{P}_2\text{O}_5:1\text{CeF}_3$  glass in different energy of  $^4\text{He}$  ions of (a) 100 keV, (b) 500 keV and (c) 1000 keV.

**Table 4.7** The percentage of energy loss in different energy of He ions interacted with  $10\text{Li}_2\text{O}:10\text{BaO}:18\text{Gd}_2\text{O}_3:61\text{P}_2\text{O}_5:1\text{CeF}_3$  glass.

%Energy loss	He at 100 keV		He at 500 keV		He at 1000 keV	
	Ions	Recoils	Ions	Recoils	Ions	Recoils
Ionization	94.07	0.75	98.38	0.22	99.07	0.13
Vacancies	0.08	0.12	0.02	0.03	0.01	0.02
Phonons	0.66	4.32	0.17	1.18	0.09	0.68

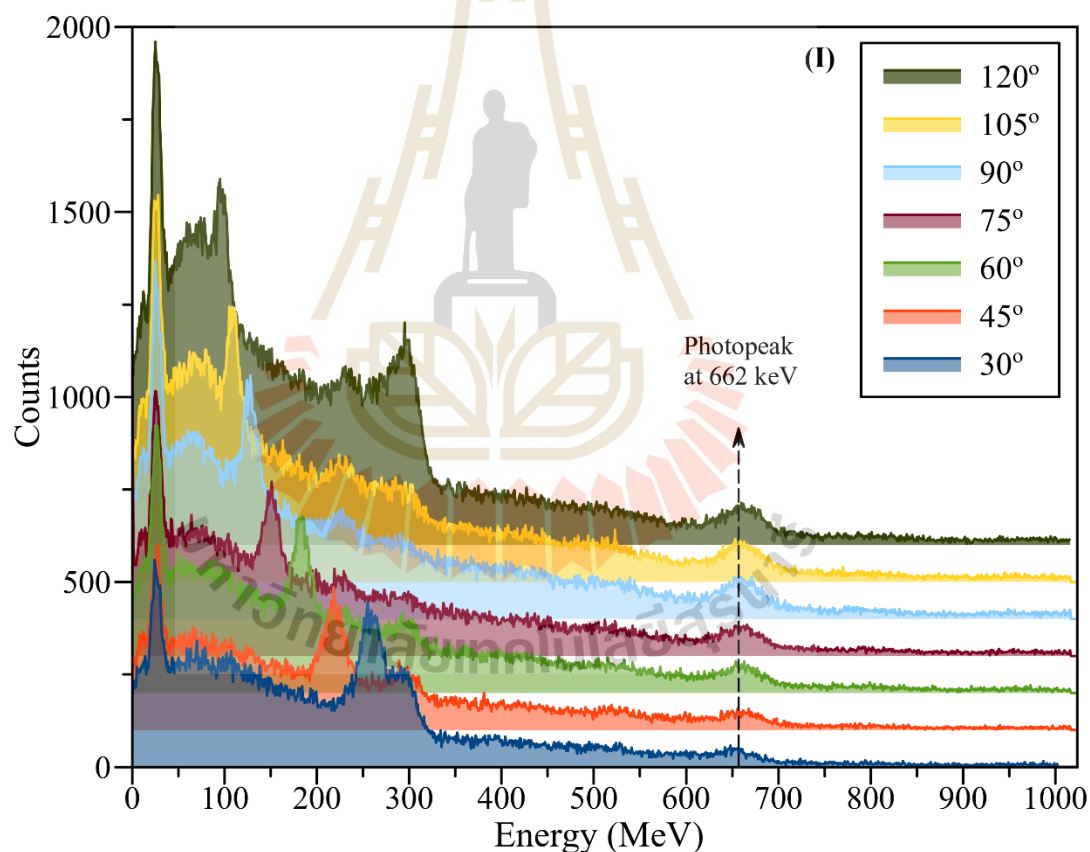


**Figure 4.21** The typical  $\text{Cs}^{137}$  at 0.662 MeV (662 keV) for transmitted (I) gamma-rays intensities of  $10\text{Li}_2\text{O}:10\text{BaO}:18\text{Gd}_2\text{O}_3:61.5\text{P}_2\text{O}_5:0.5\text{CeF}_3$  (Li-18Gd-0.5Ce) glass are scattered at different angles.

In the study, the mass attenuation coefficient of the Li-18Gd-0.5Ce glass sample was measured using gamma rays. The mass attenuation coefficient describes how a

material interacts with electromagnetic radiation, such as gamma rays, and is dependent on factors such as the density and atomic number of the material. The gamma ray source used in the study had an energy of 309 keV. The glass sample was thin, with a thickness of 0.33 cm, and its density was calculated using the Archimedes method, which involves measuring the displacement of a fluid when an object is submerged in it. The density of the Li-18Gd-0.5Ce glass sample was found to be 3.4458 g/cm<sup>3</sup>. The measurement of mass attenuation coefficient is an important parameter in the selection and design of materials for radiation shielding applications, as it can determine the amount of radiation that can be absorbed by the material.

The total mass attenuation coefficient and partial interaction for the Li-18Gd-0.5Ce glass formula were calculated using the WinXcom model, and the results are presented in table 4.9. The total mass attenuation coefficient, which characterizes the interaction of a material with radiation, is improved when there is an increase in photoelectric absorption, both incoherent and coherent, and an increase in the scattering angle of photons. This is because when the scattering angle of a photon is increased, the photoelectric effect occurs at a lower energy, which is proportional to the photopeak of an experiment at around 662 keV (Parks, 2015). This phenomenon can be explained by Compton scattering, which is the scattering of a photon by a charged particle, typically an electron, resulting in a decrease in energy of the photon and an increase in the scattering angle. The partial interaction values also indicate the contribution of each element to the total mass attenuation coefficient, with Gd<sub>2</sub>O<sub>3</sub> having the highest contribution due to its high atomic number and density. Overall, these results suggest that the Li-18Gd-0.5Ce glass formula has potential as a radiation shielding material due to its high mass attenuation coefficient.

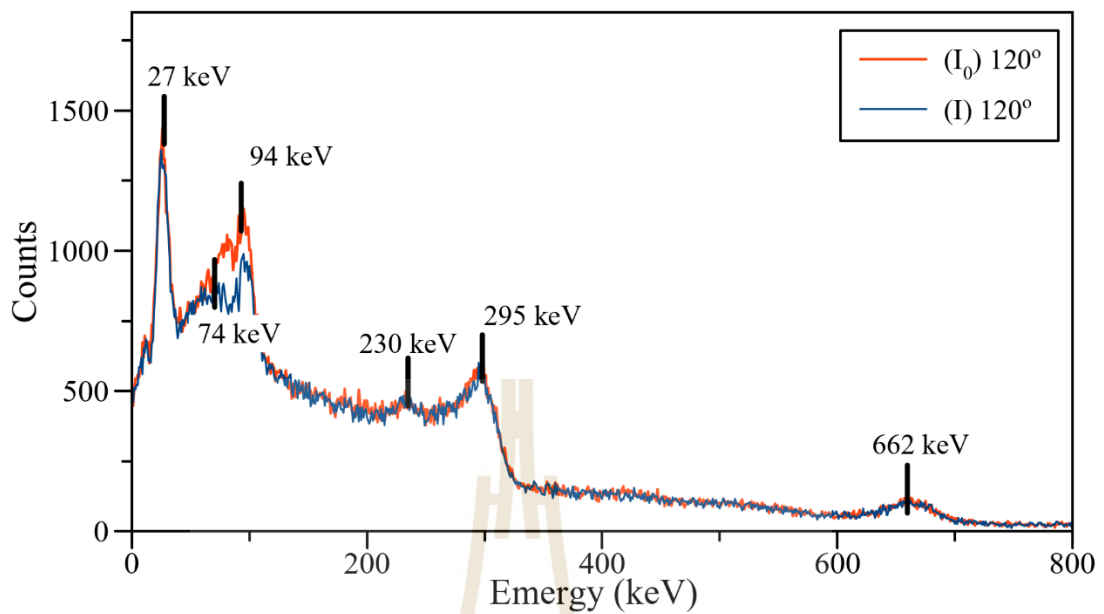


**Figure 4.22** A typical energy spectrum for Cs-137 gamma rays scattered at an angle of  $120^\circ$  relative to the direction of the gamma rays being emitted from the source. , The incident ( $I_0$ ) (in red line) and transmitted ( $I$ ) (in blue line) gamma-rays intensities of  $10\text{Li}_2\text{O}:10\text{BaO}:18\text{Gd}_2\text{O}_3:61.5\text{P}_2\text{O}_5:0.5\text{CeF}_3$  (Li-18Gd-0.5Ce) glass.

The weight fractions of glass composition and density were show in table 13. The experimental values and theoretical values (obtained from WinX Com program) of the mass attenuation coefficients, partial interactions of Li-18Gd-0.5Ce phosphate glass calculated in the energy range 223 – 561 keV from WinXCom program as show in Table 4.8. The variation of partial interactions (coherent, incoherent and photoelectric).

Half value layer (HVL) is the thickness of an absorber required to attenuate the intensity of beam to half of its original value. if attenuation can be described by eq. (34)

$$\text{Half value layer (HVL)} = \frac{\ln 2}{\mu} = \frac{0.693}{\mu} \quad (34)$$

**Table 4.8** The weight fractions and density of Li-18Gd-0.5Ce photphase glass.

Sample	Composition (Weight%)							Density (g/cm <sup>3</sup> )
	Li	Ba	Gd	P	Ce	O	F	
Li-18Gd- 0.5Ce	0.8078	7.9910	32.9412	22.1689	0.4077	0.1658	35.5176	3.4458

**Table 4.9** The total mass attenuation coefficients and Partial interaction of Li-18Gd-0.5Ce photphase glass.

Energy (keV)	$\mu_m$ ( $\times 10^{-2}$ cm <sup>2</sup> /g)			Partial interaction ( $\times 10^{-2}$ cm <sup>2</sup> /g)		
	Th	Exp	%RD	Coherent	Incoherent	Photoelectric
561.68 $\pm$ 27.8	8.84	-	-	0.25	7.53	1.06
481.59 $\pm$ 20.7	10.12	9.66 $\pm$ 0.47	4.57	0.35	8.09	1.63
398.97 $\pm$ 16.0	11.58	10.78 $\pm$ 0.46	6.74	0.48	8.63	2.47
340.83 $\pm$ 16.1	13.75	13.86 $\pm$ 0.55	0.80	0.76	9.20	3.88
287.28 $\pm$ 15.6	16.55	15.02 $\pm$ 0.71	9.28	0.91	9.72	5.93
252.98 $\pm$ 14.2	19.94	19.46 $\pm$ 1.06	2.41	1.17	10.17	7.55
223.02 $\pm$ 12.2	23.69	21.72 $\pm$ 1.22	8.34	1.44	10.54	11.71

The total mass attenuation coefficient is a crucial parameter for understanding how a material interacts with radiation. It describes the ability of a material to attenuate the intensity of a beam of photons or particles as it passes through it. This coefficient considers all possible mechanisms of interaction, including photoelectric absorption, Compton scattering, and pair production. The unit of the total mass attenuation coefficient is dependent on the energy of the incident radiation and the atomic composition of the material.



Partial interaction coefficients, on the other hand, refer to the contribution of each individual mechanism of interaction to the total attenuation coefficient. These coefficients provide valuable insight into the dominant mechanism of interaction for a given material and energy of the incident radiation. By understanding the relative contributions of each mechanism, it is possible to optimize the design of radiation detection systems and to develop materials that are better suited for specific applications. For example, a material with a high photoelectric absorption coefficient might be more suitable for detecting low-energy gamma rays, while a material with a high Compton scattering coefficient might be more effective at detecting higher energy gamma rays.

**Table 4.10** The effective atomic numbers and density of electron of Li-18Gd-0.5Ce photphase glass.

Energy (keV)	$Z_{\text{eff}}(\text{th})$ (e <sup>-</sup> /atom)	$Z_{\text{eff}}(\text{ex})$ (e <sup>-</sup> /atom)	$N_e(\text{th})$ ( $\times 10^{23}$ )	$N_e(\text{ex})$ ( $\times 10^{23}$ )	$\text{HVL} = \frac{\ln 2}{\mu_{\text{th}}}(\text{cm})$
561.68 ± 27.8	27.34	-	3.118	-	7.84
481.59 ± 20.7	33.56	44.52 ± 2.20	3.268	3.12 ± 0.15	6.85
398.97 ± 16.0	36.36	45.87 ± 1.97	3.451	3.21 ± 0.14	5.99
340.83 ± 16.1	41.15	53.80 ± 2.16	3.740	3.77 ± 0.15	5.04
287.28 ± 15.6	47.21	53.20 ± 2.51	4.108	3.73 ± 0.19	4.19
252.98 ± 14.2	54.33	63.18 ± 3.43	4.535	4.43 ± 0.24	3.48
223.02 ± 12.2	61.61	65.07 ± 3.65	4.974	4.56 ± 0.27	2.92

Calculate the theoretical values for the scattered electron and photon. The energy from the photon attenuation experiment using the Compton formula. Comparing these results to the experimental values, we discovered that the value of the total mass attenuation, the effective atomic numbers, and the electron density of Li-18Gd-0.5Ce photphase glass are close to and related to the theoretical values, as shown in tables 4.9 and 4.10. And the effective atomic numbers ( $Z_{\text{eff}}$ ) are increase with decreasing.

## CHAPTER V

### CONCLUSION

The study focused on exploring the Li-Ba-xGd-0.5Ce phosphate glasses system to investigate whether the concentration of  $Gd_2O_3$  in the glass could impact its properties, such as density, reflective index, photoluminescence, and radioluminescence. The density of the glass was found to increase linearly with an increase in the concentration of  $Gd_2O_3$  up to 16 mol%, and then the increment decreased slightly at 18 mol%. The increase in density was attributed to the higher atomic mass of Gd ions than P ions in the glass network matrix. The molar volume decreased, and the refractive index increased with an increase in the concentration of  $Gd_2O_3$ . Further investigation revealed that the sample with 18 mol% of  $Gd_2O_3$  concentration and 1.0 mol% of  $CeF_3$  concentration was the most appropriate choice. The increase in  $CeF_3$  concentration led to an increase in both the density and reflective index of the sample. However, the rate of decay also increased. At a concentration of 1.0 mol% of  $CeF_3$ , the emission luminescence was found to be at its highest, indicating the potential for excellent luminescence properties.

**Table 5.1** Comparative properties of Li-18Gd-1Ce phosphate glass in this work and commercial.

Properties	Li-18Gd-1Ce phosphate	BGO commercial
wavelength (Max. Emission) (nm)	330	480
Wavelength range (nm)	240-400	375 -650
Decay time (ns)	16	300
Refractive index	1.59	2.15

The mechanism that allowed energy transfer from Gd ions to Ce ions within the glass matrix was responsible for the observed excellent luminescence properties. Moreover, the glass samples were investigated for their ionizing radiation detection properties. The results from the SRIM program showed that the glass sample could detect gamma rays and decrease their photon energy, making it an ideal candidate for further development into a radiation detector. The Li-Ba-18Gd-xCe phosphate glass system with the composition  $10\text{Li}_2\text{O} : 10\text{BaO} : 18\text{Gd}_2\text{O}_3 : 61\text{P}_2\text{O}_5 : 1\text{CeF}_3$  was identified as the ideal phosphate glass composition based on the investigation results.

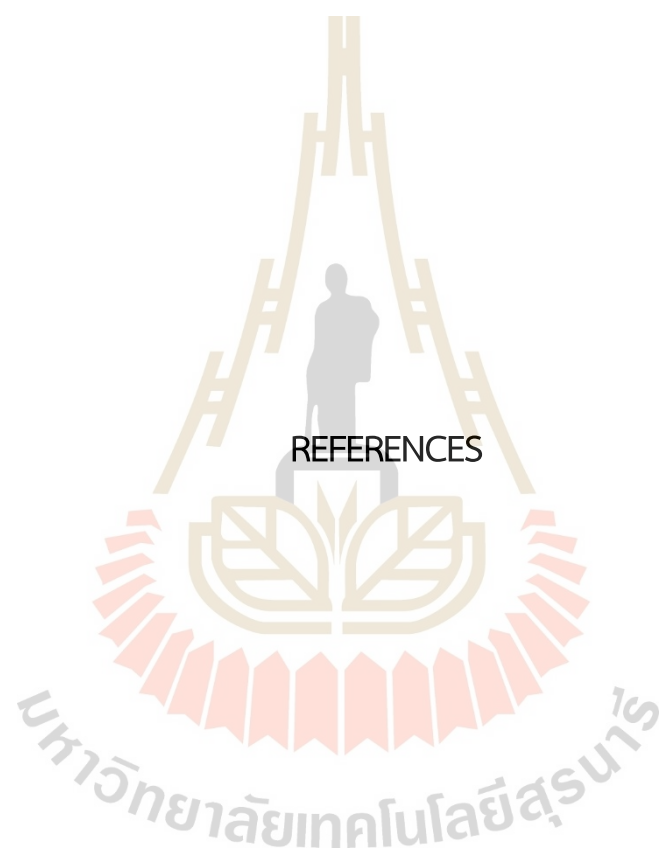
Ionizing radiation detectors are used in various fields, such as nuclear power plants, medical imaging, and environmental monitoring. To detect ionizing radiation, scintillation materials are commonly used. Scintillation materials are materials that emit light when they absorb ionizing radiation. These materials are often used in radiation detectors because they can convert ionizing radiation into visible light signals that can be detected by photodetectors.

In this study, the researchers aimed to develop a radiation detector using Li-Ba-xGd-0.5Ce phosphate glass samples. The first step was to estimate the amount of energy lost by the alpha particle when it passes through materials using the SRIM program. SRIM, or stopping and range of ions in matter, is a program used to simulate the energy loss of ions in matter. This simulation is crucial in designing radiation detectors because it provides information on how materials interact with ionizing radiation. Results showed that the range of stopping ions increased as alpha energy increased. This means that the more energy an alpha particle has, the deeper it can penetrate a material. This information was used to determine the thickness of the glass samples required to effectively detect alpha particles.

To confirm the glass samples' ability to detect gamma rays and decrease their photon energy, the researchers used the CCT approach. The CCT approach is a common method used to characterize scintillation materials' ionizing radiation detection properties. The results indicated that the glass samples could effectively detect gamma rays and decrease their photon energy.

The generated and characterized samples were found to have comparable qualities with commercial BGO, which is a well-known scintillation material used in radiation detectors. This makes the Li-Ba-xGd-0.5Ce phosphate glass samples an ideal candidate for further development into a radiation detector with a large surface area, many functions, and diverse shapes.





## REFERENCES

- Abou Neel, E. and Knowles, J. (2009). Biocompatibility and other properties of phosphate-based glasses for medical applications. In Cellular Response to Biomaterials, pages 156–182. Elsevier.
- Al-Hadeethi, Y., Sayyed, M., Kaewkhao, J., Raffah, B. M., Almalki, R., and Rajaramakrishna, R. (2019). An extensive investigation of physical, optical and radiation shielding properties for borate glasses modified with gadolinium oxide. *Applied Physics A*, 125(11), 1–10.
- Ambati, J., Lopez, A., Cochran, D., Wattamwar, P., Bean, K., Dziubla, T., and Rankin, S. (2012). Engineered silica nanocarriers as a high-payload delivery vehicle for antioxidant enzymes. *Acta biomaterialia*, 8(6), 2096–2103.
- Brow, R. K. (2000). The structure of simple phosphate glasses. *Journal of Non-Crystalline Solids*, 263, 1–28.
- Brow, R. K. and WITTENAUER, A. K. (2002). Rare earth coordination environments in ultraphosphate glasses. *Phosphorus Research Bulletin*, 13, 95–100.
- Calahoo, C. and Wondraczek, L. (2020). Ionic glasses: Structure, properties and classification. *Journal of Non-Crystalline Solids: X*, 8, 100054.
- Chanthima, N., Prongsamrong, P., Kaewkhao, J., and Limsuwan, P. (2012). *Simulated radiation attenuation properties of cement containing with baso4 and pbo. Procedia Engineering*, 32, 976–981.
- Chanthima, N., Tongdang, J., Reungsri, S., and Kaewkhao, J. Determination of radiation attenuation coefficient on lithium barium bismuth phosphate glasses at 662 kev.



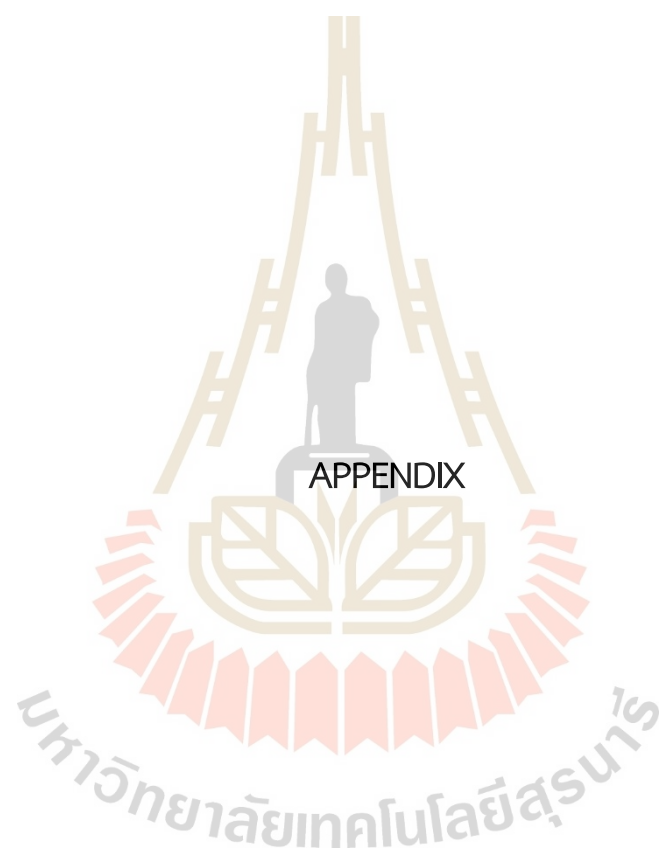
- Damodaraiah, S. and Ratnakaram, Y.(2019). Energy transfer studies and neutral to warm white light generation in  $\text{dy}^{3+}\text{-sm}^{3+}$  co-doped bismuth phosphate glasses for lighting applications. *Journal of Luminescence*, 207, 553–560.
- Gerward, L., Guilbert, N., Jensen, K. B., and Levring, H. (2004). Winxcom—a program for calculating x-ray attenuation coefficients. *Radiation physics and chemistry*, 71(3-4), 653–654.
- Guo, M., Yue, Y., Yu, J., Shao, C., Ren, J., Wang, X., and Hu, L. (2020). Effect of  $\text{li}_2\text{o}$  substitution on structures and properties of  $\text{nd}^{3+}$ -doped  $\text{al}(\text{po}_3)_3\text{-li}_2\text{o}$  glasses. *International Journal of Applied Glass Science*, 11(1), 66–77.
- Ilichev, V., Silantjeva, L., Kukinov, A., and Bochkarev, M. (2019). Photophysical properties of ir luminescent lanthanide complexes with polyfluorinated ligands. *OPEN*, 2(3), 78–83.
- Issard, H. (2015). Radiation protection by shielding in packages for radioactive materials. In *Safe and Secure Transport and Storage of Radioactive Materials*, pages 123–140. Elsevier.
- Kaewkhao, J., Laopaiboon, J., and Chewpraditkul, W. (2008). Determination of effective atomic numbers and effective electron densities for  $\text{cu}/\text{zn}$  alloy. *Journal of Quantitative Spectroscopy and Radiative Transfer*, 109(7), 1260–1265.
- Korthout, K., Parmentier, A. B., Smet, P. F., and Poelman, D. (2013). A xas study of the luminescent  $\text{eu}$  centers in thiosilicate phosphors. *Physical Chemistry Chemical Physics*, 15(22), 8678–8683.
- Kubala-Kuku's, A., Ludwikowska-Kdzia, M., Bana's, D., Braziewicz, J., Majewska, U., Pajek, M., and Wudarczyk-Mo'cko, J. (2013). Application of the x-ray fluorescence analysis and x-ray diffraction in geochemical studies of the pleistocene tills from holy cross mountains. *Radiation Physics and Chemistry*, 93, 92–98.

- Kučera, M., Nikl, M., Hanuš, M., and Onderišinová, Z. (2013). Gd<sup>3+</sup> to Ce<sup>3+</sup> energy transfer in multi-component gadolinium and gadolium garnet scintillators. *physica status solidi (RRL)–Rapid Research Letters*, 7(8), 571–574.
- Kurkjian, C. R. and Prindle, W. R. (1998). Perspectives on the history of glass composition. *Journal of the American Ceramic Society*, 81(4):795–813.
- Lang, R. (1935). The spectrum of trebly ionized cerium. *Canadian Journal of Research*, 13(1), 1–4.
- Limkitjaroenporn, P., Kaewkhao, J., and Asavavisithchai, S. (2013). Determination of mass attenuation coefficients and effective atomic numbers for inconel 738 alloy for different energies obtained from compton scattering. *Annals of Nuclear Energy*, 53, 64–68.
- Lozano, G., Marega Jr, E., Rivera, V., et al. (2021). Xps analysis of bridging and non-bridging oxygen in Yb<sup>3+</sup>-Er<sup>3+</sup>-Tm<sup>3+</sup>-doped zinc-tellurite glasses. *Journal of Non-Crystalline Solids*, 553, 120520.
- Luo, H., Hu, X., Liu, W., Zhang, Y., Lu, A., and Hao, X. (2014). Compositional dependence of properties of Gd<sub>2</sub>O<sub>3</sub>-SiO<sub>2</sub>-B<sub>2</sub>O<sub>3</sub> glasses with high Gd<sub>2</sub>O<sub>3</sub> concentration. *Journal of Non-Crystalline Solids*, 389, 86–92.
- Machewirth, D. P. (1996). Characterization of novel rare-earth-doped laser glasses. Rutgers The State University of New Jersey, School of Graduate Studies.
- Marra, P. (2016). Theoretical approach to direct resonant in-elastic x-ray scattering on magnets and superconductors. arXiv preprint arXiv, 1605.03189.
- Moses, W., Derenzo, S., Weber, M., Ray-Chaudhuri, A., and Cerrina, F. (1994). Scintillation mechanisms in cerium fluoride. *Journal of luminescence*, 59(1-2), 89–100.
- Oomen, E. and Van Dongen, A.-M. A. (1989). Europium (iii) in oxide glasses: dependence of the emission spectrum upon glass composition. *Journal of Non-Crystalline Solids*, 111(2-3), 205–213.

- Parks, J. E. (2015). The Compton effect-compton scattering and gamma ray spectroscopy. Department of Physics and Astronomy, *The University of Tennessee Knoxville, Tennessee*, pages 37996–1200.
- Peijzel, P., Vermeulen, P., Schrama, W., Meijerink, A., Reid, M., and Burdick, G. (2005). High-resolution measurements of the vacuum ultraviolet energy levels of trivalent gadolinium by excited state excitation. *Physical Review B*, 71(12), 125126.
- Reid, M. F. (2016). Theory of rare-earth electronic structure and spectroscopy. In Handbook on the physics and chemistry of rare earths, volume 50, pages 47–64. Elsevier.
- Rocha, F. S., Gomes, A. J., Lunardi, C. N., Kaliaguine, S., and Patience, G. S. (2018). Experimental methods in chemical engineering: Ultraviolet visible spectroscopy—uv-vis. *The Canadian Journal of Chemical Engineering*, 96(12), 2512–2517.
- Stutzmann, M., Brandt, M. S., and Bayerl, M. W. (2000). Spin-dependent processes in amorphous and microcrystalline silicon: a survey. *Journal of Non - Crystalline solids*, 266, 1–22.
- Wantana, N., Kaewnuam, E., Chanthima, N., Kaewjaeng, S., Kim, H., and Kaewkhao, J. (2018). Ce<sup>3+</sup> doped glass for radiation detection material. *Ceramics International*, 44, S172–S176.
- Weber, M., Bliss, M., Craig, R., and Sunberg, D. (1995). Scintillators and applications: Cerium-doped materials. *Radiation effects and defects in solids*, 134(1-4), 23–29.
- Yao, Y., Liu, L., Zhang, Y., Chen, D., Fang, Y., and Zhao, G. (2016). Optical properties of ce<sup>3+</sup> doped fluorophosphates scintillation glasses. *Optical Materials*, 51, 94–97.

- Zagrai, M., Suciu, R.-C., Rada, S., Pic ă, M., and Pruneanu, S. (2021). Structural and optical properties of eu<sup>3+</sup> ions in lead glass for photonic applications. *Journal of Non-Crystalline Solids*, 569, 120988.
- Zhang, F.-H., Wang, Y.-Y., Lv, C., Li, Y.-C., and Zhao, X. Q. (2019). Luminescent complexes associated with isonicotinic acid. *Journal of Luminescence*, 207, 561–570.





APPENDIX





## CURRICULUM VITAE

**Name:** Phitsamai Kamonpha

**Gender:** Female

**Nationality:** Thai

**Date of Birth:** 14 March 1993

**Email:** phitsamai.own1993@gmail.com

### **Educations:**

- 2006-2011, High school at Buakhao school
- 2012-2015, Bachelor of Science, Physics department, Institute of Science, Ubon Rachathani University
- 2016-2018, Master of Science, School of Physics, Institute of Science, Suranaree University of Technology
- 2019-2022, Doctor of Philosophy of Science, School of Physics, Institute of Science, Suranaree University of Technology

### **Publications:**

1. Synthesis and characterization of  $\text{CH}_3\text{NH}_3\text{PbI}_3$  and  $\text{CH}_3\text{NH}_3\text{PbI}_{(3-x)}\text{Cl}_x$  perovskite solar cell materials
2. The current status of time-resolved XAS beamline at SLRI and application on in situ experiments
3. In-situ investigation of ethanol steam reforming on Ni and Cr doped ferrites using combined X-ray absorption spectroscopy, mass spectrometry, and gas chromatography
4. Structural and luminescence investigation of  $\text{Ce}^{3+}$  doped lithium barium gadolinium phosphate glass scintillator
5. An Operando X-ray Absorption Spectroscopy Study on Sensing Characteristics of Vertically Aligned ZnO Thin Film for Methane Gas Sensors